March-April 1961
Vol. 65D
No. 2
Radio Propagation

SCIENCE

Volume 65D
Number 2
Mar.–Apr. 1961

RECEIVED
MAR 23 1961
MIAMI UNIVERSITY
LIBRARY

Radio Propagation

MIAMI UNIVERSITY LIBRARY
MAR 20 1961

SECTION D

JOURNAL OF RESEARCH

NATIONAL BUREAU OF STANDARDS

Journal of Research

of the

National Bureau of Standards

D. RADIO PROPAGATION

MAR.–APR. • 1961

VOLUME • 65D

NUMBER • 2

Editor: James R. Wait
Central Radio Propagation Laboratory, National Bureau of Standards, Boulder, Colo.

Associate Editors: T. N. Gautier, J. W. Herbstreit, R. C. Kirby, C. G. Little, A. G. McNish, R. A. Helliwell, W. E. Gordon, A. D. Wheelon, S. Silver

IRE Advisors: A. H. Waynick, K. M. Siegel

Publication dates:
Jan. 15, Mar. 15, May 15, July 15, Sept. 15, Nov. 15, 1961

JOURNAL OF RESEARCH

The National Bureau of Standards Journal of Research reports research and development in the fields of activity shown at right. Also included from time to time are survey articles related to the Bureau's scientific and technical program.

The Journal is published in four separate sections as follows:

A. Physics and Chemistry

Contains papers of interest primarily to scientists working in these fields. Issued six times a year. Annual subscriptions: domestic, $4.00; foreign, $4.75.

B. Mathematics and Mathematical Physics

Presents studies and compilations designed mainly for the mathematician and the theoretical physicist. Issued quarterly. Annual subscription: domestic, $2.25; foreign, $2.75.

C. Engineering and Instrumentation

Reports research and development results of interest chiefly to the engineer and the applied scientist. Issued quarterly. Annual subscription: domestic, $2.25; foreign, $2.75.

D. Radio Propagation

Reports research in radio propagation, upper atmospheric physics, and communications. Issued six times a year. Annual subscription: domestic, $4.00; foreign, $4.75.

Functions and Activities

The functions of the National Bureau of Standards are set forth in the Act of Congress, March 3, 1901, as amended. These include the development and maintenance of the national standards of measurement and the provision of means and methods for making measurements consistent with these standards; the determination of physical constants and properties of materials; the development of methods and instruments for testing materials, devices, and structures; advisory services to government agencies on scientific and technical problems; invention and development of devices to serve special needs of the Government; and the development of standard practices, codes, and specifications. The work includes basic and applied research, development, engineering, instrumentation, testing, evaluation, calibration services, and various consultation and information services. The Bureau also serves as the Federal technical research center in a number of specialized fields. The scope of activities of the National Bureau of Standards is suggested in the following listing of the divisions and sections engaged in technical work.

Washington, D.C.

Electricity. Resistance and Reactance. Electrochemistry. Electrical Instruments. Magnetic Measurements. Dielectrics.

Metrology. Photometry and Colorimetry. Refractometry. Photographic Research. Length. Engineering Metrology. Mass and Scale. Volumetry and Densimetry.

Heat. Temperature Physics. Heat Measurement. Cryogenic Physics. Equation of State. Statistical Physics.

Radiation Physics. X-ray. Radioactivity. Radiation Theory. High Energy Radiation. Radiological Equipment. Nucleonic Instrumentation. Neutron Physics.

Analytical and Inorganic Chemistry. Pure Substances. Spectrochemistry. Solution Chemistry. Analytical Chemistry. Inorganic Chemistry.

Mechanics. Sound. Pressure and Vacuum. Fluid Mechanics. Engineering Mechanics. Rheology. Combustion Controls.

Organic and Fibrous Materials. Rubber. Textiles. Paper. Leather. Testing and Specifications. Polymer Structure. Plastics. Dental Research.

Metallurgy. Thermal Metallurgy. Chemical Metallurgy. Mechanical Metallurgy. Corrosion. Metal Physics.

Mineral Products. Engineering Ceramics. Glass. Refractories. Enameled Metals. Crystal Growth. Constitution and Microstructure.

Building Research. Structural Engineering. Fire Research. Mechanical Systems. Organic Building Materials. Codes and Safety Standards. Heat Transfer. Inorganic Building Materials.

Applied Mathematics. Numerical Analysis. Computation. Statistical Engineering. Mathematical Physics.

Data Processing Systems. Components and Techniques. Digital Circuitry. Digital Systems. Analog Systems. Applications Engineering.

Atomic Physics. Spectroscopy. Radiometry. Solid State Physics. Electron Physics. Atomic Physics.

Instrumentation. Engineering Electronics. Electron Devices. Electronic Instrumentation. Mechanical Instruments. Basic Instrumentation.

Physical Chemistry. Thermochemistry. Surface Chemistry. Organic Chemistry. Molecular Spectroscopy. Molecular Kinetics. Mass Spectrometry. Molecular Structure and Radiation Chemistry.

• **Office of Weights and Measures**

Boulder, Colorado

Cryogenic Engineering. Cryogenic Equipment. Cryogenic Processes. Properties of Materials. Gas Liquefaction.

Ionosphere Research and Propagation. Low Frequency and Very Low Frequency Research. Ionosphere Research. Prediction Services. Sun-Earth Relationships. Field Engineering. Radio Warning Services.

Radio Propagation Engineering. Data Reduction Instrumentation. Radio Noise. Tropospheric Measurements. Tropospheric Analysis. Propagation-Terrain Effects. Radio-Meteorology. Lower Atmospheric Physics.

Radio Standards. High-Frequency Electrical Standards. Radio Broadcast Service. Radio and Microwave Materials. Atomic Frequency and Time Standards. Electronic Calibration Center. Millimeter-Wave Research. Microwave Circuit Standards.

Radio Systems. High Frequency and Very High Frequency Research. Modulation Research. Antenna Research. Navigation Systems. Space Telecommunications.

Upper Atmosphere and Space Physics. Upper Atmosphere and Plasma Physics. Ionosphere and Exosphere Scatter. Airglow and Aurora. Ionospheric Radio Astronomy.

U.S. DEPARTMENT OF COMMERCE
Luther H. Hodges, Secretary

NATIONAL BUREAU OF STANDARDS
A. V. Astin, Director

Order all publications from the Superintendent of Documents, U.S. Government Printing Office, Washington 25, D.C.

Use of funds for printing this publication approved by the Director of the Bureau of the Budget (June 24, 1958).

JOURNAL OF RESEARCH of the National Bureau of Standards—D. Radio Propagation
Vol. 65D, No. 2, March–April 1961

Ionospheric Motions Observed with High Frequency Backscatter Sounders[1]

Lowell H. Tveten

(November 3, 1960)

Techniques for determining the characteristics of movements of irregularities in the $F2$-region by the use of backscatter records are described. The results of an analysis of backscatter data obtained during December 1952, at Sterling, Virginia, at a frequency of about 13.7 Mc/s are presented and found to be in good agreement with those of other investigators of ionospheric motions.

1. Introduction

Winds and apparent motions in the ionosphere have been the subjects of study by various groups for some time. Different methods have been used. Included among the radio techniques are radio fading patterns [Mitra, 1949; Salzberg and Greenstone, 1951; Chapman, 1953], spaced vertical sounders [Munro, 1948; Munro, 1950; Price, 1954], direction-of-arrival studies [Bramley and Ross, 1951] and others [Meek, 1949; Gerson, 1950; Manning, Villard, and Peterson, 1950; Maxwell and Little, 1952; Maxwell and Dagg, 1954; Maxwell 1954; Clark and Peterson, 1956; McNicol and Webster, 1956; Wells, 1957; Valverde, 1958]. It is the purpose of this paper to present another method for studying ionospheric motions and give some results and conclusions obtained using this method.

Use of backscatter sounding was made at Stanford University to study motions of sporadic-E clouds [Clark and Peterson, 1956] and very large disturbances in the $F2$-layer [Valverde, 1958]. The present paper also deals with $F2$-layer disturbances, some of which appear to be like those studied by Valverde [1958] although the technique of analysis used is different. For the most part, however, the paper deals with disturbances of a smaller size and the technique of determining the motion is new. Some preliminary results of this investigation were mentioned by Wells [1957].

2. General Background and Method

2.1. Backscatter Sounding and Recording Techniques

For those unfamiliar with backscatter sounding a brief explanation is in order. A pulse of radio frequency energy is radiated from a directive antenna. This pulse travels outward until it encounters the ionospheric layers at one of which it may be reflected back down to earth. At the ground the energy is reflected and scattered in all directions. Some of the scattered energy retraces its original path and arrives back at the transmitting point at a delay time equal to the length of the path traveled by the pulse divided by the appropriate average group velocity of the wave over the path. This scattered energy is then channeled through a radio pulse receiver whose output is recorded.

For the purpose of this experiment the radiating antenna should not have appreciable directivity in the vertical plane but should be fairly directive in the horizontal plane. Under these conditions backscatter energy is obtained from the edge of the "skip zone" for the particular frequency and ionospheric layer involved and on to greater ranges with general decrease in intensity as the range increases [Hartsfield, Ostrow, and Silberstein, 1950; Dieminger, 1951; Peterson, 1951; Hartsfield and Silberstein, 1952; Silberstein, 1953; Shearman, 1956].

One of the methods of recording backscatter is the "range-time" recording technique in which an oscilloscope trace is triggered at the same time as the transmitter pulse, and the backscatter signal from the receiver is used to intensity modulate the trace. This trace is then photographed by a moving film camera in which the image of the trace on the film is perpendicular to the direction of film travel. The result is a plot of backscatter range as a function of time. Another method is the plan position indicator (PPI) display in which an intensity modulated oscilloscope trace rotates in synchronism with a rotating directive antenna. A photograph of one complete rotation then displays the scatter characteristics as a function of azimuth.

The range-time sweep may be gated to display only a certain portion of the total range. This is done to display greater detail of backscatter signal. An example of this type of record is shown in figure 1. The delay time is given in milliseconds and represents twice the slant range to the ground scattering point divided by the speed of propagation. The time base is in hours. For this particular record a pulse length of about 70 μsec was used and the antenna was a large terminated rhombic.

The record shows that backscatter has a quite complicated structure as far as amplitude versus range is concerned. The immediately striking feature of the record is that the amplitude peaks tend to

[1] Contribution from Central Radio Propagation Laboratory, National Bureau of Standards, Boulder, Colo.

574930—61——1

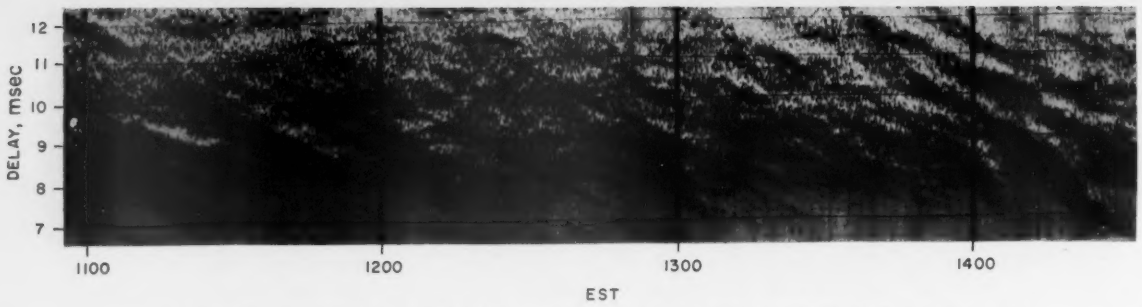

FIGURE 1. *Backscatter record made at Sterling, Virginia on 13.7 Mc/s at azimuth 282°, November 9, 1955.*

maintain themselves over relatively long periods of time but change in range during that time. This is the feature which is taken as evidence of ionospheric motions and the characteristics of these "ripples" in the backscatter are used to interpret the nature of the motions.

2.2. Quantitative Basis for Deduction of Motion Characteristics From Backscatter Records

A focusing phenomenon is necessary for the formation of amplitude peaks. Where along the path followed by the pulse does the focusing occur? Focusing regions below the ionospheric reflection point should be equally effective whether they occur on the near side or far side of the ionospheric reflection point with respect to the transmitter. However, the magnitude of the apparent motion of the focusing region as deduced from the backscatter ripples will be different depending upon the side on which the focusing region is assumed to be located. The difference in these magnitudes will become greater as the height above ground of the focusing region becomes smaller. The analysis of the ripples gives no evidence of effects of motions below the $F2$-region.

The analysis of the ripples was done on the assumption that the focusing takes place at reflection layer heights and, since the scatter involved was all $F2$-propagated, this height was taken as 300 km. The comparison of motion characteristics derived on this assumption with motion characteristics found by other workers further served to justify the focusing height chosen.

If the focusing phenomenon occurs at the reflection heights, it is convenient to treat the problem in rather simple terms. Figure 2 is an exaggerated diagram of the backscatter path geometry. The transmitted pulse travels the path from the transmitter, T, to the ionospheric reflection point at M at a height, h, above the ground and then down to the ground at R where it is scattered. Some of the scattered energy retraces the path back to T. The delay time, t, between transmit time and time of scatter return is given by

$$t=\frac{4s}{300} \text{ msec.} \qquad (1)$$

where s is in kilometers.

If a focusing region exists at M, there will be an intensification of backscatter amplitude at the corresponding delay time. If the focusing region at M is moving, the delay time of the scatter intensification will increase or decrease depending upon whether the ionospheric great circle distance D, shown in figure 2, is increasing or decreasing.

The relationship between D and delay time, t, is given in figure 3 for a height of 300 km according to the equation

$$D=(r+h)\ \cos^{-1}\frac{r^2+(r+h)^2-(75t)^2}{2r(r+h)}. \qquad (2)$$

If D were changing uniformly, and if the units of the abscissa in figure 3 were divided by the rate of change of D, the plot would be one of delay time versus time which is in the form of a backscatter range-time recording. The curve would then represent a ripple changing range on a backscatter range-time recording. In practice, the $F2$-propagated backscatter did not occur at delay times less than 6 or 7 msec for the frequencies used in this experiment so the curve at smaller delays may be disregarded. At greater delays the curve is essentially a straight line.

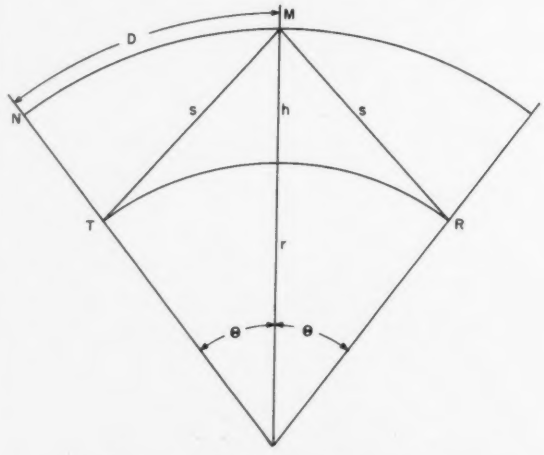

FIGURE 2. *Backscatter path geometry.*

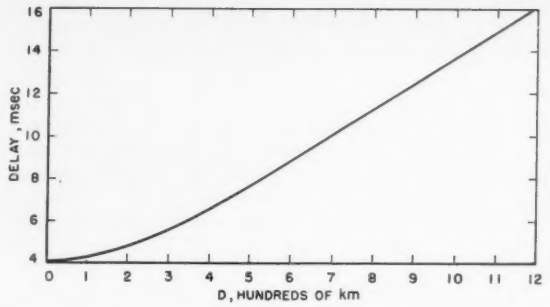

FIGURE 3. *Backscatter delay as a function of the distance, D, of the F layer reflection point.*

Since the speed of the motion is of interest, it is desirable to know the change of D as a function of time, T, for a particular ripple. This is obtained by scaling the slope of the ripple, $\frac{\Delta t}{\Delta T}$, from the range-time recording and multiplying by the reciprocal of the average slope of the delay time versus D curve, $\frac{1}{\frac{\Delta t}{\Delta D}}$, over the delay interval covered by the ripple. As the curve is essentially straight over the range of delay times likely to be encountered, this last quantity may be considered constant and used with all range-time slopes scaled. In other words

$$\frac{\Delta D}{\Delta T}=\frac{\Delta t}{\Delta T}\frac{1}{\frac{\Delta t}{\Delta D}}. \tag{3}$$

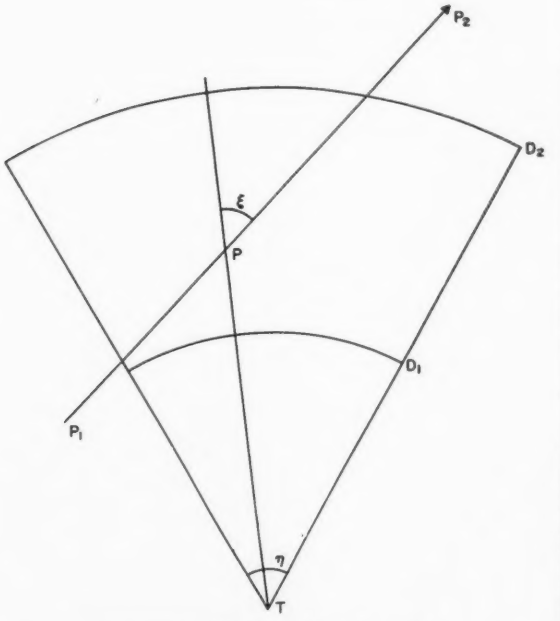

FIGURE 4. *Blob model path geometry.*

If D is in kilometers, T is in hours, and t is delay time in milliseconds, $\frac{\Delta D}{\Delta T}$ is in kilometers per hour. $\frac{1}{\frac{\Delta t}{\Delta D}}$ was calculated at 82.5 km/msec.

This quantity $\frac{\Delta D}{\Delta T}$ represents only the speed of the focusing irregularity toward or away from the transmitting point. Because of the beamwidth of the antenna, it is possible for the irregularity to travel across the beam and the resulting $\frac{\Delta D}{\Delta T}$ scaled would not necessarily be the true speed of the focusing area. How to arrive at the true speed of the focusing area depends upon the model one assumes for this irregularity.

The apparent separations of the focusing irregularities are obtained by scaling the difference in D for two consecutive irregularities on the record at the same time. This is accomplished by measuring the delay time difference in milliseconds at any time and then multiplying by 82.5 km/msec. If two are not visible at the same time, it may be necessary to project the slope of the first one in order to obtain a simultaneous range reading.

The ripples are classified according to whether they represent motions away from the transmitter or motions toward the transmitter. These two groups must be treated separately.

2.3. Focusing Models and Mechanisms

There are two principal models which focusing irregularities may follow. The first is one whose effect is about the same regardless of the azimuth of approach by the sounder pulse. This may be termed the "blob" model as a reflecting blob would exhibit this characteristic. The other may be termed the "long front" model. This would be described as a "wrinkle" in the surface of the reflecting layer extending for a relatively large lateral distance along the front.

In considering the scatter characteristics which these models would provide it is convenient to consider figure 4 in which the area between arcs D_1 and D_2 subtending the antenna beamwidth, η, is the area within which ionospheric reflection and focusing must take place.

a. Blob Model

The blob model will be considered first. In figure 4, let p be a point along the path p_1p_2 followed by a focusing blob moving at a uniform speed, v. The slope of the trace on the backscatter record varies as $v\cos\xi$ as p is allowed to move uniformly along p_1p_2. During the observation time ξ may vary as much as η degrees (in fig. 4 the total variation is about 0.7η). Thus, uniform motion along any straight path through the observation area (except a radial from T) will result in a curved ripple on the backscatter record. For a path crossing the area transversely the ripple will start with a negative slope and end with a positive slope. For radial

paths, cos $\xi=1$, so the slope is constant and equal to v.

There are three kinds of information which can be obtained directly from the scaling of the backscatter ripples. These are the distributions of apparent speeds, the average apparent speed, and the total number of ripples observed per unit time as a function of the antenna azimuth.

If there is an overall preferred direction for the blob motion over the entire area of observation, and further, if there is a certain distribution of the speeds which is the same for all directions of blob motion so that only the number of moving blobs may vary with direction of motion, the above mentioned quantities should vary in the following manner. Without distinguishing between motions toward or away from the transmitter the apparent speed distribution and its average should shift to lower values as the direction of the antenna beam shifts from the preferred direction of blob motion around to 90° and then they should increase again as the beam approaches 180° to the preferred direction.

The number of blobs observed in a given period of time depends upon the size, shape, and orientation of the observation area with respect to the direction of blob travel. For instance, if the distance D_1D_2 in figure 4 were reduced to one-half of that shown, the number of blobs observed moving across the beam would be less than the number observed moving along the beam provided that the blob densities for the two directions of motion were about equal. The motions across the beam would then be discriminated against in the speed distributions. The relative effectiveness of the experimental arrangement for counting blobs moving in a given direction will be designated as the "blob interception cross section" for the given direction. It varies with differing ionospheric conditions and therefore may vary with azimuth.

If the blob interception cross section for any antenna azimuth is approximately constant for all directions of blob travel, the total number of blobs observed per unit time should be about the same at all azimuths. However, if the blobs are separated according to whether their apparent motion is toward or away from the transmitter, then the number having outward motion should be maximum at the antenna azimuth corresponding to the preferred direction. Conversely, the number with inward motion should be maximum at 180° to the preferred direction.

In the actual records, ripples with very low apparent speed were often not scaled because of the difficulty of separating them from other effects. This tends to reduce the total number of blobs counted per unit time and to bias the average apparent speeds toward higher values, particularly for those azimuths at right angles to the preferred direction of blob motion.

If there is sufficient geographical variability in the motion characteristics, some or all of the expected characteristics stated above will be partially or completely masked and any distinguishing features of a particular model may disappear.

b. Long Front Model

The next model to be considered is the long front model. Here the focusing irregularity is considered to lie along a straight line. The motion of this irregularity which may be detected is that perpendicular to its own length. The irregularity is considered to be capable of focusing energy anywhere along its length and regardless of the angle at which the incident beam approaches. This might be difficult to realize in any real case but the concept is useful here.

Figure 5 is similar to figure 4 except that in this case a long front FF′ is moving through the area under observation in the direction of the arrow. Each increment of the front within the beam is focusing some energy. It is seen from the diagram that there would be focused energy returned from nearly minimum scatter range to maximum scatter range, but there is an additional focusing effect due to the concentration in a small increment of delay time of the energy focused by the adjacent elements of the irregularity in the vicinity of p where a radial from T is perpendicular to the front. This concentration should be enough to produce an observable ripple on the scatter record. It is concluded that with this model the ripples appearing on a record for a given antenna azimuth would represent only those irregularities moving along a radial included within the beamwidth, η. The apparent speeds would then be very nearly the actual speeds of the irregularities.

If $n(\theta, v)$ represents the overall density distribution function of the front velocities, then the observed distribution function $N_\theta(v)$ for motions away from the transmitter in a given azimuth, θ, is given by

$$N_\theta(v)=\int_{\theta-\eta/2}^{\theta+\eta/2} n(\theta, v)d\theta. \qquad (4)$$

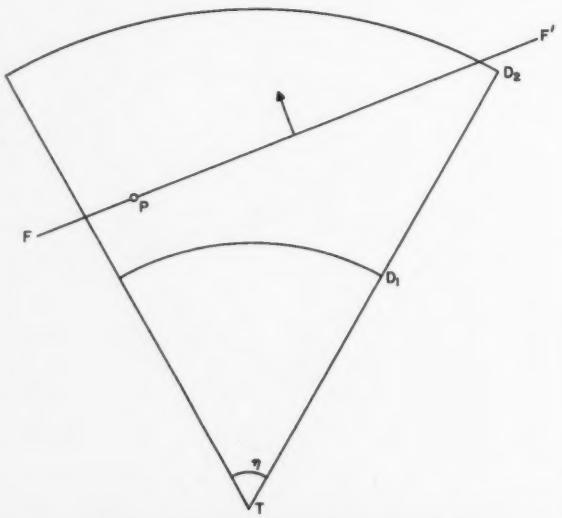

FIGURE 5. *Long front model path geometry.*

$N_{\theta+\pi}(v)$ would be the corresponding distribution for motions toward the transmitter.

If the functional dependence of the distribution on v were the same over the whole geographic area and for all directions (in other words $n(\theta, v)=p(\theta)\ q\ (v)$), this feature should be apparent in the observed distributions for the different antenna azimuths. The average scaled speeds and the normalized speed distributions would be the same for all azimuths. Differences would be indicative of geographic and/or directional variations.

With an overall preferred direction for travel, the number of irregularities moving away from the transmitter should peak as for the blob model at the antenna azimuth corresponding to the preferred direction. Similarly for motions toward the transmitter, there should be a peak at 180° from the preferred direction. Strictly speaking, the converse is not necessarily true. It may not be said with each model that peaks occurring in the manner described definitely imply the existence of an overall preferred direction of travel for the focusing irregularities. However, it seems unlikely that the velocity distributions for different azimuths should be completely different and yet coincidentally provide data as described above.

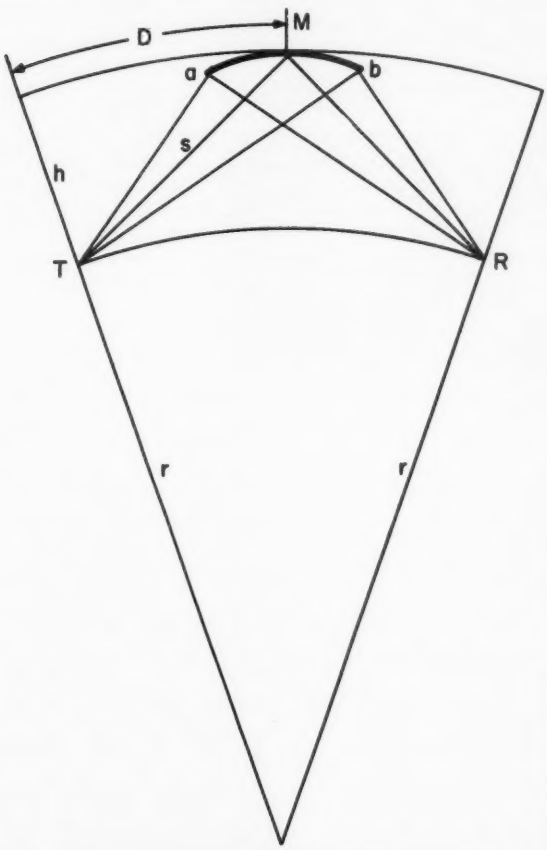

FIGURE 6. *Elliptical focusing mechanism geometry.*

c. Focusing Mechanism

So far nothing has been said regarding the actual focusing mechanism for either the blob or the long front model. A simple mechanism which can be adapted to either model is illustrated in figure 6. Let the element of curved reflecting surface aMb be a part of an ellipse of major axis $2s$ whose focal points are at T and R. Thus, all of the pulse energy radiated into the vertical angle aTb reaches R at exactly the same delay time. The same thing happens to energy scattered over the return path. This energy acts as if it were all transmitted over the path TMR.

It is pertinent to obtain some quantitative information using some of the parameters characteristic of the system used in the experiment. Let the distance ab be 200 km as would be appropriate if the wrinkles were separated by about 400 km. Let $s=900$ km which is a figure near the midrange for most of the scatter observations in this experiment. Let $h=300$ km. The tilt at a or b would then be about 2.5° with respect to the horizontal at the midpoint M, or about 1.7° referred to the horizontal at points a and b. According to Bramley and Ross [1951], such a tilt would not be unusual.

To obtain a simple and fairly adequate blob model one has only to rotate the segment aMb about the line TR. This results in a dimple in the ionospheric surface which will focus energy and behave in general as the blob model. To obtain the long front model one requires the surface generated by moving the segment aMb perpendicular to the plane of the diagram. However, exact adherence to the elliptical model is unnecessary to obtain substantial focusing. Any concave downward surface will give more or less focusing.

The blob type model constructed this way focuses the energy in a roughly circular area about a point on the ground at R. The long front model focuses the energy about a long straight line on the ground. However, as the energy approaches the front at other than perpendicular incidence, the focusing becomes more diffuse about this line as the off perpendicularity increases. This is due to the effectively lateral tilts which operate for obliquely approaching beams. Hence, there is additional reason beyond the clustering of echoes at similar time delays for concluding that backscatter ripples observed with this model include only those fronts moving along a radial included within the antenna beamwidth.

Neither the blob nor the long front mechanism for focusing would be strongly dependent upon frequency. Figure 7, which is a pair of backscatter records made simultaneously on two different backscatter sounders on two different frequencies, indicates by the great similarity in ripple structure that the actual focusing mechanism is not strongly frequency dependent.

These focusing models are not original suggestions since variations of this idea have been used by several workers [Pierce, Mimno, 1940; Munro, 1950; Munro, 1953b; Baird, 1954; Bibl, Harnischmacher, and

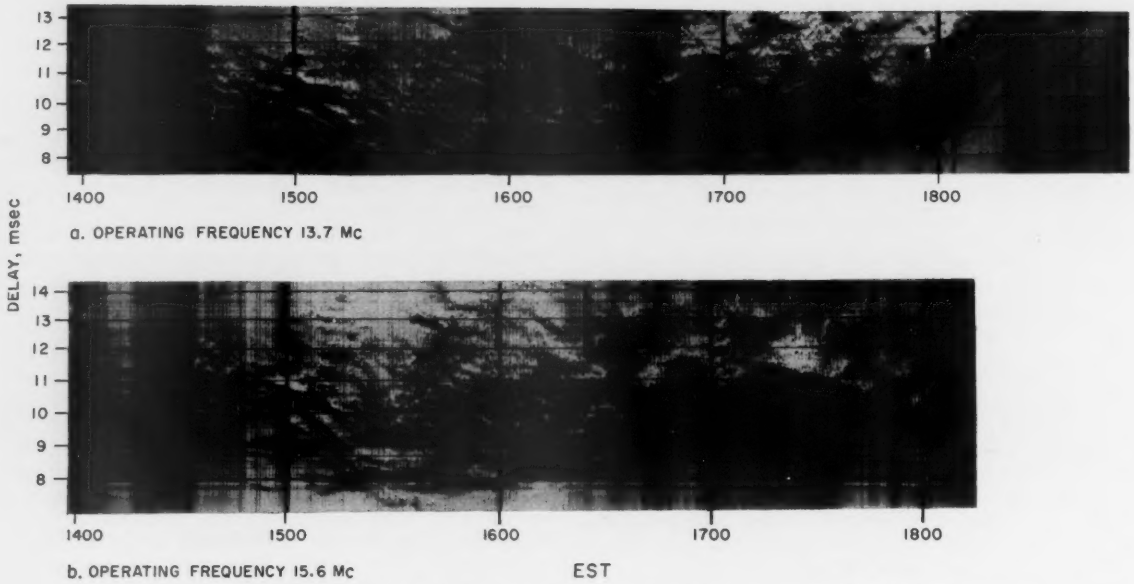

FIGURE 7. *Backscatter records made simultaneously at Sterling, Virginia at azimuth 282°, November 21, 1955.*

Rawer, 1954; Munro and Heisler, 1956a] to explain their observations.

2.4. Experimental Details and Sample Records

The data for the experiment were obtained for the most part from a month's run of the backscatter sounder during December of 1952 at the National Bureau of Standards Field Station at Sterling, Va. The records were made for a different purpose and, consequently, not all of the parameters were ideal for the investigation described here. The records consisted of 16-mm pictures of the backscatter PPI representation described earlier. The transmitter provided pulses of 40 μsec duration and about 500 kw peak power at a repetition rate of 25 pulses per second. The frequency was about 13.7 Mc/s. The antenna was a combination of two vertically polarized three-element Yagis [Silberstein, 1957], and it was rotated continuously at the rate of one rotation per minute.

A T–R network [Hartsfield and Silberstein, 1954] permitted the use of the same antenna for transmitting and receiving. A PPI oscilloscope was electromechanically geared to the antenna such that the oscilloscope trace maintained the same azimuthal bearing as the antenna. A 16-mm motion picture camera was used to photograph the PPI scope face at the rate of one film frame per complete antenna rotation. The result was a series of pictures of the backscatter range and azimuthal characteristics in a precise time sequence.

Figure 8 shows a series of PPI photographs selected at 5 min intervals between 0930 and 1030 EST, December 3, 1952. A little over 30 msec of range are shown on the records with 10 msec separating the intense range markers. The backscatter intensifications are evident here, but the change of range of these intensifications is not at all obvious as it is in the range-time record of figure 1. Any one intensification is evident at quite constant range over a relatively large azimuthal spread. Because of the antenna beamwidth even a small focusing area would be seen over a wide azimuthal range and actually any focusing mechanism will result in the arc-like structure. Thus, motion characteristics are very difficult to obtain using only the PPI pictures directly.

For the scaling of motion characteristics the range-time record mentioned earlier is more convenient. Fortunately, a method of obtaining synthetic range-time records from PPI photographs was available. Briefly, this consisted of using a motion picture projector to project the PPI pictures upon a small translucent slit oriented at the desired azimuth of the PPI image. Viewed from the opposite side from the projector this appeared simply as an intensity modulated trace which could be photographed by a range-time camera in the usual manner. Time marks were made by flashing a light on the slit at intervals determined by a microswitch operated by notches previously cut in the edge of the 16-mm film.

Range-time records for twelve azimuths, 0, 30, 60, 90, 120, 150, 180, 210, 240, 270, 300, and 330 deg were made in this way. Because of the 40° beamwidth between the effective backscatter half-power points, there is some overlap in this arrangement, but it does not materially affect the results. A set of the twelve range-time records for December 3, 1952 is shown in figure 9. A total of about 20 msec or 3000 km of slant range is shown in the records. The base line may appear at ranges somewhat higher than

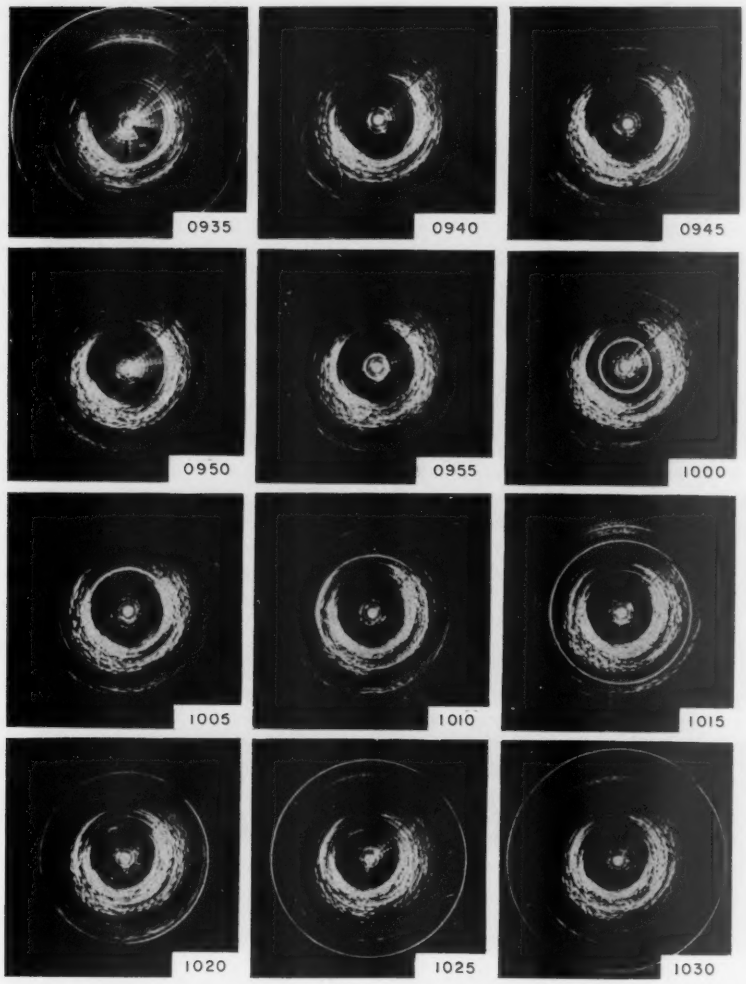

FIGURE 8. *PPI pictures at five minute intervals from 0930–1030 EST, December 3, 1952.*

zero. The time base is not quite uniform from azimuth to azimuth and this had to be taken into account in the scaling procedure. The regular diagonal pattern sweeping from the base line to the top of the record on all azimuths was caused by an interfering pulse from another experiment.

The PPI pictures of figure 8 cover the period between 0930 and 1030 EST on the range-time records in figure 9. The ripples changing in range are very obvious on the range-time recordings whereas, as mentioned earlier, the ripple characteristics are well hidden in the PPI pictures. In some azimuths, notably those around 120°, there seem to be very uniform and regular systems of motion in evidence. The rate of change of range and the separations of the ripples are quite uniform. An interesting feature here is that 180° away, at 300°, there is a regular set of ripples displaying opposite slopes, indicating that the ionospheric motions are in the same general direction in the two regions observed although these regions are separated by over 1500 km.

2.5. Basis for Analysis of Very Large-Scale Disturbances

Ripples in the scatter return are not the only evidence of ionospheric motions in backscatter records. The set of range-time recordings in figure 9 illustrates another evidence of motion. On the 180° azimuth at 1137 EST there is an indentation in the leading edge of the scatter return at about 9 msec delay time. This represents a change in ionization density or reflection height of the ionosphere, in the region where the skip rays are reflected, which causes the skip distance to increase.

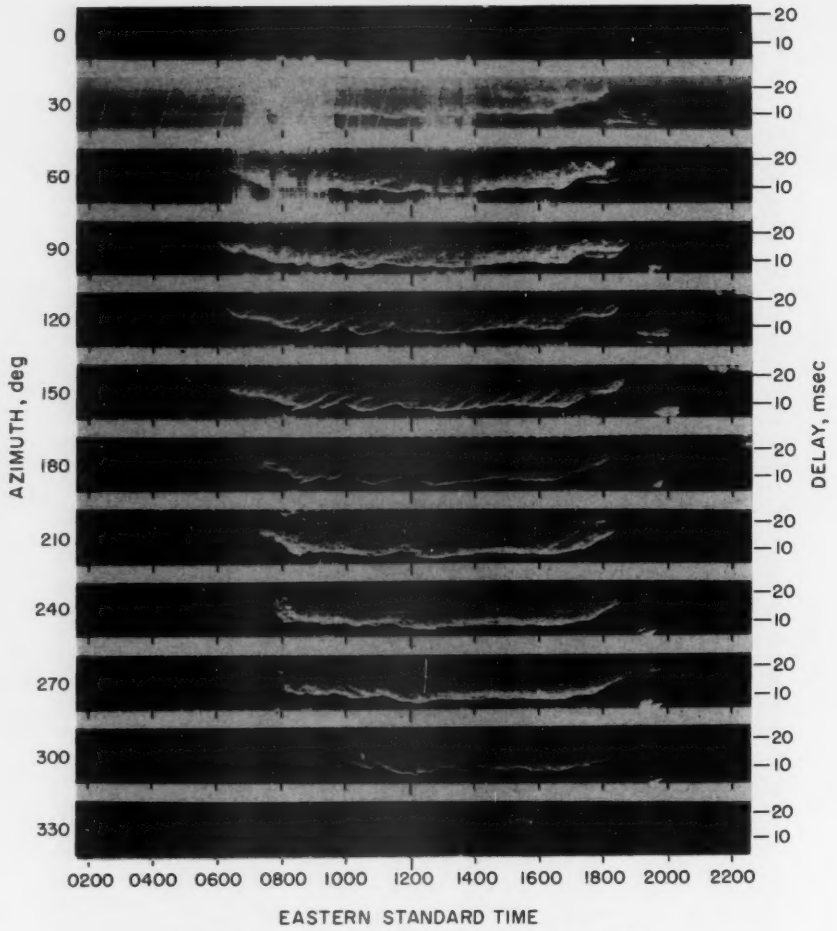

FIGURE 9. *Range-time records for December 3, 1952.*

Indentations are also evident at the neighboring azimuths but at progressively earlier times as the separation from 180° increases in both directions. This situation must be the result of a very large traveling disturbance in the ionosphere. Judging from the widths (durations) of the indentations and the relative time displacements at the different azimuths, this disturbance was about 1500 km across (parallel to the apparent direction of motion) and was traveling from north to south at a speed of about 1500 km/hr. During the thirty days of data several of these disturbances occurred as evidenced by similar patterns of indentations, although the number of azimuths displaying the indentation varied considerably from one disturbance to another. These very large disturbances are probably of the same type as those studied by Valverde [1958] using backscatter PPI pictures and vertical sounders. His measurements indicated some fronts over 4000 km long. The use of range-time records makes the job of analyzing these disturbances perhaps a little easier than the use of the PPI pictures alone.

It should be emphasized that, in contrast to the previously discussed backscatter ripple associated disturbances, of which several may be found in the ionospheric reflection area for the antenna beam at a given time, the very large disturbance is effective over practically the entire beam reflection area at one time. Therefore, the effect of the disturbance is observed regardless of the relationship of the direction of the wave front to the direction of the antenna beam.

A set of range-time records such as in figure 9 involves ionospheric conditions over an annular ring with a minimum radius of about 600 km to a maximum radius of approximately 1200 km about a point above the transmitter as a center. Because of the sequential times of appearance of the indentations at the different azimuths the disturbance appears to be a wide but very long and relatively straight band, and is therefore observed at widely separated geographical points. If the disturbance is nearly symmetrical, the peak of the indentation should indicate the time and range at which the

midline of the disturbance crosses the point whose coordinates are determined from the azimuth and range of the peak of the indentation. Thus, by scaling the time and range of the peak of the indentation for at least three different azimuths, one can obtain a set of geographic locations over which the disturbance passed and the times at which this happened from which one may estimate the magnitude and direction of motion of the disturbance perpendicular to its length.

The problem reduces approximately to one in which a straight wave front passes over points of coordinates X_iY_i in a plane at a time T_i. These quantities are related to the actual problem such that

$$X_i=R_i \cos \theta_i \tag{5}$$

$$Y_i=R_i \sin \theta_i \tag{6}$$

where R_i is obtained from figure 3 and is the value of D corresponding to the delay time to the peak of the indentation on the range-time record and θ_i is the azimuthal bearing at which the range-time record was made. T_i is the time at which the peak of the indentation appeared on the record. Figure 10 illustrates the case.

If the front passes over points 1 and 2 at times T_1 and T_2, the quantity

$$\frac{[(X_1-X_2)^2+(Y_1-Y_2)^2]^{1/2}}{|T_1-T_2|}=v'_{12} \tag{7}$$

is related to the velocity of the front perpendicular to itself by the expression

$$v'_{12}=v \sec (\psi_{12}-\phi) \tag{8}$$

where v is the magnitude of the front velocity, ϕ is its direction, and ψ_{12} is the bearing of point 1 from point 2 when $T_1>T_2$ or the bearing of point 2 from point 1 when $T_2>T_1$. ψ_{12} is obtained from the expression,

$$\tan \psi_{12}=\frac{Y_1-Y_2}{X_1-X_2} \tag{9}$$

when $T_1>T_2$, and from

$$\tan \psi_{12}=\frac{Y_2-Y_1}{X_2-X_1} \tag{10}$$

when $T_2>T_1$. The proper quadrant for ψ_{12} is obtained, of course, by strict observance of the signs of the numerator and the denominator of the equation. Using other points, one obtains other values of v'. If there are N points, there are obtained $\frac{N(N-1)}{2}$ different values of v' each with a particular value of ψ. Having two values of v' and the corresponding ψ's, one may calculate values for v and ϕ by solving two equations of the form of (8) simultaneously. The value of ϕ obtained this way is either the true ϕ or $\phi \pm 180°$. Because of the geometry of the problem the true ϕ may differ from the two ψ's by a maximum of 90° which then makes only one choice possible.

For the present treatment when there were five or more azimuths of observation for a given disturbance, the resulting ten or more values of v' and corresponding ψ were plotted and fitted to a curve of equation (8) by inspection thus yielding the v and the ϕ for the disturbance in question. When there were only three or four observation points, the method of solution by simultaneous equations was used in which every possible set of two values of v' and corresponding ψ's was used to obtain values which were averaged for a final value of v and ϕ.

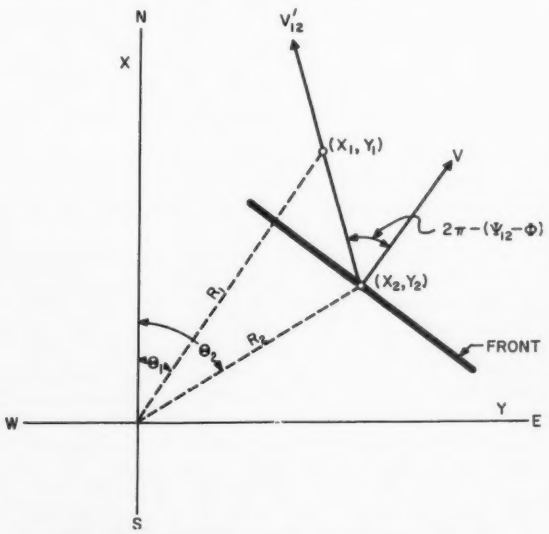

FIGURE 10. *Geometry for very large disturbances.*

3. Results

3.1. Statement of Results

These results are limited in that they were obtained principally during the daylight hours of December 1952. A typical daily set of range-time backscatter records is shown in figure 9. This should be remembered when comparing these results with those of others who have worked at different seasons and different times of day.

Figure 11 is a plot of the average number of ripples per hour of time in which $F2$-propagated ground scatter was evident, for motions away from the transmitter and for motions toward the transmitter, as a function of antenna azimuth. The uncertainty intervals are equal to twice the standard deviation of the mean. The two azimuthal scales are offset by 180° in order to make more obvious the similarity of the two curves.

With either the blob model or the long front model for the focusing irregularities, the distribution shown could result from an approximately uniform directional distribution over the entire area, peaking in

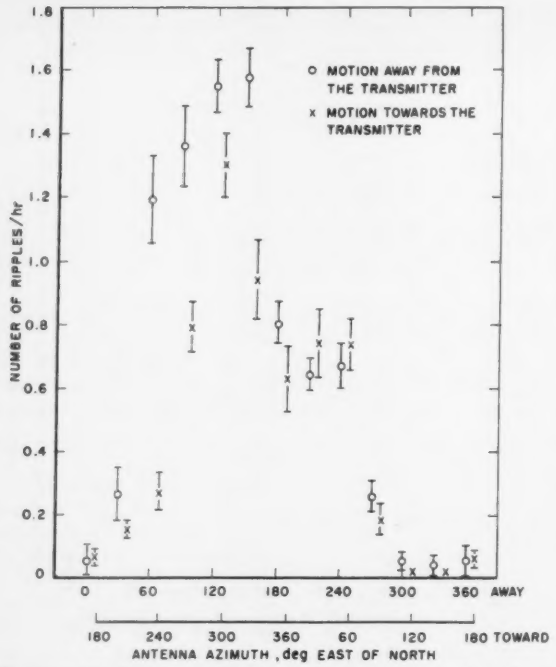
NUMBER OF RIPPLES/hr
o MOTION AWAY FROM THE TRANSMITTER
x MOTION TOWARDS THE TRANSMITTER
0 60 120 180 240 300 360 AWAY
180 240 300 360 60 120 180 TOWARD
ANTENNA AZIMUTH, deg EAST OF NORTH

FIGURE 11. *Number of ripples per hour as a function of azimuth.*
Vertical lines extend to plus and minus the standard deviation of the mean.

the southeast direction. Not only do the peaks for motions away from the transmitter occur at azimuths approximately 180° away from those of the motions toward the transmitter, but the minimums behave in the same way, and in each curve the minimum is displaced about 180° from the maximum. The knee in the curve for outward motion at 180° to 240° is very similar to that for inward motion at 0° to 60°. It seems highly unlikely that this pattern should have occurred unless the directional characteristics of the motions were very similar over the entire area involved.

The variations of the mean apparent speed with azimuth, both for motion toward the transmitter and for motion away from the transmitter, are shown in figure 12. The mean apparent speed for motion toward the transmitter is systematically greater than for motion away from the transmitter. The only explanation of this difference that comes to mind is that it resulted from an idiosyncrasy or unconscious bias in the scaling process, but an investigation failed to reveal it. The azimuthal variations, amounting to 30 to 40 percent, have highest values in the northeast quadrant and lowest values in the southwest quadrant.

According to the long front model (section 2.3.b) the observed average speeds would be the same as the true average speeds for the different directions and geographical areas. If the blob model were the correct one, the true average speed would be greater than the average apparent speed since one would observe only the radial component of actual velocity

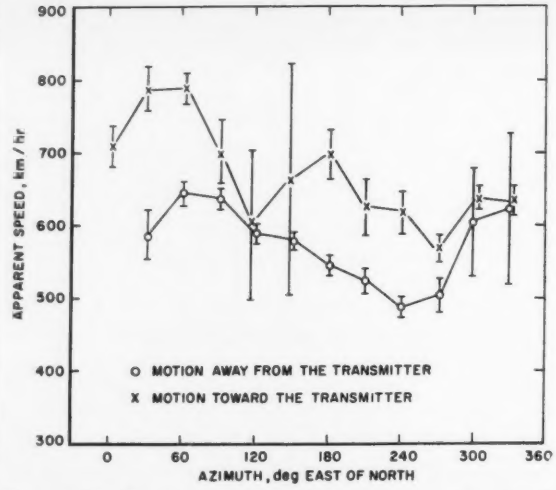
APPARENT SPEED, km/hr
o MOTION AWAY FROM THE TRANSMITTER
x MOTION TOWARD THE TRANSMITTER
0 60 120 180 240 300 360
AZIMUTH, deg EAST OF NORTH

FIGURE 12. *Mean apparent speeds as a function of azimuth.*
Vertical lines extend to plus and minus the standard deviation of the mean. The standard deviation for a single observation varied between 150 and 350 km/hr.

(section 2.3.a), and there would be a tendency for the ratio of apparent to true values to be least in the azimuths at right angles to the preferred direction of motion; i.e., if there were no geographical variations, the average apparent speed would tend to be least in the northeast and southwest quadrants in accordance with the trends of figure 11. Thus the azimuthal variations in figure 12 are not explicable solely in terms of either model, and must be a manifestation of geographical differences in the velocity distribution. As further evidence of geographical differences, the speed distributions for the northeastern azimuths have a much greater proportion of cases in which the speeds fall into the extreme 1200 to 2500 km/hr range. On the other hand, calculations have indicated that the azimuthal variation expected on the basis of the blob model would be small for the directional distribution implied by figure 11, and might be masked by the geographical variations. Thus it must be concluded that these results do not lead to a preference for either the blob model or the long front model for the irregularities.

Figure 13 is a speed distribution histogram showing the number of ripples per 40 km/hr interval for all azimuths taken together. The median value is 580 km/hr.

It should be pointed out that the distribution histogram as plotted in figure 13 and the distributions used to calculate the results in figure 12 are based on the number of irregularities moving through the ionospheric area under observation by the antenna beam in a given period of time. The number observed at any particular speed in a given period must be the actual density of irregularities possessing this speed in the ionosphere multiplied by the product of the speed and the effective cross section for interception of moving irregularities by the antenna beam. The more basic physical quantity is the distribution of the actual number of irregularities per unit area of

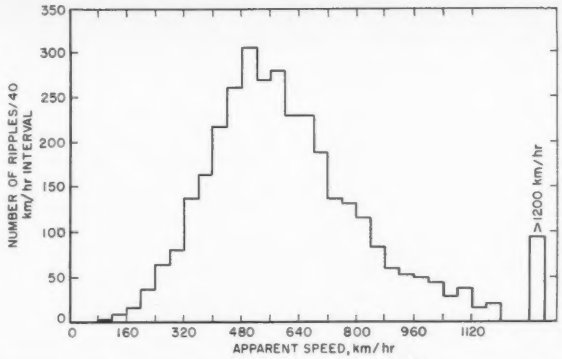

FIGURE 13. *Apparent speed distribution for ripples from all azimuths taken together.*

ionosphere as a function of speed. In the absence of exact knowledge of the interception cross section but assuming it to be constant, one may obtain a relative distribution by taking the distribution histogram as shown in figure 13 and dividing the number per speed interval by the middle speed of the interval. The results given in figure 13 calculated on this basis are given in figure 14. This provides a more symmetrical distribution and provides a new median value of 500 km/hr.

If there were irregularities with no motion or very little motion, they were not detected in scaling the records because of the difficulty in distinguishing them from other effects. Neither type of distribution would then give the proper relationship at very low values of apparent speed.

Range-time records from each azimuth showed relatively brief periods during which the backscatter seemed rather smooth without outstanding irregularities and without evidence of motion. The proportion of time that this occurred during the period of regular $F2$-propagated backscatter averaged about five percent.

No significant difference was found between the speed characteristics of the ripples during the morning when the skip distance was moving into shorter ranges, during the evening when the skip was moving out to greater ranges, and during the remainder of the day between these periods when the skip distance was relatively constant.

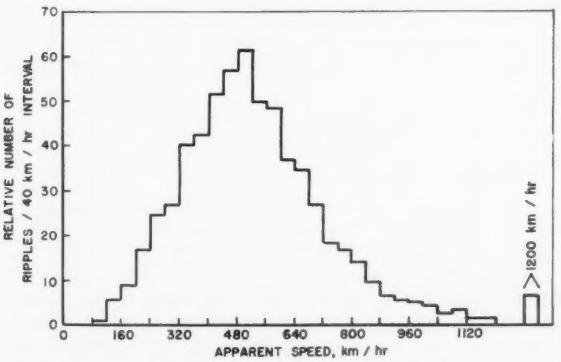

FIGURE 14. *Relative apparent speed distribution corrected to represent the ripple density per unit ionospheric surface area.*

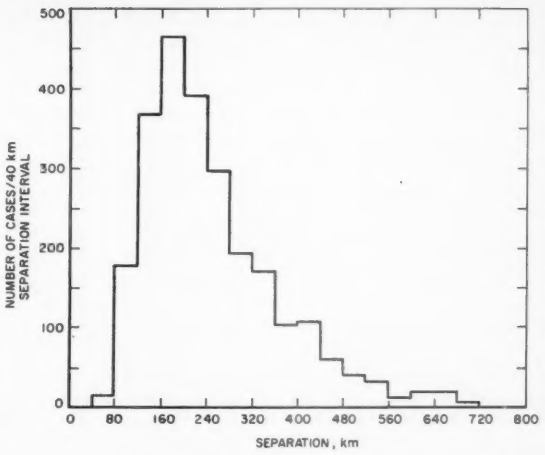

FIGURE 15. *Apparent ripple separation distribution for all azimuths taken together.*

On a given record, most of the ripples appear in groups and exhibit some differences but seem to be a part of a system. Some appear singly and are separated from their neighbors by relatively large intervals of time and space.

Figure 15 is a distribution histogram giving numbers of separations observed per 40 km interval of separation for all azimuths of observation taken together. Values in the range 160 to 200 km were most frequent. Because of the uncertainties in scaling the separations as they became larger, separations larger than 720 km were not included.

Figure 16 displays the results of the analysis of the very large-scale traveling disturbances. The circles represent the values obtained by fitting the secant curve to the plot of the observed velocity components. The cross marks represent the values obtained by the type of calculation used when there were only three or four azimuths at which the disturbance was recorded.

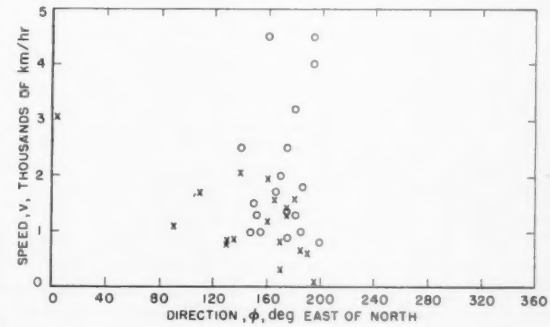

FIGURE 16. *Speed, v, and direction, φ, distribution for very large traveling disturbances.*

The majority of these motions of very large disturbances appear between 120° and 200° east of north and have magnitudes of from 100 km/hr to 4500 km/hr. A few larger values were obtained but were omitted because of the large error possible due to the small time increment between azimuthal appearances of the disturbance. Also in these cases the disturbances showed at only three azimuths. The disturbances which appeared at a large number of azimuths vary between 800 km/hr and 4500 km/hr in magnitude. This agrees very well with the results of Valverde at Stanford University for October, November, and December of 1952. His results fall between 750 km/hr and something over 2000 km/hr. It is interesting to note that Valverde's results fall principally between 180° and 225° east of north while those obtained at Sterling, Virginia fall between 120° and 200° east of north. This may indicate an association with the earth's magnetic field.

3.2. Comparison of Results

The results of the backscatter ripple analysis may be summarized by saying that most of the apparent speeds are included in the interval 80–1000 km/hr with a median speed of 580 km/hr or 500 km/hr depending upon whether the distribution is that observed or that calculated from that observed for the population per unit ionospheric area. The overall direction of motion indicated is toward the southeast. The separations between those focusing irregularities which seem to be a part of a system fall between 40 km and 700 km for the most part with the most frequent value at 180 km.

Nearly all of the methods used to measure ionospheric movements in the $F2$-region result in the same range of apparent velocities as obtained in this investigation. Thus the method depending upon the observation of the fading of radio stars at spaced receivers as reported in papers by Maxwell and Little [1952], Maxwell [1954], Maxwell and Dagg [1954] indicates velocities in the high F-region of 100 to 1200 km/hr. The method of similar fades on close spaced receivers as done, for example, by Salzberg and Greenstone [1951], and Chapman [1953] yields values of 250 to 360 km/hr for the F-region. The irregularities utilized with these methods are quite small being of the order of a very few kilometers at the most.

The type of irregularities responsible for backscatter ripples is evidently the same type as those investigated by Munro [1948, 1949, 1950, 1953 a, b], Munro and Heisler [1956 a, b], Price [1954], and McNicol and Webster [1956] in Australia, Beynon [1948], Bramley and Ross [1951], and Bramley [1953] in England, and Pierce and Mimno [1940], and Toman [1955] in the United States. Most of Munro's results indicate a velocity of 300 to 600 km/hr. Price indicates magnitudes of 120 to 1200 km/hr with a most frequent value around 600 km/hr. Beynon obtained a velocity around 430 km/hr and Bramley has found values from 90 to 1300 km/hr with the maximum number of observations about 540 km/hr. Pierce and Mimno derived speeds of 600 to 800 km/hr.

Of particular interest for comparison purposes is the work of Toman [1955] in New England which covered a period including December of 1952. He used a pulse transmitter on fixed frequency and measured the ionospheric movements by observing the relative time delays between the appearances of $F2$ virtual height changes on a system of spaced receivers. Since the distance separating his location from Sterling, Va., is only a few hundred kilometers, it would be expected that the results should be quite similar. He found monthly speed averages ranging from 250 to 600 km/hr with 580 km/hr recorded for December 1952. During the month of December the preferred direction of movement was 117° east of north according to these results. These measurements were made during the daylight hours, and the similarity to the backscatter results is very great.

Munro has reported a generally northeast direction of movements for winter months and a generally southeast direction during the summer with a very fast shift occurring during the period around the equinox. Price has reported a roughly similar result. These are daytime results. Bramley found motion toward the east by day and toward the west at night with a shift at about 1400 u.t. Radio star methods [Maxwell and Little, 1952; Maxwell and Dagg, 1954; and Maxwell, 1954] usable at night indicate a direction toward the west before about midnight and toward the east after that time.

Bramley has reported the wavelengths of the quasi-periodic irregularities in the $F2$-region as varying between 25 and 425 km with a maximum number at 150 km. The vertical amplitude varied up to 4 km. The lateral dimension of one irregularity extended beyond 200 km. Munro and his coworkers in Australia indicated quasi-periodic disturbances with periods of 10 to 60 min and with lateral dimensions perpendicular to the direction of motion exceeding 50 km and some extending to several hundred. These disturbances occur at the rate of one or two per hour with a dimension of 100 to 500 km across a given disturbance. They also point out that the irregularities exhibit a forward tilt with height in the direction of motion with the result that they are noticed first at the higher levels. According to Price the disturbances range from a few to 200 km across and that perpendicular to the direction of travel they exhibit a broad wave front. The number of disturbances observed per hour averaged about 0.4.

McNicol and Webster explained their results in terms of fronts several hundred kilometers long and in the form of a wide inverted trough or in steps with strongly curved edges.

Pierce and Mimno accounted for their results in terms of ionospheric wrinkles of depth less than 5 km and widths of the order of 100 to 500 km.

While the backscatter results did not indicate a preference for either the blob or long front model, some of these other observations point to the possibility that at least a large share of the disturbances are of the long front type.

These are a few results obtained by other workers investigating the problem of ionospheric motions.

A much more complete survey of the subject (up to 1954) is given by Briggs and Spencer [1954].

4. Conclusion

The use of a backscatter sounder appears to be a relatively simple method of determining the direction and apparent speeds of ionospheric motions when these characteristics are fairly uniform over the relatively large area observed by the sounder. Even in the absence of uniformity useful information about the magnitudes of apparent speeds is still available from a single sounder. It has been shown that the results obtained using the backscatter sounder are in good agreement with those obtained using other methods.

Future experimentation should be directed toward determining the form and focusing characteristics of the ionospheric irregularities themselves. The use of variable pulse lengths, different antenna beams, and concerted action by several sounders of both the vertical and backscatter type should yield considerable information about these irregularities.

The author expresses his appreciation to Richard Silberstein, who suggested the investigation, for his continuing interest and suggestions, to William Hartsfield who devised the method for making synthetic range-time recordings and under whose project leadership the backscatter run was made, and to Thomas Gautier for the many helpful suggestions and valuable discussions.

5. References

Baird, K., High multiple radio reflections from the F–2 layer of the ionosphere at Brisbane, Australian J. Phys. **7,** No. 1, 165–175 (Mar. 1954).

Bibl, K., E. Harnischmacher, and K. Rawer, Some observations of ionospheric movements, Report of the Physical Society Conference on Physics of the Ionosphere, London, 113–118 (Sept. 1954).

Beynon, W.J.G., Evidence of horizontal motion in region F–2 ionization, Nature **162,** 887 (Dec. 4, 1948).

Bramley, E. N., Direction finding studies of large scale ionospheric irregularities, Proc. Roy. Soc. [A] **220,** 39–61 (Oct. 22, 1953).

Bramley, E. N., and W. Ross, Measurements of the direction of arrival of short radio waves reflected at the ionosphere, Proc. Roy. Soc. [A] **207,** 251–267 (June 22, 1951).

Briggs, B. H., and M. Spencer, Horizontal movements in the ionosphere, Reports on Progress in Physics **17,** No. 254, 245–280 (1954).

Chapman, J. H., A study of winds in the ionosphere by radio methods, Can. J. Phys. **31,** No. 1, 120–131 (Jan. 1953).

Clark, C., and A. M. Peterson, Motion of sporadic-E patches determined from high-frequency backscatter records, Nature **178,** 486–487 (Sept. 1, 1956).

Dieminger, W., The scattering of radio waves, Proc. Phys. Soc. **64,** No. 2, 142–158 (Feb. 1951).

Gerson, N. C., Large scale sporadic movements of the D-layer of the ionosphere, Nature **166,** 316–317 (Aug. 19, 1950).

Hartsfield, W. L., S. M. Ostrow, and R. Silberstein, Backscatter observations by the Central Radio Propagation Laboratory—August 1947 to March 1948, J. Research NBS **44,** 199–214 (Feb. 1950).

Hartsfield, W. L., and R. Silberstein, A comparison of C–W field intensity and backscatter delay, Proc. IRE **40,** No. 12, 1700–1706 (Dec. 1952).

Hartsfield, W. L., and R. Silberstein, Low-pass duplexing system for high-frequency pulse transmitters, Tele-Tech **13,** No. 2, 76 (Feb. 1954).

Manning, L. A., O. G. Villard, and A. M. Peterson, Meteoric echo study of upper atmosphere winds, Proc. IRE **38,** No. 8, 877–883 (Aug. 1950).

Maxwell, A., Investigation of F region drift movements by observations of radio star fading, Report of the Physical Society Conference on Physics of the Ionosphere, London, 166–171 (Sept. 1954).

Maxwell, A., and M. Dagg, A radio astronomical investigation of drift movements in the upper atmosphere, Phil. Mag. [7] **45,** 551–569 (June 1954).

Maxwell, A., and C. G. Little, A radio-astronomical investigation of winds in the upper atmosphere, Nature **169,** 746–747 (May 3, 1952).

McNicol, R. W. E., and H. C. Webster, A study of "Spread-F" ionospheric echoes at night at Brisbane, II. Interpretation of range spreading, Australian J. Phys. **9,** No. 2, 272–285 (June 1956).

Meek, J. H., Sporadic ionization at high latitudes, J. Geophys. Research **54,** No. 3, 284–285 (Sept. 1949).

Mitra, S. N., A radio method of measuring winds in the ionosphere, Proc. Inst. Elec. Engrs. **96,** Part III, No. 43, 441–446 (Sept. 1949).

Munro, G. H., Short period changes in the F region of the ionosphere, Nature **162,** 886–887 (Dec. 4, 1948).

Munro, G. H., Short-period variations in the ionosphere, Nature **163,** 812–814 (May 21, 1949).

Munro, G. H., Traveling disturbances in the ionosphere, Proc. Roy. Soc. [A] **202,** 208–223 (July 7, 1950).

Munro, G. H., Traveling disturbances in the ionosphere: Diurnal variation of direction, Nature **171,** 693–694 (April 18, 1953a).

Munro, G. H., Reflexions from irregularities in the ionosphere, Proc. Roy. Soc. [A] **219,** 447–463 (Oct. 1953b).

Munro, G. H., and L. H. Heisler, Cusp type anomalies in variable frequency ionospheric records, Australian J. Phys. **9,** No. 3, 343–358 (Sept. 1956a).

Munro, G. H., and L. H. Heisler, Divergence of radio rays in the ionosphere, Australian J. Phys. **9,** No. 3, 359–372 (Sept. 1956b).

Peterson, A. M., The mechanism of F-layer propagated backscatter echoes, J. Geophys. Research **56,** No. 2, 221–237 (June 1951).

Pierce, J. A., and H. R. Mimno, The reception of radio echoes from distant ionospheric irregularities, Phys. Rev. **57,** No. 2, 95–105 (Jan. 15, 1940).

Price, R. E., Traveling disturbances in the ionosphere, Report of the Physical Society Conference on Physics of the Ionosphere, London, 181–190 (Sept. 1954).

Salzberg, C. D., and R. Greenstone, Systematic ionospheric winds, J. Geophys. Research **56,** No. 4, 521–533 (Dec. 1951).

Shearman, E. D. R., The technique of ionospheric investigation using ground backscatter, Proc. Inst. Elec. Engrs. **103,** pt. B, No. 8, 210–223 (March 1956).

Silberstein, R., High frequency scatter sounding experiments at the National Bureau of Standards, Science **118,** 759–763 (December 25, 1953).

Silberstein, R., The long-distance horizontal radiation pattern of a high-frequency antenna, IRE Tran. on Antennas and Propagation **AP–5,** No. 4, p. 397 (Oct. 1957).

Toman, K., Movement of the F region, J. Geophys. Research **60,** No. 1, 57–70 (March 1955).

Valverde, J. F., Motions of large-scale traveling disturbances determined from high-frequency backscatter and vertical incidence records, Radio Propagation Laboratory, Stanford Univ. Sci. Rept. No. 1 (May 21, 1958).

Wells, H. W., Large-scale movements of the layers, Proceedings of Polar Atmosphere Symposium, Part 2: Ionospheric Section, (Pergamon Press, 1957). (Also published as a special supplement to the J. Atmospheric and Terrest. Phys., 33–40, 1957.)

(Paper 65D2–109)

JOURNAL OF RESEARCH of the National Bureau of Standards—D. Radio Propagation
Vol. 65D, No. 2, March–April 1961

Relationship Between Red Auroral Arcs and Ionospheric Recombination[1]

G. A. M. King and F. E. Roach

(August 11, 1960)

A "monochromatic" (6300 A) auroral arc, observed photometrically to be north of Boulder, Colo., has been identified with oblique echoes on ionograms taken near Boulder. The auroral emission is explained in terms of a great enhancement of ionospheric recombination. The recombination process is shown to depend on the density of molecular nitrogen in the ionospheric *F* region; the change in nitrogen density during and after auroral activity, responsible for the change in recombination rate, is ascribed to the combined effects of heating and mixing of the atmosphere at the lower ionospheric heights.

1. Introduction

On the night of 27–28 November 1959, magnetic and auroral activity occurred over a large part of the United States. The general character of the activity can be judged from the variation of the horizontal component of the earth's magnetic field recorded at Boulder, Colo. (see fig. 1). Visual observers, especially in the northwestern United States, reported auroral structure during the evening, and, in particular, bright aurora with red in the northern sky was seen from Boulder about 0600 u.t. (Z).

Instrumental coverage of the period was excellent, and included (1) all-sky camera observations, (2) photometric observations of the green (5577 A) and the red (6300 A) auroral lines at three stations in the southwestern United States, (3) ionospheric soundings, including special recordings near Boulder in the low frequency range, 50 kc/s to 2 Mc/s, and (4) measurement of fluxes of high-energy particles in the outer Van Allen zone during several passes of Explorer VII.

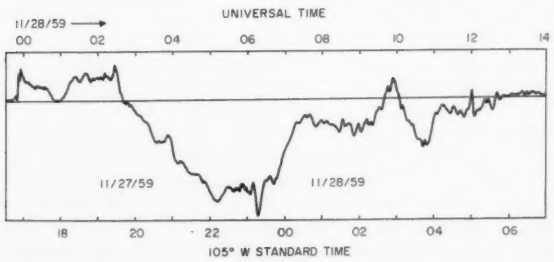

FIGURE 1. *Plot of the horizontal component (H) of the earth's magnetic field at Boulder during the 27–28 November 1959 period.*

Full scale equals 330 gamma.

In this paper, we discuss the relationship between the photometric observations of a red arc and the ionospheric soundings. We hypothesize that the red emission is due to enhanced ionospheric recombination and draw semiquantitative support for the hypothesis from the observational data.

2. Photometric Data

The photometric equipment at Fritz Peak (near Boulder) was put into operation at 0410 Z and continued in use throughout the night until 1310 Z. Observations were made with a birefringent filter photometer in the three colors, 5577 [OI], 6300 [OI], and 5893 [NaI]. The forbidden oxygen radiations (5577 and 6300) were active throughout the night. Two classes of activity occurred, and for convenience we will classify them as follows:

(1) *RG.* In this class, both the red (6300) and the green (5577) emissions are enhanced in intensity.

(2) *R.* In this class the emission forms an arc which is selectively enhanced in the red with no apparent increase in the intensity of the green emission.

It is tempting to think of *RG* as regular auroral activity, since both the red and green lines are characteristic features of auroras in general. The properties of *R*-arcs are described in several recent papers; Barbier [*1*][2] discussed their occurrence and general nature, while Roach and Marovich [*2*, *3*] gave detailed descriptions of two *R*-arcs.

On this particular night, the *RG* activity covered a wide range of intensity (see fig. 2) whereas the *R* activity went through slow and ponderous changes. The general impression from figure 2 is that after 0700 Z, when the *R* data were no longer contaminated by the strong *RG* background, there was a tendency of monotonic decay in the *R* activity with a resurgence at 0925 Z.

[1] Contribution from Central Radio Propagation Laboratory, National Bureau of Standards, Boulder, Colo.

[2] Italicized figures in brackets indicate the literature references at the end of this paper.

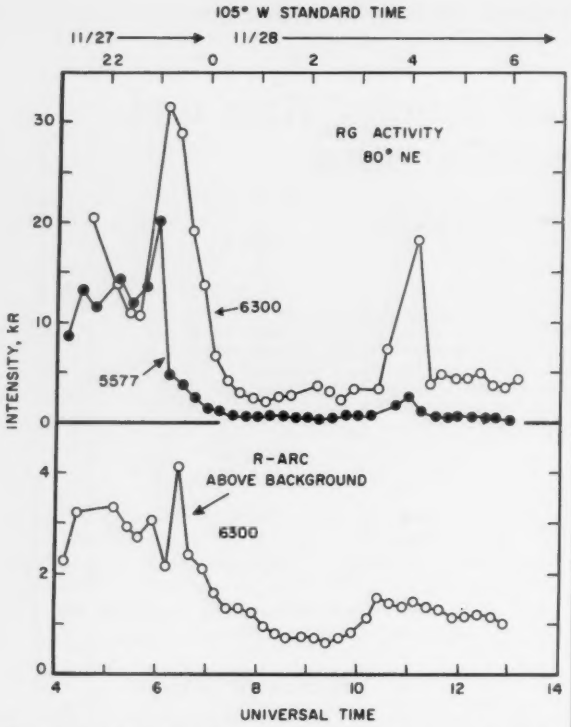

FIGURE 2. *Intensity changes of the RG activity near the northeast horizon (above) and of the R-arc (below) during the night of 27–28 November 1959.*

The height and geographical position of the *R*-arc have been determined in a cooperative study by workers from Fritz Peak (Colo.), Cactus Peak (Calif.), and Sacramento Peak (N. Mex.) [4]. By triangulation, they find a mean height of about 400 km. With this value and the angular data from the Fritz Peak records the arc's geographical position has been deduced; the results are shown in figure 3. At the same time, its width in latitude was determined to be about 500–600 km.

3. Ionospheric Data

Ionospheric records were taken half-hourly at Boulder, 26 km from Fritz Peak. Figure 4 shows the record at 0730 Z, together with a diagram setting out the salient features of the ordinary wave reflections.

A conspicuous feature of this ionogram is the spread echo above the main trace. As the *F* region totally reflects all waves traveling vertically in this frequency range, it is not possible that the spread echo be overhead at a greater height than the normal layer; therefore, the spread trace must be due to echoes received obliquely from a large irregularity in the *F* layer some distance from the observing station. Further considerations, based on the conditions necessary for reflection, suggest that the irregularity is at about the same height as the layer giving the vertical echoes.

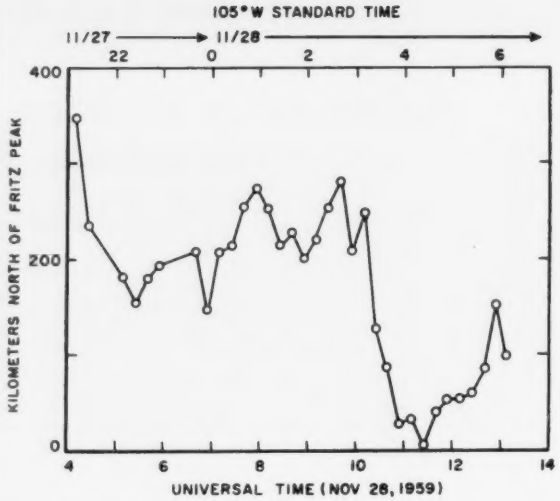

FIGURE 3. *Position of the R-arc of 27–28 November 1959 with respect to Fritz Peak*

Ordinate indicates kilometers north of Fritz Peak for an assumed height of 400 km.

Unfortunately, because of the large effects of ionospheric refraction, it is not possible to determine the distance to the irregularity. However, these refraction effects (which also determine the virtual height, h', of the vertical reflection) will to some extent be canceled when we take the ratio of the virtual ranges to the oblique and to the overhead echoes. A very crude measure, then, of the zenith angle, z, of the irregularity is given by,

$$\sec z = 1 + \frac{\Delta s}{h'} \qquad (1)$$

where Δs is indicated on figure 4 and h' is the virtual height of the overhead echo at 2 Mc/s where the results are least affected by differences between the electron distribution in the irregularity and in the overhead *F* layer. This "zenith angle" was determined from all the ionograms between 0700 and 1200 Z, and it is plotted on figure 5 together with the angle to the *R*-arc determined directly from the photometric records. The parallelism of the two curves suggests immediately that the irregularity and the *R*-arc are associated, especially in view of the fact that the height of the arc places it in the *F* region. This conclusion has been reinforced by a study of the temporal association of oblique echoes and *R*-arcs, using ionograms from Fort Monmouth, White Sands, and Boulder, for nights in September 1957 and December 1959.

An important observation which can be made from figure 4 is that the electron density in the irregularity is *less* than in the overhead trace. In other words, the *R*-arc is associated with a local decrease in the ionization of the *F* region.

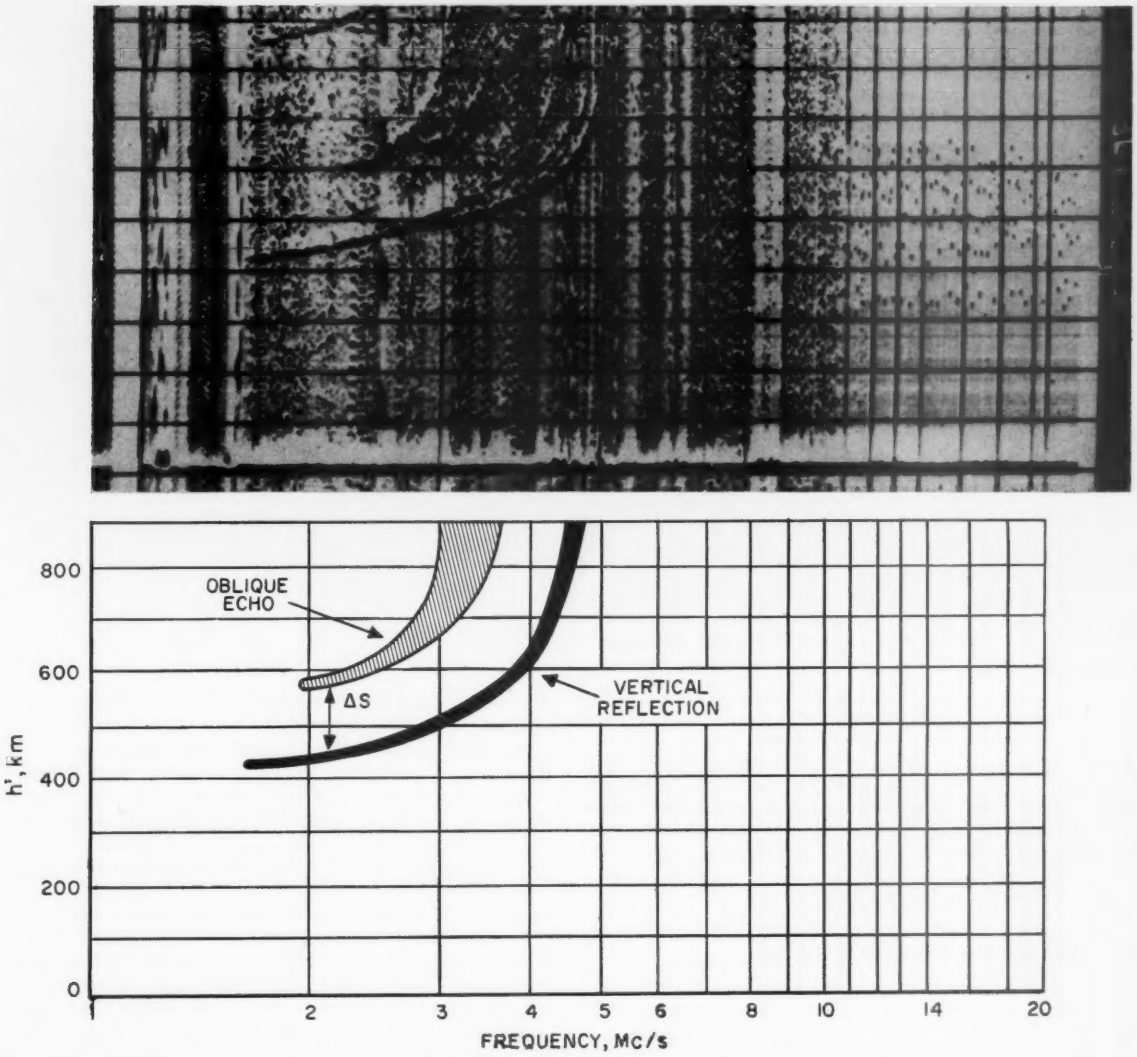

FIGURE 4. *Ionogram made at Boulder at 0730 Z.*
The lower diagram illustrates the essential features.

For testing the theoretical deductions discussed later, we needed electron density profiles. Fortunately, besides the normal ionograms covering frequencies above 1 Mc/s, there were special records over the frequency range 50 kc/s to 2 Mc/s, made at a field station 23 km from Boulder and 13 km from Fritz Peak. By using both sets of records, we were able to get profiles by real height analysis free from the serious errors of "unobserved ionization." The most reliable profile was that at 0730 Z, as the traces on the ionogram were well defined (see fig. 4). From 0800 to 1000 Z profiles could not be obtained, because of sporadic *E*, and after 1030 Z the traces were diffuse, so that the upper parts of the profiles were unreliable. It must be noted that the electron density profiles apply to the main trace and not to conditions in the region of the irregularity, for which they cannot be obtained.

4. Red Emission Due to Ionospheric Recombination

We will attempt to explain four observational facts which have been presented above:

(1) Occurrence of the *R*-arc after the main phase of the magnetic disturbance.

(2) Steady change of intensity with time.

(3) Strong emission of the red lines of atomic oxygen without measurable emission of the green oxygen line.

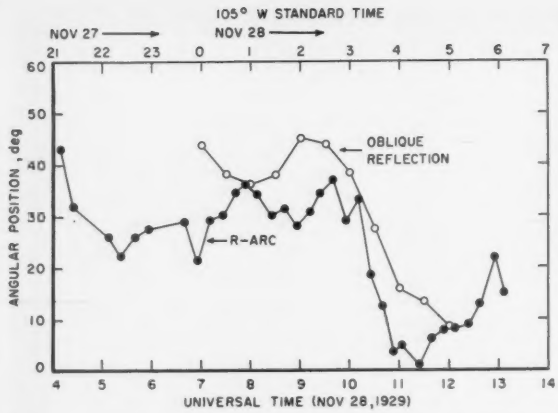

FIGURE 5. *Comparison of the angular position of the R-arc and the oblique echo during part of the night of 27–28 November 1959.*

(4) Association with a local decrease in the ionization of the F region.

Consider the normal process of recombination in the ionosphere. The ionospheric electrons are produced during the daylight hours by photoionization of atomic oxygen.

$$O+h\nu \rightarrow O^+ + e. \tag{2}$$

As the reverse process of radiative recombination is extremely slow, the removal of electrons, both by day and by night, occurs through a two step process [5]. This involves first atom-ion interchange between the ionized oxygen atom and molecular nitrogen,

$$O^+ + N_2 \rightarrow NO^+ + N, \tag{3}$$

and then dissociative recombination,

$$NO^+ + e \rightarrow N^* + O \tag{4a}$$

or

$$NO^+ + e \rightarrow N + O^*. \tag{4b}$$

(Similar reactions involving molecular oxygen will be discussed later and shown to be unimportant for the present purpose.)

Equation (4) gives a relationship between recombination and upper atmospheric emissions; the products of the recombination are excited atoms of nitrogen or oxygen, and when these fall to the ground states they emit characteristic radiations at 5199 [NI] and 6300 (and 6364) [OI].

Given the distributions with height of the electrons and of molecular nitrogen, one can compute the rate of electron recombination, assuming that NO^+ is in equilibrium between reactions (3) and (4). The approximate equation is [6].

$$\frac{\partial n}{\partial t} = -\frac{\alpha n \gamma [N_2]}{\alpha n + \gamma [N_2]} \cdot n \tag{5}$$

where

n is the electron density
$[N_2]$ is the number density of N_2
α is the rate coefficient of reaction (4)
γ is the rate coefficient of reaction (3).

The exothermic energy balance of eq (4) is 2.7 ev, sufficient to provide either an NI quantum (2.36 ev) or an OI quantum (1.96 ev) but not both. Lacking precise data on the relative probability of (4a) and (4b), we shall assume that one OI quantum is emitted for every two recombinations, i.e.,

$$E \approx -\frac{1}{2}\frac{\partial n}{\partial t}. \tag{6}$$

As an illustration, we will apply the above theory to the calculation of the red emission on a quiet night [7]. The time chosen is 0730 Z, 19 November 1958, and the electron density profile is deduced from the Boulder ionograms. The $[N_2]$ profile is derived from atmospheric densities given by Kallmann and Juncosa [8], assuming that the gases are in diffusive equilibrium, and normalized so that $\gamma[N_2]$ at 300 km equals the recombination rate determined by Ratcliffe et al. [9],

$$\beta_{300} = \gamma [N_2]_{300} = 10^{-4}/\text{sec}. \tag{7}$$

For α, we adopt

$$\alpha = 2 \times 10^{-8} \text{ cm}^3/\text{sec}. \tag{8}$$

The electron density profile and the corresponding OI emissions are shown together in figure 6. The integrated emission of 28 rayleighs agrees well with observed values on quiet nights, and in fact Barbier [10] gives a value of 30 rayleighs for 0700 Z at Haute Provence on this night (Fritz Peak data are not available for the time in question). The height of the nightglow, 6300, has not yet been measured, but the evidence places it in the F region [11,12]. The height of maximum emission, 260 km, deduced in this example is very reasonable.

We will now see if the same theory can explain the R-arc on the night of 28 November 1959.

Two additional factors must be considered when converting the calculated values of $\partial n/\partial t$ into emission of 6300 quanta. One is that electron densities in the region of the arc are less than in the overhead F region, yet the latter are used in the computation. The other factor arises from the shape of the arc, broad in comparison with its vertical extent; as the observations were not made vertically, the measured values are larger than those for vertical observation. Neither factor is large, and they are in opposite senses; so, for convenience, we shall assume that they cancel and that a direct comparison can be made between the theory based on eqs (5) and (6) and uncorrected observations.

We suppose also that the abnormally great brilliance of the R-arc is due to *enhanced* recombination: i.e., that β is larger than its normal value in such a ratio that the calculated emission agrees with the observed emission. The test of the theory, then, is based on comparison of the predicted and the observed heights of maximum emission.

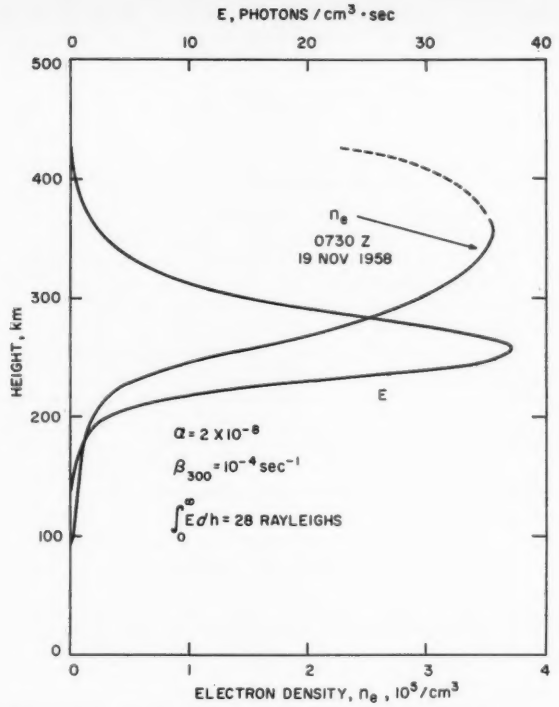

FIGURE 6. *Electron density profile* (n_e) *and the 6300 emission profile* (E) *under quiet conditions.*

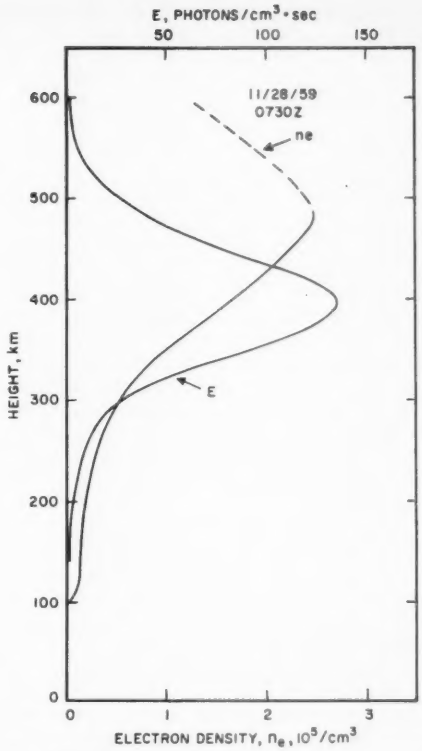

FIGURE 7. *Electron density profile* (n_e) *and the 6300 emission profile* (E) *at 0730 Z on the night of 28 November 1959.* $\alpha = 2x10^{-8}/cm^3$ *sec and* $\beta_{300} = 10^{-1}/sec$.

The integrated emission is 1460 rayleighs.

For the electron density profile at 0730 Z almost perfect agreement is reached if $\beta_{300} = 10^{-1}$/sec. The electron profile and the emission profile are shown together in figure 7. Figure 8 presents the comparisons for the five times studied; in each comparison the curved line gives the theoretical relation between integrated emission and height of maximum emission as β goes through a range of values, while the circles connected by a heavy line give the observed points, corrected and not corrected respectively for background *RG* activity. As in the 0730 Z case, the nearest approach to agreement occurs when β_{300} is about 10^{-1}/sec.

The effect of varying α between 10^{-8} and 10^{-7} cm³/sec was studied, and 2×10^{-8} gave the best overall agreement.

5. Reason for the Increased Recombination

The rate of recombination required to give agreement between the theory and the observations is a thousand times the normal rate. This factor is so large that, in spite of the fair sucess of the theory, we must ask if it is reasonable.

The recombination rate, β, is proportional to $[N_2]$ (see eq (7)). Normally, at 300 km, $[N_2]$ is about a thirtieth of the total number of atmospheric particles; this figure is based on a diffusive level of 105 km in agreement with rocket observations [*13*].

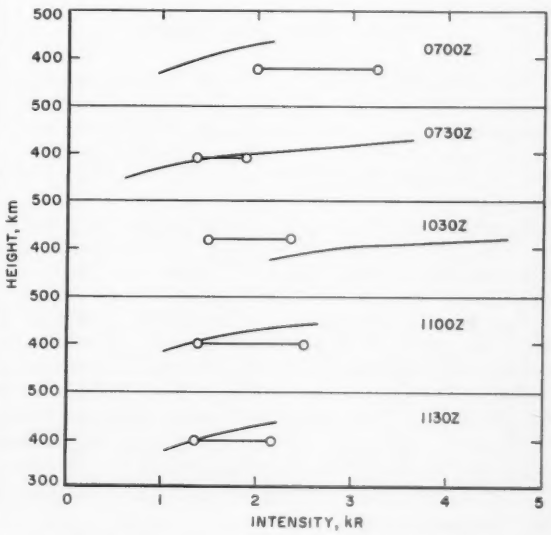

FIGURE 8. *Comparison between theory and observation at five times during the night of 28 November 1959.*

(See text)

However, during auroral activity the atmosphere is heated by the influx of energetic particles. Direct evidence of this has recently been provided by Mulyarchik [*14*] who measured the temperature of the region emitting the 6300 OI line; he found that the temperature increased with the brightness of the display. Now, under normal conditions, the F region is hotter than E. But most of the energy of the aurora is set free in the E region, and, if the increase in F-region temperature is due to conduction of heat from the E region, the normal temperature gradient would have to be reversed. This would call for a very great rise in the E-region temperature, and consequent great changes in atmosphere densities at all higher levels. Another consequence of interest here is the mixing caused by the reversal of the temperature gradient; this raises the diffusive level and so increases the fractional molecular concentration at higher levels. Thus, during and after auroral activity, we expect to find a great increase in $[N_2]$ at F-region heights, and a factor of a thousand does not seem unreasonable.

Three other facts deserve mention in this respect. The first is that the electron density profiles on 28 November 1959 are consistent with atmospheric scale heights in the F region one and a half times normal (compare figs. 6 and 7). Next, satellite drag data indicate an increase in atmospheric densities at times of magnetic storms [*15*]. Finally, Lytle and Hunten [*16*] report that at dawn after an active aurora the N_2^+ emission was very greatly enhanced; while they explain this simply in terms of resonance scattering from N_2^+ ions generated by the aurora, it seems to us more likely in view of the rapid recombination of N_2^+ that the ions were generated by solar ultraviolet light, and that the difference between this and normal dawn lies in the increased $[N_2]$.

6. Further Discussion

Accepting the ideas of the last section, we must ask what effect such a large change in the atmosphere would have on the computation of 6300 emission according to the theory outlined previously; clearly, the $[N_2]$ profile should not be derived in the simple manner used for quiet night conditions. A trial calculation, based on scale heights greater by a factor of one and a half than those of Kallmann and Juncosa [*8*], shows that the emission profile is thickened, but that the height of maximum emission is not greatly altered; more important, however, is that the value of β_{300} needed to give the observed emission is decreased to only 400 times the normal value. As mixing also increases the effective scale height of $[N_2]$, it is likely that on the night of 27–28 November 1959, the increase in β_{300} was much less than the thousand times deduced earlier. The data do not justify a more complete analysis to determine the increase precisely.

When discussing the theory of recombination, we based it on reactions with molecular nitrogen rather than with molecular oxygen as has been supposed by other workers [*7*]. The relevant equations are

$$O^+ + O_2 \rightarrow O_2^+ + O \tag{9}$$

$$O_2^+ + e \rightarrow O^* + O^{**}. \tag{10}$$

We have three reasons for believing that reactions (9) and (10) are not those of interest in the present case. The first is that Dickinson and Sayers [*17*] have recently measured the rate coefficient of reaction (9), obtaining the value 2.5×10^{-11} cm^3/sec; if diffusive separation of the atmospheric gases starts at 105 km [*13*], then $[O_2]_{300}$ is only about 5×10^5/cm^3, which with the measured rate coefficient is much too small to give the observed ionospheric recombination rate. Secondly, the exothermic energy balance of eq (10) is 6.9 ev, enough to give the oxygen green line (4.2 ev) as well as the red lines; whereas there is virtually no green emission in the R-arcs [*3*]. Finally, the temperature measurements mentioned earlier [*14*] also included observations of the NI lines at 5199, and the values are in the same range as those for the OI 6300, indicating that both emissions are from the same height; the reactions involving molecular nitrogen yield both NI 5199 and OI 6300 (see eq (4)). It seems that the R-arcs are not truly "monochromatic," but are only considered so because photometric observations of 5199 are not available.

It is worth mentioning that the rate coefficient of the atom-ion interchange reaction with molecular nitrogen (eq (3)) has been reported in the literature [*18*], but the value, 10^{-8} cm^3/sec, is almost certainly incorrect. The laboratory experiment was for the purpose of testing a mass spectometer, and the rate coefficient was an incidental result; it is likely that no precautions were taken to exclude contamination from the apparatus.

7. Summary

A hypothesis is submitted for the excitation in the upper atmosphere of the oxygen atom to the ^{1}D state. The proposed mechanism involves (1) an atom-ion interchange in which O^+ and N_2 go to NO^+ and N and (2) a dissociative recombination in which NO^+ and an electron yield excited atomic nitrogen or oxygen. The dissociative recombination is sufficiently exothermic (2.72 ev) to excite the oxygen atom to the ^{1}D state (1.96 ev) but not to the ^{1}S state (4.16 ev).

To account for the strong emission of [OI] 6300 in the form of arcs on the equatorward side of general auroral activity it is hypothesized that during an aurora, the rate of the atom-ion interchange is increased by a large increase in the density of molecular nitrogen at F-region heights as a consequence of heating and mixing of the atmosphere below. The predictions of the hypothesis are in agreement with the observed height and intensity of the R-arc on the night of 27–28 November 1959.

One of us (G. A. M. K.) wishes to acknowledge support under the International Geophysical Year program of the National Academy of Sciences while he was a guest worker at the High Altitude Observatory and at the National Bureau of Standards, Boulder, Colo.

8. References

[1] D. Barbier, L'activite aurorale aux bases latitudes, Ann Geophys. **14,** 334 (1958).
[2] F. E. Roach and E. Marovich, A monochromatic low latitude aurora, J. Research NBS **63D,** 297 (1959).
[3] F. E. Roach and E. Marovich, Aurora of October 22/23, 1958, at Rapid City, South Dakota, J. Research NBS **64D,** 205 (1960).
[4] F. E. Roach, J. G. Moore, E. C. Bruner, H. Cronin, and S. M. Silverman, The height of maximum luminosity in an auroral arc, J. Geophys. Research **65,** 3575 (1960).
[5] D. R. Bates and H. S. W. Massey, The basic reactions in the upper atmosphere, Proc. Roy. Soc. (London) **192,** 1 (1947).
[6] J. A. Ratcliffe, Formation of the ionospheric layers F_1 and F_2, J. Atmospheric and Terrest. Phys. **8,** 260 (1956).
[7] J. W. Chamberlain, Oxygen red lines in the airglow: I. Twilight and night excitation processes, Ap. J. **127,** 54 (1958).
[8] H. K. Kallmann and M. L. Juncosa, A preliminary model atmosphere based on rocket and satellite data, Rand Rept. RM 2286 (1958).
[9] J. A. Ratcliffe, E. R. Schmerling, C. S. Setty, and J. O. Thomas, The rates of production and loss of electrons in the F-region of the ionosphere, Phil. Trans. Roy. Soc. **A248,** 609 (1956).
[10] D. Barbier, report to the IGY data centers.
[11] P. St. Amand, Some possible relations between the nightglow and the ionosphere, Ann. de Geophysique **11,** 450 (1955).
[12] M. J. Koomen, R. Scolnik, and R. Tousey, Direct measurement of the night airglow, "The Threshold of Space" 211 (Pergamon 1957).
[13] E. B. Meadows and J. W. Townsend, Diffusive Separation in the Winter Nighttime Arctic Upper Atmosphere, Ann. de Geophysique **14,** 80 (1958).
[14] T. M. Mulyarchik, Interferometric temperature measurements of the upper atmosphere, based on the width of certain emission lines, Izvestiya Akademii Nauk SSSR, Ser. Geofiz. **3,** 449 (1960).
[15] L. G. Jacchia, Corpuscular radiation and the acceleration of artificial satellites, Nature **183,** 1662 (1959).
[16] E. A. Lytle and D. M. Hunten, Dawn enhancement of auroral N_2^+ emission, Can. J. Phys. **38,** 477 (1960).
[17] P. H. G. Dickinson and J. Sayers, Ion charge exchange reactions in oxygen afterglows, Proc. Phys. Soc. (in press).
[18] R. F. Potter, Atom-ion interchange in air, J. Chem. Phys. **23,** 2462 (1955).

(Paper 65D2–110)

JOURNAL OF RESEARCH of the National Bureau of Standards—D. Radio Propagation
Vol. 65D, No. 2, March–April 1961

Fresnel Region Fields of Circular Aperture Antennas[1]

Ming-Kuei Hu

(July 5, 1960; revised July 29, 1960)

A different approach to the Fresnel region field approximation is introduced. Instead of using the conventional truncated power series expansion approximation, the Newton's iteration formula for square root is used. By using such an approximation for circular apertures with tapered illumination of the form $(1-\zeta^2)^n$, the Fresnel region fields can finally be expressed in terms of a new class of functions $W_0^n(\gamma, u)$. The function W_0^0 is shown to be related to the Lommel's functions of two variables, and the function W_0^n is then obtained from the function W_0^{n-1} by a simple recurrence relationship. Field distributions for $n=0, 1, 2, 3, 4$ and at distances $\frac{1}{4}D^2/\lambda$, $\frac{1}{2}D^2/\lambda$, $\frac{1}{2}D^2/\lambda$, D^2/λ, $2D^2/\lambda$, ∞ have been computed and presented as sets of curves. General and quantitative properties of the fields are clearly demonstrated by these curves. It is also shown that the field of any other nonuniform illumination with circular symmetry can be expressed in terms of the fields of the basic illumination of the form $(1-\zeta^2)^n$.

1. Introduction

It is well known that there is a close similarity between diffraction problems in optics and aperture field problems in antenna theory. In optics, two diffraction problems—the diffraction from a single edge or a slit and the diffraction from a circular aperture—have been well treated. These two problems were first solved by Fresnel and Lommel, respectively, in terms of the now so-called Fresnel integrals and Lommel's functions of two variables. The corresponding problems in antenna theory are the Fresnel region fields produced by rectangular and circular apertures. However, in optics, the primary illumination is assumed to be uniform over the aperture, but in antenna theory, the case of nonuniform illumination is of great interest.

For the case of uniform illumination, the analytical methods developed in optics can also be applied to antenna problems. For Fresnel region fields of rectangular apertures, generalizations to include nonuniform illumination through expansions in terms of different basic forms are not too difficult, polynomial and trigonometric sum types of illumination were treated by the author [1].[2] On the other hand, the analysis of Fresnel region fields of circular aperture antennas with nonuniform illumination is considerably more difficult. However, with the use of illumination of the form $(1-\zeta^2)^n$, the Fresnel region field was solved by the present author [1]. A short communication about this result has been published [2]. The complete analysis and numerical results are presented in this paper. A refined but more complicated result for the case of uniform illumination was given by Hansen and Bailin [3]. It may be noted that the corresponding far field problems have been treated by many authors with the use of different basic forms [4, 5, 6, 7], including the form $(1-\zeta^2)^n$ [4, 5] used in this paper.

2. Fresnel Region Approximation

In the study of field distributions of linearly polarized uniform phase plane aperture antennas [8] the following formula [1] or a slightly different form given by Silver [8] may be used as a starting point.

$$E(x,y,z)=\frac{jk}{4\pi}\int_A F(\xi,\eta)\,\frac{e^{-jkr_0}}{r_0}\left(1+\frac{z}{r_0}\right)dA, \tag{1}$$

[1] Contribution from Department of Electrical Engineering, Syracuse University, Syracuse 10, N.Y. This work is part of a project sponsored by Rome Air Development Center under Contract No. AF 30(602)-928 with Syracuse Univ.

[2] Figures in brackets indicate the literature references at the end of this paper.

where

$E(x,y,z)$=the complex magnitude (amplitude and phase) of the electric field intensity at the field point (x,y,z),

$F(\xi,\eta)$=the illumination at the point $(\xi,\eta,0)$ in the apperture A. For uniform phase illumination, $F(\xi,\eta)$ can be taken as a real function of ξ and η,

$r_0=\sqrt{(x-\xi)^2+(y-\eta)^2+z^2}$=the distance between the field point (x,y,z) and the source point $(\xi,\eta,0)$, and

$k=\frac{2\pi}{\lambda}$ with λ=the wavelength.

The coordinate system used for writing formula (1) is given in figure 1. Formula (1) holds for any illumination function $F(\xi,\eta)$ and for apertures of any shape. In the present paper, it is assumed that the aperture is circular and the illumination is of circular symmetry.

For a circular aperture of radius a, as given in figure 2, formula (1) can be rewritten as follows:

$$E(r,\theta,\phi)=\frac{jk}{4\pi}\int_0^{2\pi}\int_0^a F(\rho,\phi')\,\frac{e^{-jkr_0}}{r_0}\left(1+\frac{r}{r_0}\cos\theta\right)\rho\,d\rho\,d\phi' \tag{2}$$

where

$$r_0=\sqrt{(r\sin\theta\cos\phi-\rho\cos\phi')^2+(r\sin\theta\sin\phi-\rho\sin\phi')^2+(r\cos\theta)^2}.$$

The evaluation of the above integral is a very difficult one without further approximation. In order to facilitate its evaluation, different approximations are generally used. Depending upon the approximation used, the result may be classified as the far field approximation, the Fresnel region approximation, etc. The most widely used approach to such approximations is to expand the distance r_0, appearing in the exponential, into a power series involving r, θ, and ϕ. The result obtained, by neglecting all terms of order higher than one or of order higher than two, is generally considered as the far field approximation or the Fresnel region approximation. As far as the remaining r's under the integral sign are concerned, much more crude approximations are satisfactory. If the field point in consideration is not too close to the aperture and θ is not too large, then the factor $1/r_0\,(1+(r/r_0)\cos\theta)$ can be approximated to good accuracy by using the relation,

$$\frac{1}{r_0}\left(1+\frac{r}{r_0}\cos\theta\right)\cong\frac{2}{r}. \tag{3}$$

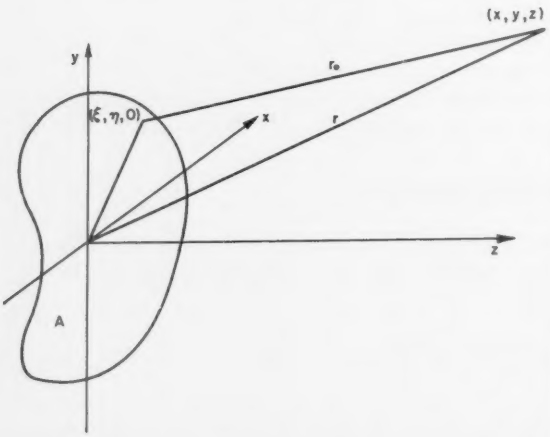

FIGURE 1. *Coordinate system for* A *plane aperture.*

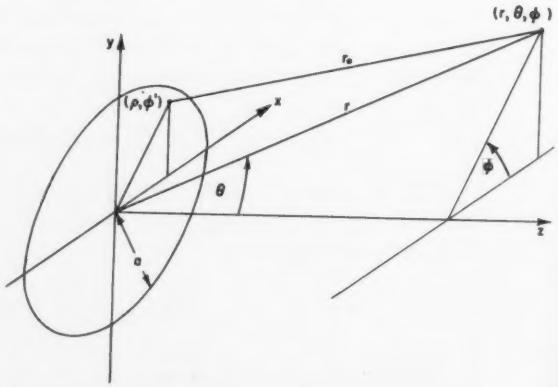

FIGURE 2. *Coordinate system for* A *circular aperture.*

A rather different approach to the Fresnel region approximation is used in the present paper. Instead of using the truncated power series expansion, the well-known Newton's iteration formula for finding square root of a given number is employed. This formula has the following special property. If an approximation B_1, of $\sqrt{A}$ is known to be correct to n significant figures, then the approximation B_2 of $\sqrt{A}$ obtained by using the iteration formula,

$$B_2=\frac{1}{2}\left(B_1+\frac{A}{B_1}\right) \tag{4}$$

will be correct to $2n$ significant figures. If this formula is applied to the approximation of r_0 in Fresnel region, we have

$$r_0\cong\frac{1}{2}\left\{r+\frac{(r\sin\theta\cos\phi-\rho\cos\phi')^2+(r\sin\theta\sin\phi-\rho\sin\phi')^2+(r\cos\theta)^2}{r}\right\}. \tag{5}$$

After simplifying, eq (5) becomes

$$r_0\cong r-\rho\sin\theta\cos(\phi-\phi')+\frac{\rho^2}{2r}. \tag{6}$$

This approximation of r_0 gives a simpler form than that given by Silver [8] and also by Hansen and Bailin [3]. It should be noted that this particular form makes the following relatively simple analysis possible.

Using the approximations (3) and (6), formula (2) gives:

$$E(r,\theta,\phi)=jk\frac{e^{-jkr}}{2\pi r}\int_0^{2\pi}\int_0^a F(\rho,\phi')e^{jk\left[\rho\sin\theta\cos(\phi-\phi')-\frac{\rho^2}{2r}\right]}\rho d\rho d\phi'. \tag{7}$$

If it is further assumed that the aperture illumination $F(\rho,\phi')$ is of circular symmetry, i.e., $F(\rho,\phi')$ can be written as $F(\rho)$; then $E(r,\theta,\phi)$ will be independent of θ and can be denoted by $E(r,\theta)$. Hence we have

$$E(r,\theta)=jk\frac{e^{-jkr}}{r}\int_0^a F(\rho)J_0(k\sin\theta\rho)e^{-jk\left(\frac{\rho^2}{2r}\right)}\rho d\rho. \tag{8}$$

If a normalized variable

$$\zeta=\frac{\rho}{a} \tag{9}$$

is defined, then eq (8) can be written as

$$E(r,\theta)=jka^2\left(\frac{e^{-jkr}}{r}\right)\int_0^1 F(\zeta)J_0(u\zeta)e^{-j\frac{\gamma}{2}\zeta^2}\zeta d\zeta, \tag{10}$$

where

$$u=ka\sin\theta \tag{11}$$

and

$$\gamma=\frac{ka^2}{r}. \tag{12}$$

From eqs (11) and (12) it is clear that $u=\gamma$ implies $r\sin\theta=a$; therefore $u=\gamma$ means that the field point is at a distance, equal to the radius of the aperture, from the aperture-axis.

It is more convenient for the following discussions to rewrite eq (10) as:

$$E(r,\theta)=e^{-jkr}\left(\gamma e^{j\frac{\pi-\gamma}{2}}\right)\int_0^1 F(\zeta)J_0(u\zeta)e^{j\frac{\gamma}{2}(1-\zeta^2)}\zeta d\zeta. \tag{13}$$

3. Uniform Aperture Illumination

For the case of uniform illumination, $F(\zeta)=1$, eq (13) reduces to

$$E(r,\theta)=e^{-jkr}\left(\gamma e^{j\frac{\pi-\gamma}{2}}\right)\int_0^1 J_0(u\zeta)e^{j\frac{\gamma}{2}(1-\zeta^2)}\cdot\zeta d\zeta. \tag{14}$$

In the above equation, the integral may be denoted by $W_0^0(\gamma,u)$,

$$W_0^0(\gamma,u)=\int_0^1 J_0(u\zeta)e^{j\frac{\gamma}{2}(1-\zeta^2)}\,\zeta d\zeta. \tag{15}$$

This integral has an imaginary part as well as a real part. It is closely related to the Lommel's functions of two variables [9]. The Lommel's functions of two variables can be expressed in integral forms as:

$$\begin{aligned} U_1(\gamma,u)&=\gamma\int_0^1 J_0(u\zeta)\cos\frac{\gamma}{2}(1-\zeta^2)\cdot\zeta d\zeta,\\ U_2(\gamma,u)&=\gamma\int_0^1 J_0(u\zeta)\sin\frac{\gamma}{2}(1-\zeta^2)\cdot\zeta d\zeta. \end{aligned} \tag{16}$$

$U_1(\gamma,u)$ and $U_2(\gamma,u)$ are of order one and order two, respectively.

By integrating by parts and using the recurrence relations of Bessel functions, it can be proved that $U_1(\gamma,u)$ and $U_2(\gamma,u)$ may be expanded into the following two series:

$$\begin{aligned} U_1(\gamma,u)&=\left(\frac{\gamma}{u}\right)J_1(u)-\left(\frac{\gamma}{u}\right)^3 J_3(u)+\left(\frac{\gamma}{u}\right)^5 J_5(u)\ \ldots,\\ U_2(\gamma,u)&=\left(\frac{\gamma}{u}\right)^2 J_2(u)-\left(\frac{\gamma}{u}\right)^4 J_4(u)+\left(\frac{\gamma}{u}\right)^6 J_6(u)\ \ldots. \end{aligned} \tag{17}$$

Generalizations of these functions to higher orders are possible, but these generalizations will not be used in the present paper.

In terms of $U_1(\gamma,u)$ and $U_2(\gamma,u)$, we have

$$W_0^0(\gamma,u)=\frac{U_1(\gamma,u)}{\gamma}+j\frac{U_2(\gamma,u)}{\gamma}. \tag{18}$$

Using the above relation for $W_0^0(\gamma,u)$, formula (14) can be written simply as:

$$E(r,\theta)=e^{-jkr}\left(\gamma e^{j\frac{\pi-\gamma}{2}}\right)\cdot W_0^0(\gamma,u). \tag{19}$$

This result is essentially the same as the first term in the series solution of Hansen and Bailin [3]. It can be seen from their figure 6 that the two results are close to each other within the region considered in this paper.

4. Nonuniform Aperture Illumination of the Form $(1-\zeta^2)^n$

If the aperture illumination is assumed to be of the form $(1-\zeta^2)^n$, the field expression can be obtained by substituting $F(\zeta)=(1-\zeta^2)^n$ into eq (13), that gives

$$E(r,\theta)=e^{-jkr}\left(\gamma e^{j\frac{\pi-\gamma}{2}}\right)\int_0^1 (1-\zeta^2)^n J_0(u\zeta)e^{j\frac{\gamma}{2}(1-\zeta^2)}\,\zeta d\zeta. \tag{20}$$

Now if we define

$$W_0^n(\gamma,u)=\int_0^1 (1-\zeta^2)^n J_0(u\zeta)\, e^{j\frac{\gamma}{2}(1-\zeta)}\, \zeta d\zeta \tag{21}$$

then

$$E(r,\theta)=e^{-jkr}\left(\gamma e^{j\frac{\pi-\gamma}{2}}\right)\cdot W_0^n(\gamma,u). \tag{22}$$

When $n=0$, eqs (20) and (22) reduce to eqs (14) and (19), respectively. In other words eqs (20) and (22) include uniform illumination as a special case. For $n\neq 0$, these give the field distributions for the special tapered illumination $(1-\zeta^2)^n$. The integration of the integral (21), or the evaluation of the function $W_0^n(\gamma,u)$, can be carried out by noting the following simple property: If differentiation of $W_0^n(\gamma,u)$ with respect to γ is carried out, we have

$$\frac{\partial}{\partial\gamma}W_0^n(\gamma,u)=\frac{j}{2}\int_0^1 (1-\zeta^2)^{n+1}J_0(u\zeta)\, e^{j\frac{\gamma}{2}(1-\zeta^2)}\, \zeta d\zeta. \tag{23}$$

Equation (23) gives the recurrence relation,

$$W_0^{n+1}(\gamma,u)=\frac{2}{j}\frac{\partial}{\partial\gamma}W_0^n(\gamma,u). \tag{24}$$

In terms of $W_0^0(\gamma,u)$, we have

$$W_0^n(\gamma,u)=\left(\frac{2}{j}\right)^n\frac{\partial^n}{\partial\gamma^n}W_0^0(\gamma,u) \tag{25}$$

or

$$W_0^n(\gamma,u)=\left(\frac{2}{j}\right)^n\left[\frac{\partial^n}{\partial\gamma^n}\frac{U_1(\gamma,u)}{\gamma}+j\frac{\partial^n}{\partial\gamma^n}\frac{U_2(\gamma,u)}{\gamma}\right]. \tag{26}$$

It is possible to derive expressions of $W_0^n(\gamma,u)$ in terms of Lommel's functions of orders higher than two. But as far as numerical evaluation is concerned, it was found that the simplest way is to use eq (26) and the series expansions (17) for $U_1(\gamma,u)$ and $U_2(\gamma,u)$. The series expansions of $(\partial^n/\partial\gamma^n)(U_1(\gamma,u)/\gamma)$ and $(\partial^n/\partial\gamma^n)(U_2(\gamma,u)/\gamma)$, for $n=0,1,2,3$, and 4, are obtained by differentiating the power series of $U_1(\gamma,u)/\gamma$ and $U_2(\gamma,u)/\gamma$, term by term, n times with respect to γ.

5. Results

In the last section, for the aperture illumination of the form $(1-\zeta^2)^n$, the field expression is given by

$$E(r,\theta)=e^{-jkr}\left(\gamma e^{j\frac{\pi-\gamma}{2}}\right)\cdot W_0^n(\gamma,u), \tag{27}$$

where

$$\gamma=\frac{ka^2}{r} \tag{28}$$

and

$$u=ka\sin\theta. \tag{29}$$

$E(r,\theta)$ in eq (27) can always be rewritten in the following form:

$$E(r,\theta)=Ae^{j2\pi\phi} \tag{30}$$

where A is the amplitude and $2\pi\phi$ is the phase angle in radians.

Plots of the aperture illumination $(1-\zeta^2)^n$ for $n=0,1,2,3,4$, are given in figure 3. The field distribution curves, both amplitude A and phase $2\pi\phi$, are computed for the following cases (see fig. 4):

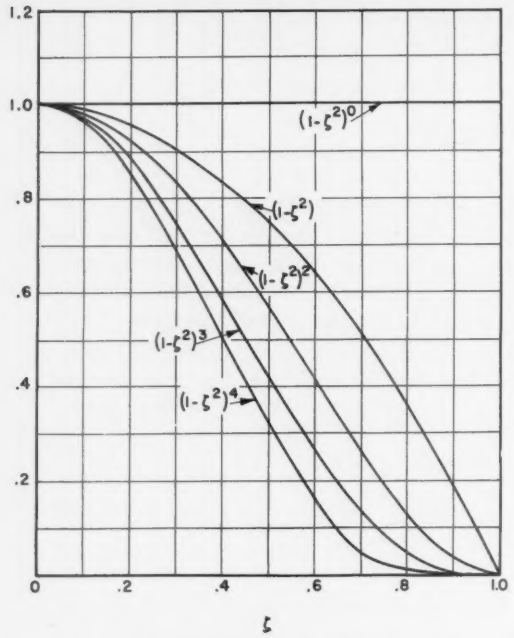

FIGURE 3. *Aperture illumination distributions, uniform and tapered.*

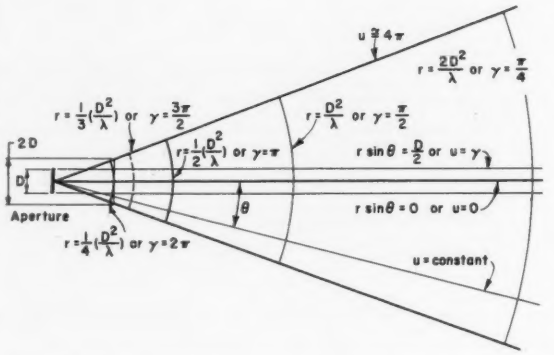

FIGURE 4. *Fresnel region, in which field distributions have been computed.*

(i) Field distributions along the circular arcs:

$$r=\frac{1}{4}\left(\frac{D^2}{\lambda}\right), \frac{1}{3}\left(\frac{D^2}{\lambda}\right), \frac{1}{2}\left(\frac{D^2}{\lambda}\right), \left(\frac{D^2}{\lambda}\right), 2\left(\frac{D^2}{\lambda}\right), \infty,$$

where $D=2a$. The corresponding values for γ are:

$$\gamma=2\pi, \frac{3\pi}{2}, \pi, \frac{\pi}{2}, \frac{\pi}{4}, 0.$$

It should be noted that the case $r=\infty$ or $\gamma=0$ is the conventional far field result.

For the convenience of comparison, the field distribution curves are normalized in the following way: Let

$$E(r,0)=A_0 e^{j2\pi\phi_0} \tag{31}$$

then the normalized $E(r,\theta)$ for a fixed r is given by

$$\frac{E(r,\theta)}{E(r,0)}=\frac{A}{A_0}e^{j2\pi(\phi-\phi_0)}=A_n e^{j2\pi\phi_n}. \tag{32}$$

The normalized amplitude and phase distributions along the arcs are given in figure 5 to figure 14.

(ii) Field distributions along the aperture-axis:

In this and the following case, the distributions are not normalized but are plotted with the factor e^{-jkr} excluded. The two distribution curves, amplitude and phase, in the present case are useful in correlating the normalized distributions given in case (i).

(iii) Field distributions along a line parallel to the aperture-axis and at a distance equal to the radius of the aperture:

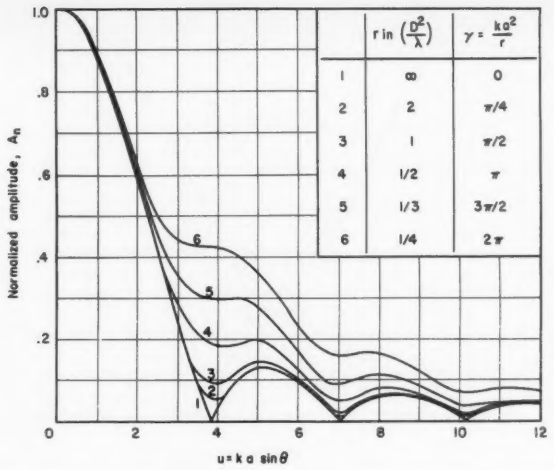

FIGURE 5. *Normalized amplitude distribution curves with aperture illumination* $=(1-\zeta^2)^0$, *(constant).*

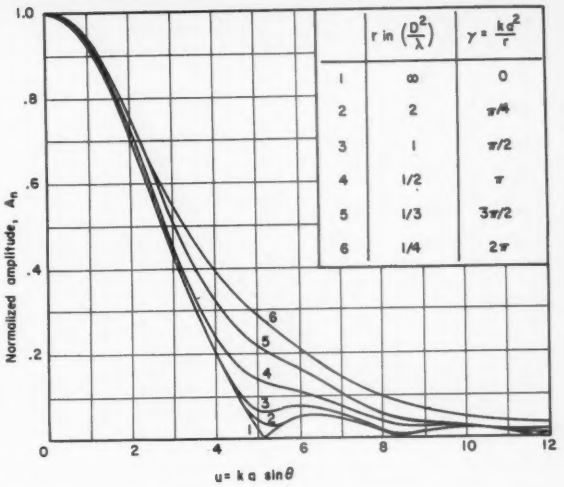

FIGURE 7. *Normalized amplitude distribution curves with aperture illumination* $=(1-\zeta^2)$.

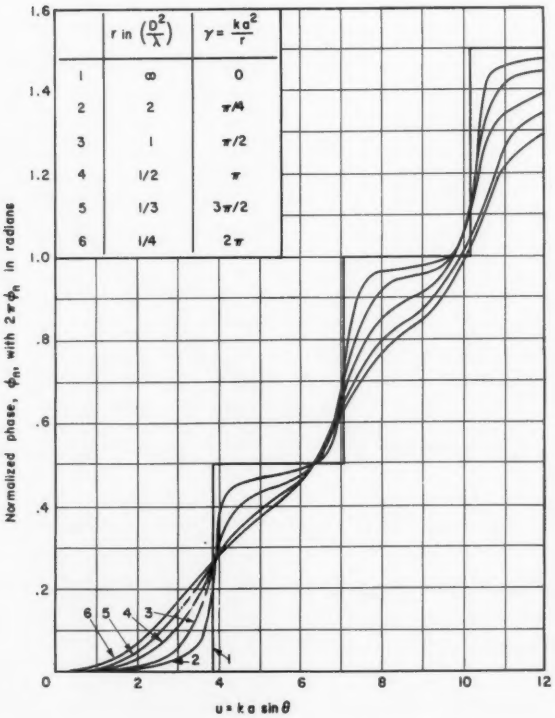

FIGURE 6. *Normalized phase distribution curves with aperture illumination* $=(1-\zeta^2)^0$, *(constant).*

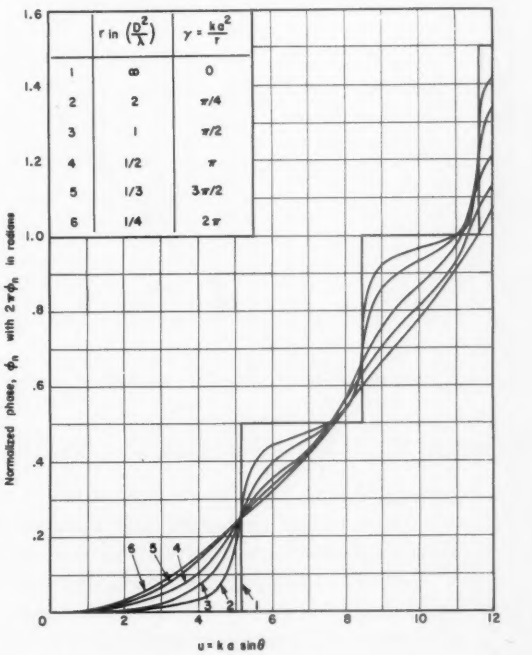

FIGURE 8. *Normalized phase distribution curves with aperture illumination* $=(1-\zeta^2)$.

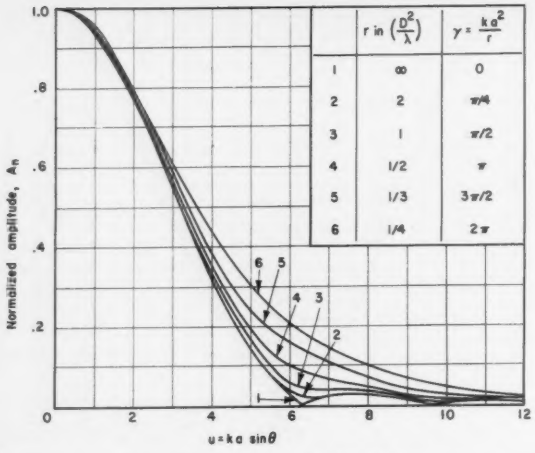

FIGURE 9. *Normalized amplitude distribution curves with aperture illumination* $=(1-\zeta^2)^2$.

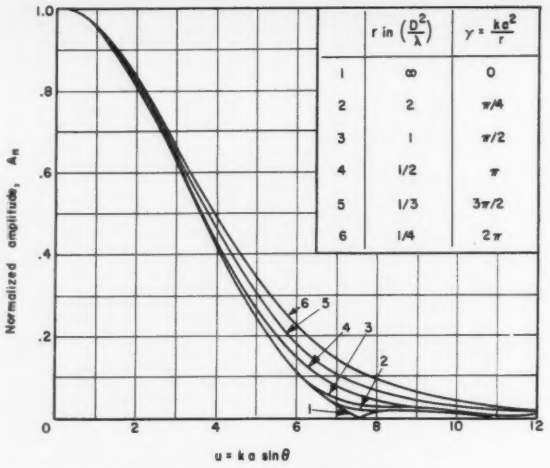

FIGURE 11. *Normalized amplitude distribution curves with aperture illumination* $=(1-\zeta^2)^3$.

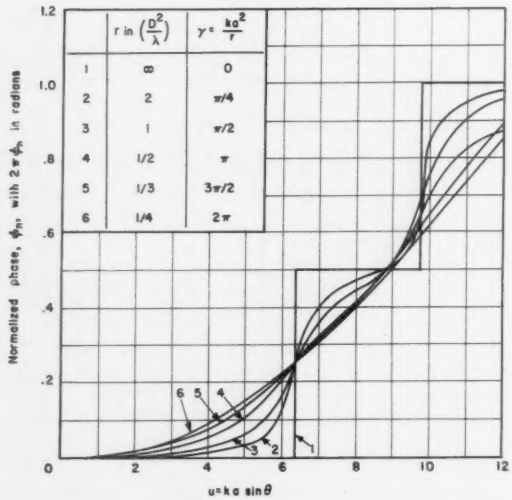

FIGURE 10. *Normalized phase distribution curves with aperture illumination* $=(1-\zeta^2)^2$.

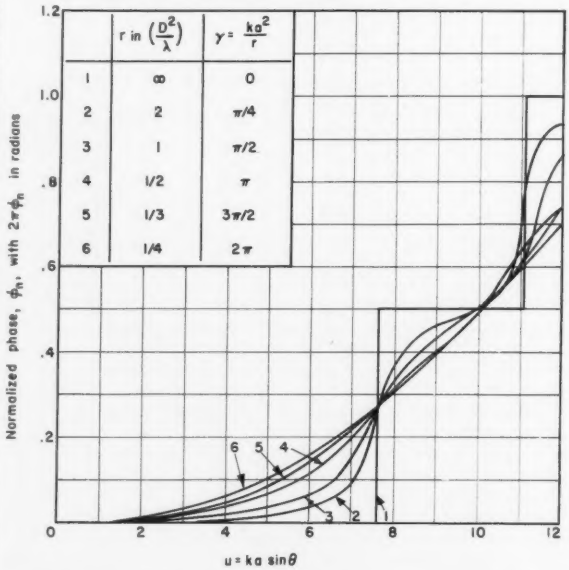

FIGURE 12. *Normalized phase distribution curves with aperture illumination* $=(1-\zeta^2)^3$.

Distribution curves for case (ii) and cases (iii) are given in figure 15 to figure 18. From these field distribution curves, the following properties are observed.

(1) For the normalized field distribution curves along circular arcs:

(a) For each aperture illumination of the form $(1-\zeta^2)^n$, the main beam width is essentially a constant in the range of r from $\frac{1}{8}(2D^2/\lambda)$ up to infinity. (Note: For a fixed direction, the parameter u is a constant.)

(b) There is no perceptible difference in the normalized amplitude distribution curves at $2D^2/\lambda$ (conventional far field limit) and at infinity for the same aperture illumination, except near those directions where the infinity case has zero values or nulls. On the other hand, there are differences between the phase distribution curves; these curves change from a stepped form at infinity to a smooth continuous form at $2D^2/\lambda$.

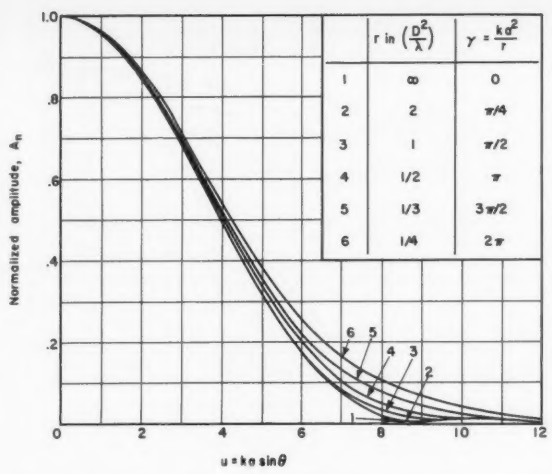

FIGURE 13. *Normalized amplitude distribution curves with aperture illumination* $=(1-\zeta^2)^4$.

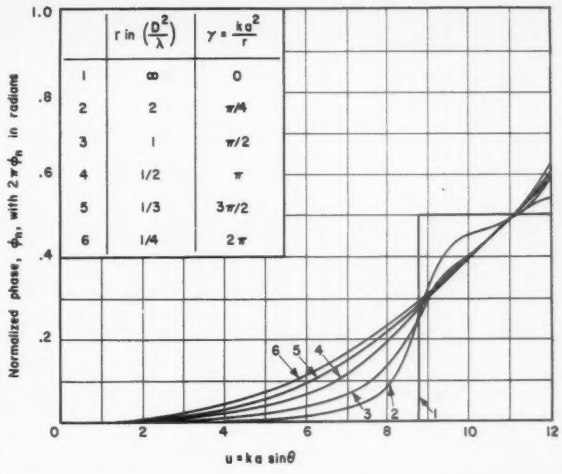

FIGURE 14. *Normalized phase distribution curves with aperture illumination* $=(1-\zeta^2)^4$.

(c) The "side lobe level" increases as the distance r is reduced, but the amplitude distribution curve as a whole becomes "smoother." It is also true that the phase distribution curve becomes smoother too as r is reduced.
(d) When the distribution curves of different aperture illuminations are compared, it is seen that the main lobe beamwidth increases as n is increased. At the same time, within a fixed measure of the angle θ, the number of side lobes is reduced.
(e) The side lobe level is definitely reduced as n is increased. The ratio of the normalized maximum amplitudes of the first side lobes with $n=4$ and $n=0$ is approximately 1 to 10.
(f) As n increases, the difference in the normalized amplitude distribution curves at different r becomes smaller.

(2) For the field distribution curves along the aperture-axis:
(a) Along the aperture-axis, the amplitude distributions vary closely as $1/r$ in the range $r=\frac{1}{2}(2D^2/\lambda)$ to $r=$infinity for all cases studied. As for the particular case $n=4$, this is true even when r is reduced to $\frac{1}{8}(2D^2/\lambda)$.
(b) Along the aperture-axis, all the phase distributions, excluding the exponential factor e^{-jkr}, are approximately straight lines, i.e., the phase varies linearly with respect to $1/r$.

(3) For the field distribution curves along a line parallel to the aperture-axis and at a distance equal to the radius of the aperture;
(a) In the range, $r=2D^2/\lambda$ to $r=$infinity, both the amplitude and phase distributions have approximately the same values as those obtained along the aperture-axis.
(b) At $r=\frac{1}{8}(2D^2/\lambda)$, the ratio of the corresponding amplitudes for the present case and case (ii) is roughly one to four for all cases computed.

6. Generalization to Nonuniform Aperture Illuminations of Other Forms

In the last section, only a special type of nonuniform illumination of the form $(1-\zeta^2)^n$ was given. It is possible to generalize the analysis to include nonuniform illuminations of other forms either through expansions by the Schmidt orthogonalization process [5] or by the following simple algebraic procedure. For any circularly symmetric aperture illumination, it is always possible to approximate it by an even polynomial of the variable ζ. Such poly-

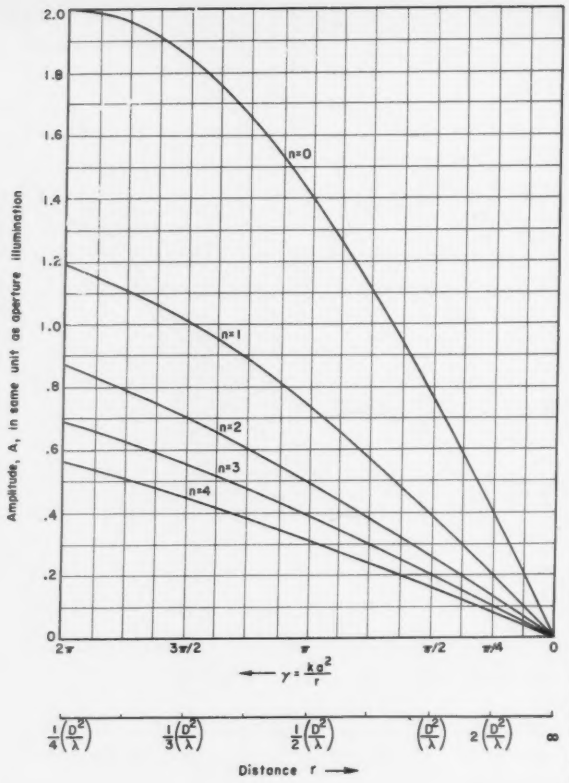

FIGURE 15. *Amplitude distribution curves along the aperture axis with aperture illumination* $=(1-\zeta^2)^n$.

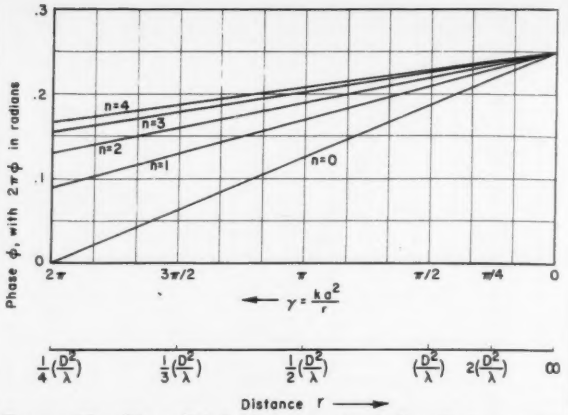

FIGURE 16. *Phase distribution curves (excluding the factor* e^{-ikr}*) along the aperture axis with aperture illumination* $=(1-\zeta^2)^n$.

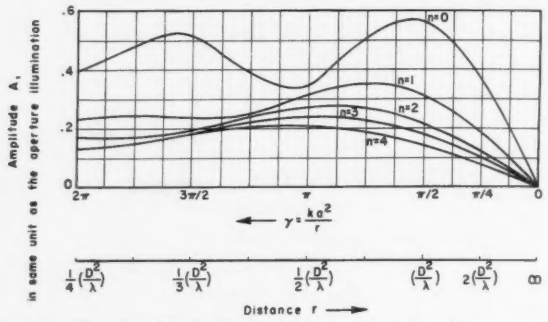

FIGURE 17. *Amplitude distribution curves along a line parallel to the aperture axis and at a distance a from the aperture axis with aperture illumination* $=(1-\zeta^2)^n$.

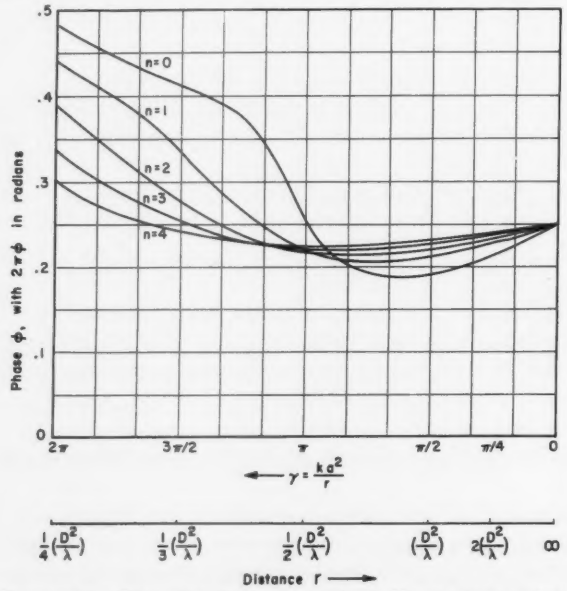

FIGURE 18. *Phase distribution curves (excluding the factor* e^{-ikr}*) along a line parallel to and at a distance a from the aperture axis with aperture illumination* $=(1-\zeta^2)^n$.

nomials are of the following form:

$$a_n\zeta^{2n}+a_{n-1}\zeta^{2(n-1)}+\ .\ .\ .\ +a_1\zeta^2+a_0. \tag{33}$$

It is clear that such a polynomial can always be transformed into the following form:

$$b_n(1-\zeta^2)^n+b_{n-1}(1-\zeta^2)^{n-1}+\ .\ .\ .\ +b_1(1-\zeta^2)+b_0. \tag{34}$$

For a given set of a's, the corresponding b's can be uniquely determined by solving a system of linear simultaneous algebraic equations. In particular, for the case of $n=4$, the coefficients b's obtained in terms of the a's are as follows:

$$\begin{aligned} b_4&=a_4\\ b_3&=-a_3-4a_4\\ b_2&=a_2+3a_3+6a_4\\ b_1&=-a_1-2a_2-3a_3-4a_4\\ b_0&=a_0+a_1+a_2+a_3+a_4. \end{aligned} \tag{35}$$

When $b_0, b_1, \ .\ .\ .\ , b_4$ are determined as above, the field expression is then given by

$$E(r,\theta)=e^{-jkr}\left(\gamma e^{j\frac{\pi-\gamma}{2}}\right)\int_0^1\sum_{n=0}^{4}b_n(1-\zeta^2)^n\,J_0(u\zeta)e^{j\frac{\gamma}{2}(1-\zeta^2)}\zeta d\zeta \tag{36}$$

In terms of $W_0^n(\lambda,u)$, (36) gives

$$E(r,\theta)=e^{-jkr}\left(\gamma e^{j\frac{\pi-\gamma}{2}}\right)\sum_{n=0}^{4}b_nW_0^n(\gamma,u) \tag{37}$$

Equation (37) can then be evaluated by using the results already obtained in this paper.

7. References

[1] M. K. Hu, Study of near-zone fields of large aperture antennas, Syracuse Univ. Research Inst., Syracuse, New York, final rept., pt. 2 (Apr. 1957).

[2] M. K. Hu, Fresnel region field distribution of circular aperture antennas, IRE Trans. on Antennas and Propagation, **AP–8,** No. 3, pp. 344–346 (May 1960).

[3] Hansen and Bailin, A new method of near field analysis, IRE Trans. on Antennas and Propagation **AP–7,** special suppl., pp. S458–S467 (Dec. 1960).

[4] R. C. Spencer, Paraboloid diffraction patterns from the standpoint of physical optics, MIT, Radiation Lab. RL Rept. T–7 (Oct. 1942).

[5] C. T. A. Johnk, Synthesis of aperture antennas, Univ., Ill., Eng. Exptl. Sta., Tech. Rept. 1 (1954).

[6] A. Ishimaru and G. Held, Analysis and synthesis of radiation patterns from circular apertures, Can. J. Phys. **38,** pp. 78–99 (Jan. 1960).

[7] T. T. Taylor, Design of circular apertures for narrow beamwidth and low sidelobes, IRE Trans. on Antenna and Propagation **8,** No. 1, pp. 17–22 (Jan. 1960).

[8] S. Silver, Microwave antenna theory and design (McGraw-Hill Book Co., Inc., New York, N.Y., Radiation Lab. Ser **12,** pp. 170–173, 1949).

[9] G. N. Watson, A treatise on the theory of Bessel functions (Cambridge Univ. Press, second ed., pp. 537–540, 1952).

(Paper 65D2–111)

JOURNAL OF RESEARCH of the National Bureau of Standards—D. Radio Propagation
Vol. 65D, No. 2, March–April 1961

Free-Balloon Borne Meteorological Refractometer[1]

John F. Theisen and Earl E. Gossard

(July 14, 1960; revised August 15, 1960)

In this paper a free balloon borne refractometer is described and samples of soundings are shown. The instrument has been used for sampling the refractive index through the troposphere in a study of the fine structure of refractive layers over Southern California. It uses fast response temperature and humidity elements and is carried aloft by a standard radiosonde balloon. The instrument avoids the defects of the usual radiosonde for obtaining refractive index information while allowing a nearly vertical sounding to be obtained without the disturbance of the atmosphere characteristic of a sounding taken by an aircraft.

1. Introduction

The vertical distribution of refractive index is of primary importance in a study of radio-wave propagation in the lower atmosphere. We have devised a system to obtain a direct and continuous measurement of refractive index by using slightly modified 400 Mc/s radiosonde components and techniques. The system was designed as a research tool to supplement information obtained from an aircraft borne microwave refractometer in an investigation of the intense super-refractive layers commonly found near the surface off the Southern California coast. There are certain well-known disadvantages to aircraft aside from expense and the necessity of maintaining air and ground crews. An aircraft being a large fast-moving vehicle disturbs the medium by an amount which is difficult to assess. Also, aircraft must necessarily pass rapidly through a very large horizontal distance in order to pass slowly through a small vertical distance. Thus fairly weak horizontal gradients may be erroneously interpreted as strong vertical gradients. These factors were important in the studies carried out at the Navy Electronics Laboratory because we were primarily interested in the possible existence of persistent microlayers of very large gradient which have sometimes been suggested to explain tropospheric radio scattered fields. For this purpose we needed essentially vertical profiles by fast response sensors providing a continuous record.

2. Refractive Index Equation

Because of the availability and dependability of radiosonde components a system employing wet and dry bulb sensing elements was used in otherwise unmodified radiosonde transmitters. The following approach was used in developing an expression for refractive index in terms of wet and dry bulb temperature.

Equation (1) relates radio refractive index to pressure, temperature, and humidity

$$N=(n-1)\times 10^6=\frac{77.6P}{T}+3.73\times 10^5\,\frac{e}{T^2} \qquad (1)$$

n is refractive index, T is temperature in (° K), P is atmospheric pressure in millibars and e is vapor pressure in millibars.

If we neglect the effect of pressure variation with height and define a modified refractive index, N_1, the curve of N_1 with height will be similar to N except that it will not have as great a negative slope. Its departure from N can be considered to be approximately linear as in the case of M and B, two other well-known modified refractive indices. This departure is 8.5 units per 1,000 ft. N_1 is now a function of only temperature and humidity and is given by eq (2) where P has been arbitrarily chosen as 1,000 millibars (mb).

$$N_1=\frac{77{,}600}{T}+3.73\times 10^5\,\frac{e}{T^2}. \qquad (2)$$

In examining the relationship between changes in temperature and humidity and changes in refractive index, we consider the partial derivatives of N with respect to T and e in the differential form of (2). We have

$$dN_1=\frac{\partial N_1}{\partial T}dT+\frac{\partial N_1}{\partial e}de \qquad (3)$$

where

$$de=\frac{\partial e}{\partial T_w}dT_w+\frac{\partial e}{\partial T}dT$$

e is assumed to be given by the psychrometric formula,

$$e=e_w-0.000675P\,(T-T_w) \qquad (4)$$

where e_w is the saturation vapor pressure at the

[1] Contribution from U.S. Navy Electronics Laboratory, San Diego, Calif.

wet-bulb temperature T_w. From Clapyron's equation

$$\frac{\partial e_w}{\partial T_w}=\frac{5418}{T_w^2}e_w \tag{5}$$

So finally:

$$dN_1=-\left[\frac{7.76\times10^4}{T^2}+\frac{7.46\times10^5 e}{T^3}+\frac{2.52\times10^2}{T^2}P\right]dT$$
$$+\left[\frac{3.73\times10^5}{T^2}\left(\frac{5418\,e_w}{T_w^2}+0.000675\,P\right)\right]dT_w. \tag{6}$$

Defining

$$A=\frac{3.73\times10^5}{T^2}\left(0.782+2.00\frac{e}{T}+0.675\Delta P\right) \tag{7}$$

$$B=\frac{3.73\times10^5}{T^2}\left(0.574+5418\frac{e_w}{T_w^2}+0.675\Delta P\right). \tag{8}$$

We can write changes in refractive index N_1 as

$$\Delta N_1=-A\Delta T+B\Delta T_w \tag{9}$$

where the coefficients A and B are slowly varying. ΔP represents the effect of atmospheric pressure on vapor pressure and has been chosen as the departure from 850 mb. Therefore $\Delta P=P-850$.

Although the coefficients are slowly varying, well behaved and single valued in the range of interest, they are functions of two and three variables. A complete and fully automatic analog solution of the equation would therefore require a fairly sophisticated computer. Since the instrument in its present form was designed for research purposes, it was more practical to use a simple computer and require the operator at the receivers to make occasional adjustments of the coefficients at the computer according to the ambient temperature, wet-bulb temperature and height of the balloon. This is easy in the present system since both temperature and wet-bulb temperature are available and may be recorded separately if desired. B usually has to be adjusted about once every 2 min in the first 10,000 ft msl and A about once every 5 min to ensure that errors are less than 3 percent. The accuracy can be made almost as great as desired by adjusting the coefficients more often.

For field use the computing operation should be fully automatic. For this condition it may be convenient to rewrite eq (9) as

$$\frac{1}{A}\Delta N_1=-\Delta T+\frac{B}{A}\Delta T_w. \tag{10}$$

In the ratio B/A the effects of pressure and temperature are much reduced and the coefficient on the right hand side of (10) can be considered to be a function of T_w only with an error of less than 4 percent through the temperature range from 0 to 25 °C. The error will actually be much less in general because of the fact that temperature and pressure usually decrease together with altitude and the overall error through the sounding is negligible for operational purposes. If a simple analog computer were designed to fit the B/A function, no adjustments of coefficients would have to be made during the sounding when eq (10) is used. However, a scale factor $1/A$ which depends weakly on temperature, wet-bulb temperature and pressure has been introduced on the left-hand side of the equation. $1/A$ is a sensitivity factor which can range from about 0.235 to 0.280, although the actual range over the sounding will generally be much less because temperature and pressure usually decrease together. Since the only variable coefficient is now a scale factor, the minor adjustments of the refractive index scale through the sounding can be made on the recorder record after the sounding is completed by using the known temperature, wet-bulb temperature and altitude at critical points in the sounding.

3. Refractometer System

A standard radiosonde system uses a thermistor to obtain temperature and a lithum-chloride strip to obtain humidity. By using a switching mechanism mechanically coupled to an aneroid cell, the meteorological sensing elements along with reference resistors are switched in and out of the measuring circuit—a grid-blocking oscillator. The oscillator frequency depends on the resistance in the circuit. Reference resistors provide altitude and calibration information.

The inaccuracy and long time constant (anywhere from 5 to 35 sec depending on temperature) of the lithium chloride strip make it unacceptable in the present application because *gradients* of refractive index rather than absolute values of refractive index are the important factor in most radio meteorological applications. Because of the slow response and discontinuous method of transmission of information the conventional radiosonde grossly underestimates sharp refractive index gradients and small fluctuations are usually undetectable. A system was therefore developed which has the advantages of a conventional radiosonde, namely, the expendability of the measuring units, the near vertical sounding possibilities and an ascension rate of 500 to 1,000 ft/min but which provides a *continuous* record of refractive index and has a sufficiently *fast response* to detect microlayers and strong gradients. First considerations were given to a system using one radiosonde transmitter carrying two thermistors, one for wet-bulb and one for dry-bulb temperature. Along with appropriate circuit modifications to enter a pressure dependence term from the radiosonde baroswitch a system could be developed that transmitted refractive index directly from the single transmitter [1].[2] However, since our main interest was to have a system which required little or no

[2] Figures in brackets indicate the literature references at the end of this paper.

modification to presently existing equipment, we decided on a dual transmitter-receiver setup. This permitted use of standard transmitters and receptors. Also, previously developed test, calibration and operating procedures could be followed. In this system separate signals are telemetered to the ground by conventional radiosonde transmitters. A simple analog computer on the ground converts the temperature and humidity information to refractive index which is then recorded as a continuous function of altitude. Reference altitudes are obtained by interrupting the otherwise continuous trace at the high reference contacts of the baroswitch unit. The pressure altitude thus obtained is sufficiently accurate for radio-meteorological requirements and compares favorably with altitudes obtained from aircraft altimeters. A block diagram of the entire refractometer system is shown in figure 1 and a detailed block diagram of the computer is shown in figure 2. Figure 3 shows the balloon-borne components of the system. Figure 4 shows the receivers, computer and recorder. The recorder was a continuously recording potentiometer type, made by Varian and the operational amplifier was a plug-in type made by Philbrick.

A wet-bulb measuring device was substituted for the lithium-chloride strip. It was a thermistor identical to the temperature element but provided with a fine cotton wick and a reservoir of distilled water. The water was fed to the element by capillary action and ventilation was provided by the vertical motion of the entire unit. A ventilation rate of 100 ft/min was required to maintain a reliable wet-bulb measurement. The time constant of this type of wet-bulb was 2½ sec and essentially inde-

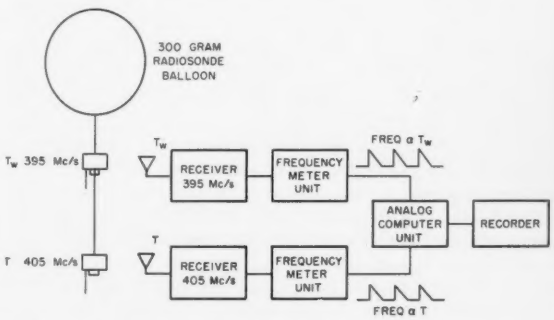

FIGURE 1. *Block diagram of balloon-borne meteorological refractometer system.*

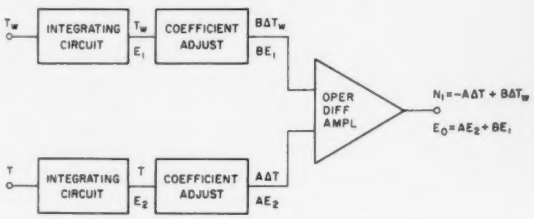

FIGURE 2. *Block diagram of computer.*

FIGURE 3. *Photograph of the airborne components.*

FIGURE 4. *Photograph of the receivers, computer, and recorder.*

pendent of ambient temperature. The wet-bulb freezes when the air temperature is between —4 and —8 °C. The freezing is very aburpt as seen in the sample soundings shown in figure 6. After the latent heat released has been dissipated the record quickly returns to normal. Since this system was primarily intended for use at temperatures above 0 °C, no further consideration has so far been given to the characteristics of the frozen wet bulb. Over the ocean areas of the world the great majority of superrefractive layers occur in the lowest 10,000 ft of the atmosphere [2] and the record after the wet bulb froze was of little interest in the research program for which the refractometer system was designed. In principle it should be entirely possible to make simple adjustments of the computer when the wet-bulb freezing level is reached and continue the sounding to higher elevations using the ice-bulb temperature as a measure of humidity. Tentative investigation indicates that this procedure is practical, but experimental study of the time required for the ice to sublime off of the wet bulb is needed.

Many years of use at the Navy Electronics Laboratory have proven the accuracy and reliability of carefully wrapped thermistors as wet-bulb temperature sensing elements. They have been used in captive balloon measurements [3, 4] and in wet-thermistor rod aerographs. A refractive index variometer using a wet-bulb, dry-bulb approach consisting of fast response thermistor beads has been developed in Japan [5] and has been used for measurements to 1,500 ft. Figure 5 shows profiles of refractive index taken simultaneously with a microwave refractometer and with an aerograph in an SNB–5 aircraft. Because of the low speed of this aircraft, frictional and compressional heating of the thermistor elements is not serious and it is seen that the agreement of the two measuring systems is excellent even though the aerograph was only read at 500-ft intervals.

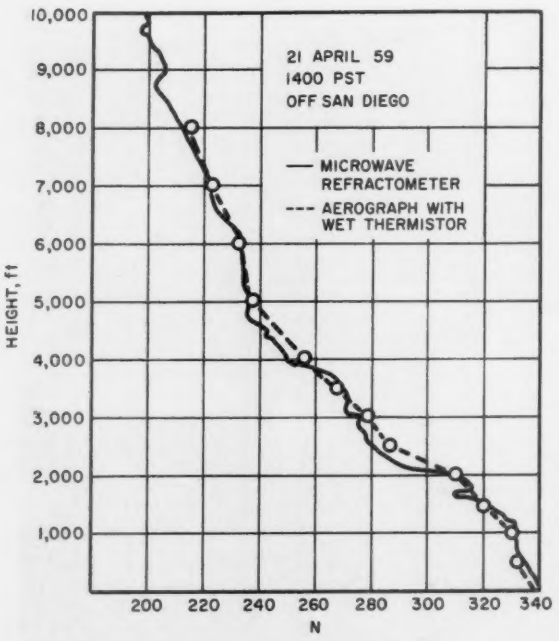

FIGURE 5. *Simultaneous microwave refractometer (solid curve) and wet-thermistor aerograph soundings taken by an aircraft.*

Aerograph temperature and wet-bulb temperature were read every 500 ft and refractive index was then computed by hand.

4. Discussion of the Sounding Data

Several of the soundings were compared with the refractive index profiles computed from radiosonde data. Figure 6 shows sample refractive index soundings. The afternoon sounding of 11 March was followed immediately by a conventional radiosonde ascent. The radiosonde record was analyzed exactly as it would normally be analyzed in a weather station and the resulting profile is shown by the straight line segment sounding in figure 7. It is seen that several strong gradients and many small features are missed entirely by the radiosonde.

Figure 8 shows a refractive index profile in which a very abrupt change in refractive index occurs. At 600 ft msl the refractive index changed 20 N units in 150 ft or 133 units per 1,000 ft. However the local San Diego radiosonde observation indicated a change of 25 N units in 500 ft or only 50 units per 1,000 ft. For many thin layers the error in gradient has been found to be even larger.

Persistence of the atmospheric fine structure is of special interest both in tropospheric scatter propagation studies and in radar coverage prediction. The release times on 11 March (fig. 6) were 3 hr apart. The overall similarity of the profiles is striking, and even some of the fine structure of the first sounding is repeated in the second.

One very important advantage of a balloon sounding over an aircraft sounding is its nearly vertical ascent relative to the air stream. For example it has been noticed for several years by many observers that a thin but prominent minimum in refractive index often occurs in the lower part of strong super refractive layers recorded by microwave refractometers in aircraft. It has been the generally accepted belief that this minimum was caused by the horizontal component of the aircraft's flight path as it passed through a wavy structure entering the layer. The situation is shown schematically in figure 9. The balloon-borne system definitely establishes the fact that this interpretation is *not* correct because the prominent minimum often appears in the balloon soundings also. Furthermore the balloon soundings establish the fact that the small refractive index minimum is due principally to the humidity distribution. A vertical sounding by balloon thus eliminates ambiguities arising from the horizontal component of the flight path of an aircraft.

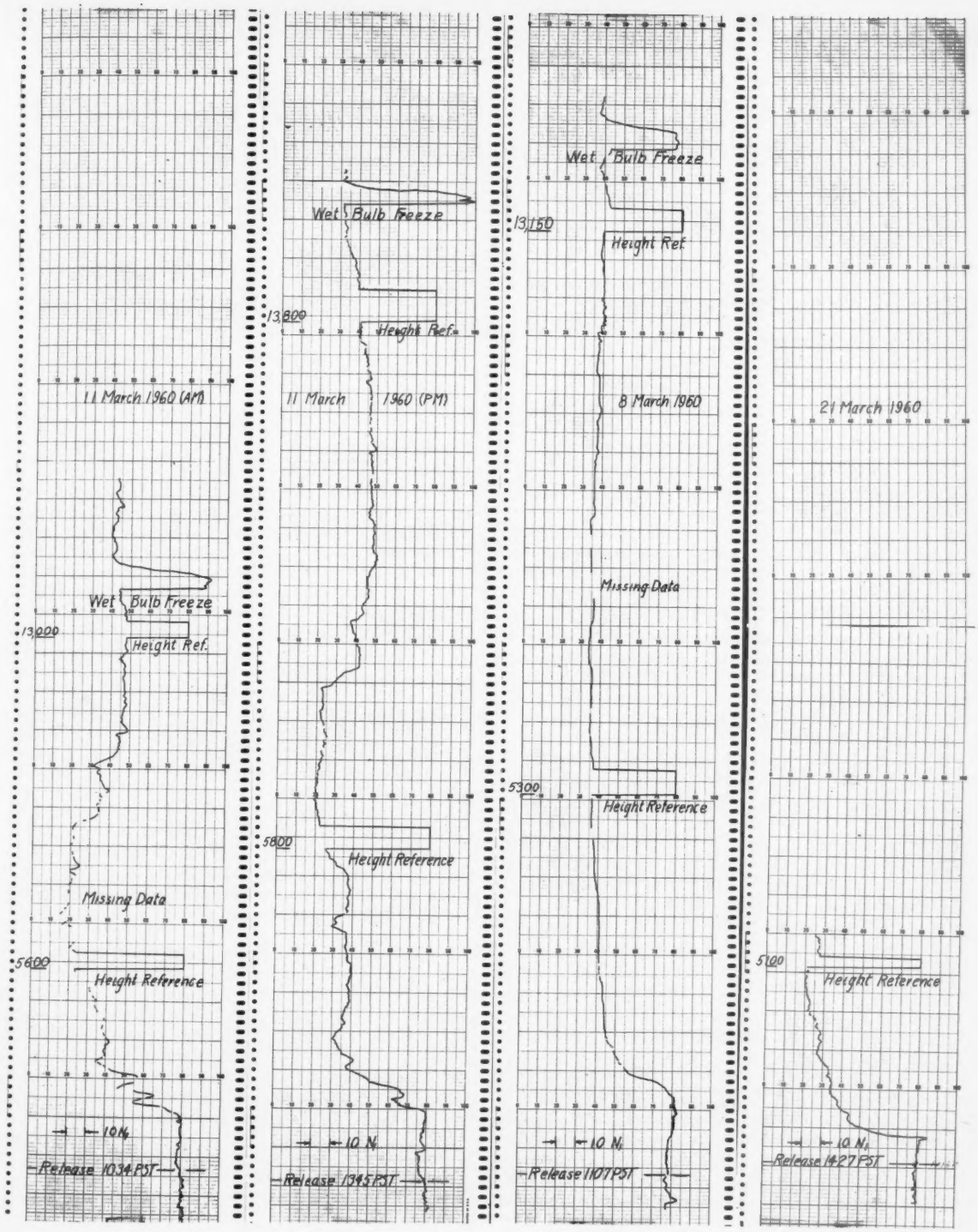

FIGURE 6. *Sample records.*

The missing data on the morning of 11 March occurred when the balloon came directly over the receivers and passed through the null of the receiving antennas.

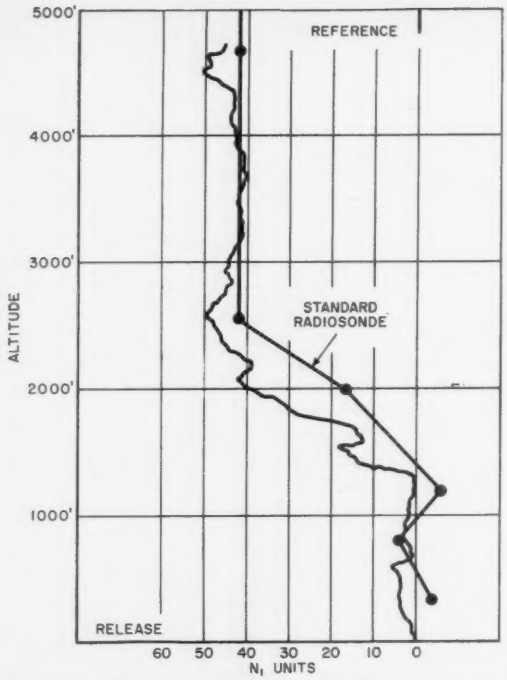

FIGURE 7. *Afternoon sounding for 11 March 1960 and a standard radiosonde sounding taken immediately after the refractometer sounding (about one hour later).*

The refractive index was computed by hand from the radiosonde data and is plotted in linear segments between computed points.

5. Conclusions

A meteorological refractometer system which is expendable and light enough to be flown on a radiosonde balloon can be built from standard radiosonde components. The system has proven to be very useful as a research tool for studying the microstructure of the atmosphere up to 13,000 ft msl. Since the great majority of super refractive layers occur well below this height it should also prove to be a useful operational tool—especially in fleet units from which aircraft cannot be operated, and for problems in surface-to-air radar coverage where only the low troposphere is important.

6. References

[1] A. H. Clinger and A. W. Straiton, Adaptation of the radiosonde for direct measurement of radio refractive index, Bull. Am. Meteorol. Soc. **41,** 250 (1960).

[2] J. Michealis and E. E. Gossard, Distribution of refractive layers over the North Pacific and Arctic, NEL Report 841 (1958).

[3] A. L. Crozier, Captive balloon refractovariometer, Rev. Sci. Instr. **29,** 276 (1958).

[4] E. E. Gossard, Power spectra of temperature, humidity and refractive index from aircraft and tethered balloon measurements, IRE Trans. **AP-8,** 28 (1960).

[5] K. Hirao and K. Akita, A new type refractive index variometer, J. Radio Research Labs. (Japan) **4,** (1957).

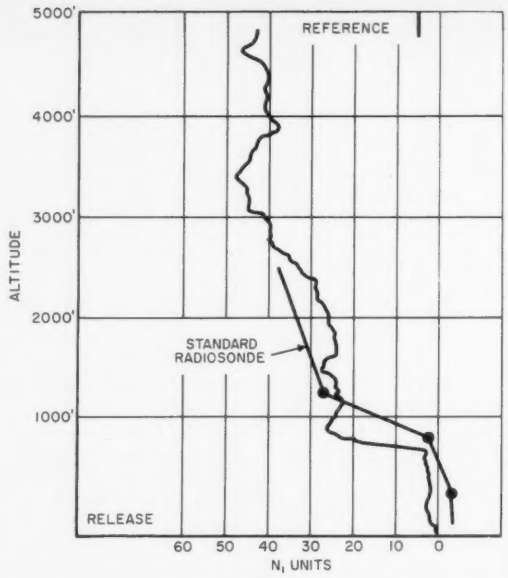

FIGURE 8. *Refractometer sounding for 10 March 1960 and corresponding radiosonde data taken from the local San Diego raob.*

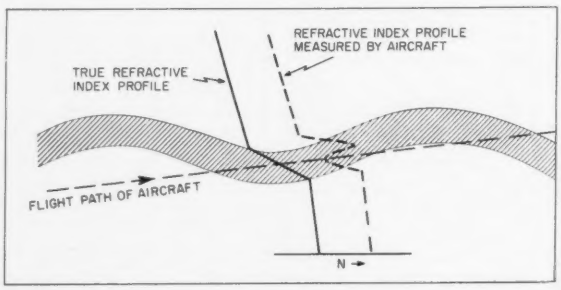

FIGURE 9. *Schematic description of how an aircraft sounding can indicate an erroneous anomaly in the height distribution of refractive index.*

(65D2–112)

JOURNAL OF RESEARCH of the National Bureau of Standards—D. Radio Propagation
Vol. 65D, No. 2, March–April 1961

Weather and Reception Level on a Troposphere Link—Annual and Short-term Correlations[1]

L. G. Abraham, Jr., and J. A. Bradshaw

(August 8, 1960; revised September 30, 1960)

The weather parameters suggested by the Booker-Gordon theory are correlated with data from a troposphere link not previously reported. While the correlations over the whole year's weather cycle are high, the short term correlations practically vanish. The former without the latter lend little support to this theory.

This article reports a study of relations between weather variables and hourly median signal levels at 915 mc, received over a 134 mile tropospheric link operated under sponsorship of AFCRC[2] in 1956–57, and offers a comment on similar studies reported by others. In the present study, one of the authors collected 160 entries of signal strength over hours corresponding to the hours for collecting weather data at the Albany, Boston Harbor, Nantucket, and Portland, Me., weather stations. (The first station lies on the link axis near the receiver, and the last three surround the transmitter at Bedford, Mass.)

The 160 entries were first correlated with weather parameters averaged for both ends of the link axis. Among these were the mixing ratio (MR), in grams of water vapor per kilogram of dry air at ground level, and the stability index (SI), involving the lapse rate of temperature between 5000′ and 10,000′. The MR is not affected by changes of pressure or temperature, short of precipitation, in a given air sample, and in this sense is conservative. The SI increases as the potential energy available for turbulent mixing increases. This SI is proportional to $\gamma - \gamma_d$ in the notation of [1].[3]

The pair correlations obtained with signal level in decibels, voltage and power respectively were MR: 0.58, 0.46, 0.29; and SI 0.22, 0.11, and 0.03. A regression calculation of signal against both weather variables (clearly not orthogonal) gives R=0.60, 0.51, 0.34. The high decibel correlations point to some extended-path mechanism; whereas if voltage or power had exceeded decibels in correlations with weather, the data would suggest the importance of single scatterers.

Next the same data were grouped into 10 periods (by month, but 4 summer months were combined in pairs) so that about 16 entries fell in each period. The normalized monthly average values and rms deviations appear in figure 1. One can see a high correlation between averages; indeed, we have 0.93 for signal in decibels and MR, 0.69 for signal and SI. Within these periods, however, the correlations were much lower: the average correlation was 0.13 ± 0.27 rms deviations for signal in decibel and MR, and 0.06 ± 0.20 for signal and SI. Figure 2 shows these correlations within months.

Clearly the signal and these weather parameters have in common a marked annual cycle of variation but practically no short-term relationship. The literature gives examples of this too, for the same appears in the 0.90 correlation of refractive index with monthly medians in [2]. In references [3] and [4], data were collected over 3 to 6 months, so the annual cycle is doubtless represented. Moreover, points associated with rapid changes in either variable were rejected before making a correlation. This selection, although justified on physical grounds, is dangerous in a statistical sense, and it reduced the number of points considered to 31 and 20 respectively. The results were correlations of 0.85 between signal level and a variable combining refractive index and static stability in [3], and 0.80 for differential signal level and Richardson's stability number in [4]. The annual cycle is apparent in correlations reported earlier [5, 6, 7, 8, and 9]. Several of these reports also mention poor correlation of chosen variables with short term (diurnal) signal levels.

The Booker-Gordon theory of tropospheric propagation by "blob scatter" [10] leads one to expect more short-term correlation. Without it, the annual cycle lends little support to this theory. There are, however, some reports of good correlation in small samples with large scale weather patterns, cyclones and anticyclones [9, 11, 12], in particular one by Pickard and Stetson [13] whose method of analysis by "epochs" deserves further employment in this field of study.

[1] Contribution from General Electric Research Laboratory, Schenectady, N.Y.
[2] Under Contract AF19(604)-1723.
[3] Figures in brackets indicate the literature references at the end of this paper.

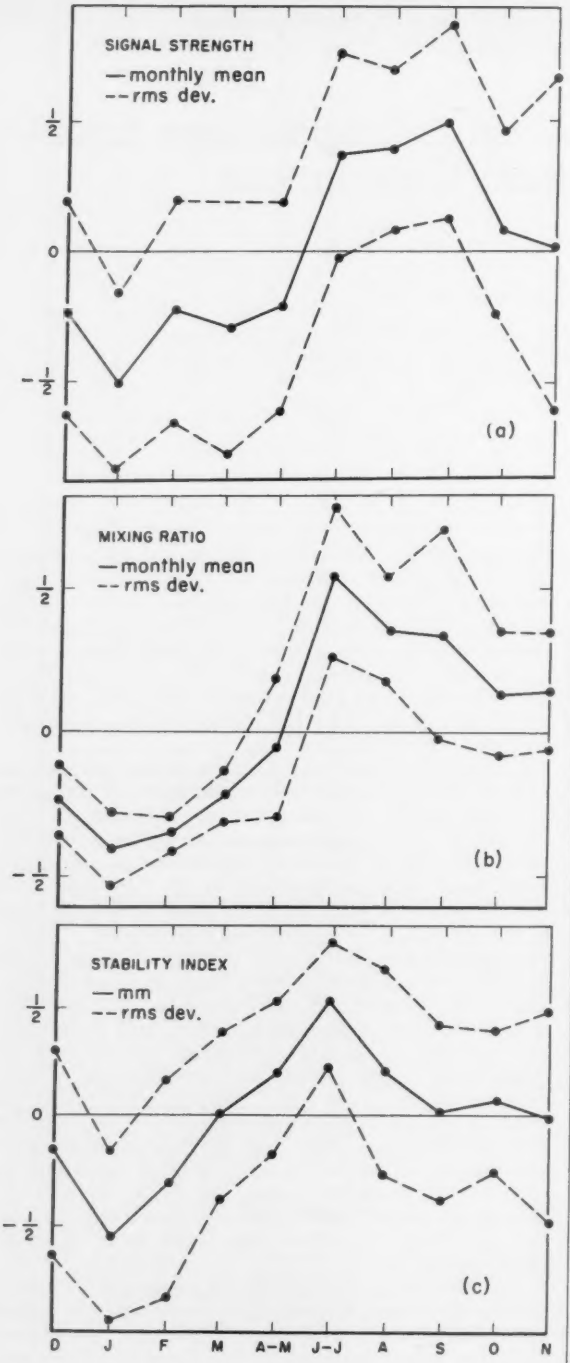

FIGURE 1. *Signal strength and two weather parameters, normalized monthly average values in 1956–57, and RMS deviations.*

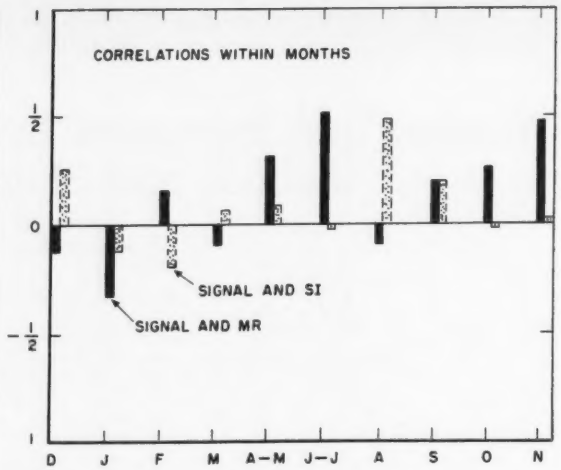

FIGURE 2. *Correlations within months between signal level and two weather parameters.*

References

[1] Norman Beers, Handbook of meteorology, 403 (McGraw-Hill Book Co., Inc., New York, N.Y., 1945).

[2] A. Crawford, D. Hogg, and W. Kummer, Studies in tropospheric propagation beyond the horizon, Bell System Tech. J. **38,** 1067, see fig. 14, p. 1088 (September 1959).

[3] P. Misme, The correlation between the electric field at a great distance and a new radio-meteorological parameter, Trans. IRE **AP–6,** 289 (July 1958).

[4] R. Bolgiano, Jr., A theory of wavelength dependence in ultra-high frequency transhorizon propagation, J. Research **NBS 64D,** 231, see fig. 6, p. 237 (May 1960).

[5] B. Bean and F. Meaney, Some applications of the monthly median refractivity gradient in tropospheric propagation, Proc. IRE **43,** 1419, see fig. 3, p. 1421 (October 1955).

[6] B. Bean, Some meteorological effects on scattered radio waves, Trans. IRE, **CS–4,** 32, see fig. 3, p. 34 (March 1956).

[7] R. Gray, The refractive index of the atmosphere as a factor in troposphere propagation far beyond the horizon, Conv. Rec. IRE, **5,** pt. I, 3, see figs. 2, 3, 7 and 9 (March 1957).

[8] K. Bullington, W. Inkster, and A. Durkee, Results of propagation tests at 505 mc and 4090 mc on beyond horizon paths, Proc. IRE **43,** 1306, see pp. 1315–16 (October 1955).

[9] Onoe, Hirai, Niwa, Results of experiment of long distance overland propagation of ultra-short waves, J. Radio Research Labs, Tokyo, Japan, **5,** 79, fig. 3, p. 84 (April 1958).

[10] H. Booker, and W. Gordon, Theory of radio scattering in the tropospheric, Proc. IRE, **38,** 401 (April 1950).

[11] G. C. Rider, Propagation measurements at 858 mc over paths up to 585 km, Marconi Rev., **131,** 185, see fig. 6, p. 189 (October 1958).

[12] W. Moler and D. Holden, Tropospheric scatter propaga- and atmospheric circulations, J. Research NBS **64D,** 81, see fig. 10, p. 89 (January 1960).

[13] G. Pickard and H. Stetson, A study of tropospheric reception at 42.8 mc and meteorological conditions, Proc. IRE **35,** 1445 (December 1947).

(Paper 65D2–113)

JOURNAL OF RESEARCH of the National Bureau of Standards—D. Radio Propagation
Vol. 65D, No. 2, March–April 1961

Initial Results of a New Technique for Investigating Sferic Activity [1,2]

G. Hefley, R. H. Doherty, and R. F. Linfield

(February 25, 1960; revised August 8, 1960)

A technique for the measurement of sferics on a massive scale has been developed. The technique pertains largely to spectral and directional measurements. Representative samples of data are presented and discussed. The data samples include:

1. Diurnal variations in sferic rates as a function of the 10.5, 40, and 100 kc/s component amplitudes.
2. Sferic rates as a function of triggering level.
3. Directional measurement of sferic rates.
4. Correlation of directional sferic rates with weather reports.
5. Sferic amplitude distributions at 10.5, 40, and 100 kc/s.
6. Comparison of the distribution of amplitudes of the sferics from two different storm areas.

Recommendations for future measurements are made.

1. Introduction

1.1. Background

A "sferic" [3] is the electromagnetic energy radiated from a lightning discharge and propagated between the earth and the ionosphere. The spectral components of this radiation are variable in both phase and amplitude depending on the nature of the discharge [1].[4] Electromagnetic energy is radiated at frequencies ranging from a few cycles per second up into the megacycle range [2, 3]. As the sferic is propagated its original form is modified as a result of propagation characteristics [3 to 7].

When sferic waveforms are observed on an oscilloscope the end result of all propagation factors is seen, but the analysis of these same factors is by no means self-evident [8]. Certain spectral components whose amplitude and phase cannot be resolved with broadband waveforms can be separated out and recorded at measurable levels through the use of properly designed restricted band techniques.

1.2. Instrumentation

Sferics were observed with a system devloped for the automatic measurement of the complex spectral characteristics and for the automatic high-speed processing of statistical data. These observations are potentially useful in many applications such as propagation studies, distance measurements, thunderstorm location and tracking, and ground conductivity determinations. In these applications, however, only a minute fraction of the total number of sferics is of interest or value. Therefore, in order to make practical use of the few desired sferics it is necessary to eliminate the undesired signals immediately to avoid a prohibitive waste of time in analyzing the data. Such a scheme permits data handling on a scale which is statistically meaningful. Analysis techniques which were previously impractical can be applied since manual data processing is substantially reduced.

The system performs the following functions: Azimuthal detection, complex spectrum measurement, data storage, data selection, and recording.

The azimuthal detection portion of the system has been designated E–Φ (Ephi) because the bearing of the transient signal is determined from the relative phase of the vertical electric field at spaced antennas (three antennas were used for these measurements). The system minimizes siting and polarization errors A directional code is generated upon reception of each signal. This code is ideally suited for subsequent logical operations.

Pulses are derived from the sferics in certain portions of the spectrum. These pulses are formed by band-pass filters of such characteristics that the pulses rise as rapidly as possible but still maintain a shape nearly independent of the characteristics of the sferic waveform. Information on the relative phase and amplitude of these spectral components is obtained by comparing filter outputs.

These intrinsic characteristics of the signals, along with data from Ephi are used to distinguish desired from undesired signals. The data selection is accomplished by logical "and" and "or" circuitry in

---

[1] Contribution from Central Radio Propagation Laboratory, National Bureau of Standards, Boulder, Colo.

[2] Portions of this paper were originally presented to the spring URSI meeting in Washington, D.C., May 1959, in two papers entitled: "Observations of Some Spectral Components of Sferics" by R. F. Linfield, and "Observed Time and Direction Variations of Sferic Activity" by R. H. Doherty.

[3] The authors feel that the use of sferic or sferics as defined above is more suitable than atmospheric or atmospherics because of the more general connotation of these latter terms. For example: Nagoya University's Research Institute of "Atmospherics" studies all electromagnetic phenomena of natural origin, and a National Institute for "Atmospheric" Research proposed for the United States would study all phases of the physics of the atmosphere.

[4] Figures in brackets indicate the literature references at the end of this paper.

accordance with a preset program. Data are stored while these logic circuits perform their respective functions. These circuits make the decision to record or disregard the data in about 500 μsec.

Special techniques which overcome some of the difficulties of recording and timing randomly occurring transient signals have been developed. Electronic counters are used to indicate summation of sferics selected with respect to certain parameters.

Oscilloscope photographs are taken not only of the broadband sferic waveform but also of the various pulses derived from the different portions of the spectrum. A high-speed intermittent-action camera was developed for this purpose and is so arranged that, if desired, pictures are taken only of sferics which have particular values of certain parameters. The time of arrival of the sferic is recorded on each photograph in digital form [9].

1.3. Data Interpretation

Sferic rates are most meaningful when they are related to a certain area. Sferic density is defined as sferics per second per square mile, and this type of information would be directly available from two directional systems recording and correlating sferics. The data that are presented in this paper were observed at only one point and, therefore, the azimuthal rates only indicate the direction of the activity. Weather reports were the only available independent data and, in general, it was difficult to determine whether the activity was concentrated or diffused within the sector.

In order to compare different sets of measurements the observed rates must be standardized with respect to time and the sector width. Sector rates are, therefore, expressed as the number of sferics per second per degree.

The data presented in this paper are in most cases relatively small samples and are intended primarily to illustrate some of the simpler types of measurements that might be made on a systematic long-term basis.

2. Omnidirectional Data

2.1. Diurnal Variations of Sferic Rates

In many cases it is convenient to describe sferic activity by the rate of occurrence with respect to one or more parameters. For example, the number of sferics per second which exceed a specified field strength or the number per second which come from a given direction with amplitudes[5] within specified limits.

Data contained in this paper, with one exception, were recorded in Gold Beach, Oreg., during the summer of 1958. One set of measurements was made in Boulder, Colo., in November 1958. A typical sample of the summer sferic activity recorded at Gold Beach is shown in figures 1, 2, and 3. Data from figures 1 and 3 are related in that the times of observation were essentially the same. Additional 10.5 kc/s data were obtained during July and August, but plots of the average of all 10.5 kc/s data were so similar to figure 1 that an additional figure of these data was not included. Therefore, figure 1 may be considered representative of summer sferic

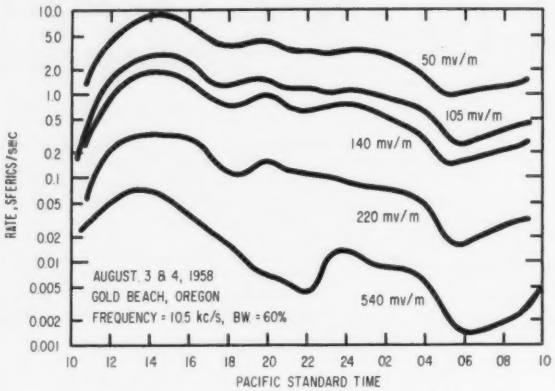

FIGURE 1. *Diurnal sferic rates, 10.5 kc/s.*

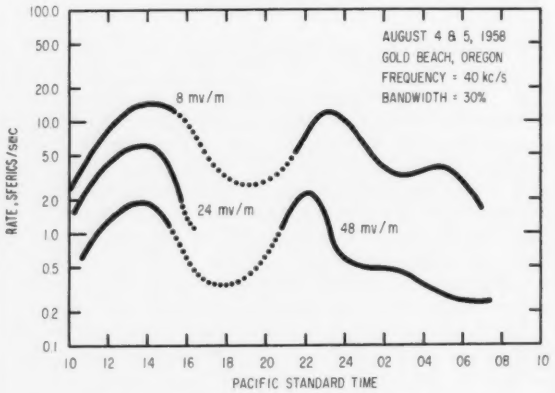

FIGURE 2. *Diurnal sferic rates, 40 kc/s.*

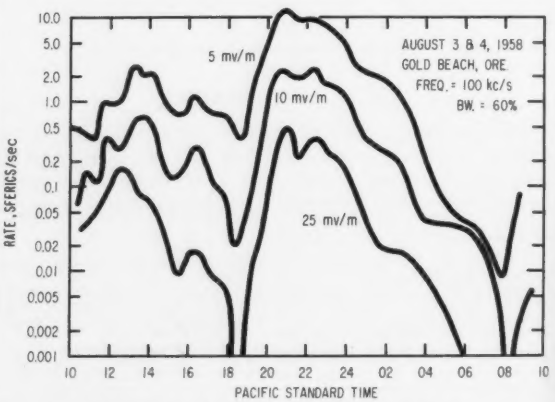

FIGURE 3. *Diurnal sferic rates, 100 kc/s.*

[5] In this paper all amplitudes or triggering levels presented in millivolts or volts per meter represent peak-to-peak values of an equivalent cw signal centered in the pass band of the filter.

rates recorded at Gold Beach. These data were obtained using band-pass filters with center frequencies of 10.5, 40, and 100 kc/s and bandwidths of 60, 30, 30 percent respectively. The amplitude of the 10.5 kc/s component is usually about one-half the amplitude of the broadband waveform and, therefore, the approximate broadband rates may be determined from figure 1. This ratio, however, varies somewhat from sferic to sferic depending on the spectral distribution of the energy [3].

Figure 1 also shows that the sferic activity was greatest in the early afternoon and least in the vicinity of sunrise. These times of day correspond to the usual daily cycle of thunderstorm activity. During the summer months a major part of the thunderstorms in continental United States occurs in the mountains and central part of the country. The peak occurring between 1200 and 1600 correlates well with sferic activity in the mountainous regious. The smaller peak at 2000 and the sustained activity throughout the night probably reflect the storms in the central plains and Gulf regions (see fig. 4). Since fewer sferics from a particular storm will exceed a given threshold level at the receiver as the distance to the storm is increased, it may be assumed that these measurements are weighted heavily by the relatively nearby thunderstorm activity in the mountains.

In comparing the 10.5 kc/s (fig. 1) and 100 kc/s (fig. 3) records, the early afternoon peaks correspond rather closely but, in contrast, the 100 kc/s record shows a minimum at sunset and a large peak around 2100 hr. Part of the data from figures 1 and 3 are replotted in figure 5 to show the nighttime peak more clearly. The daytime minimum and the rapid increase shortly after sunset is evidently the result of an ionospheric effect at sunset and the subsequently enhanced ionospheric propagation thereafter. The peak at 2100 correlates with the activity in the plains region as shown in figure 4, but the comparison of the rates at 10 and 100 kc/s after 2100 is not understood.

Although part of the data are lacking for the 40-kc/s curves (fig. 2), the trends shown are not inconsistent with what might be expected at such an an intermediate frequency.

2.2. Variations in Sferic Rates

When the sferic rates were considered as a function of receiver sensitivity or triggering level, a nonlinear distribution was observed. Some examples are shown in figure 6. In these cases samples of data were obtained during brief periods of time so it could be assumed that the sferic activity remained essentially constant during an individual measurement period. Since the distributions are different, it seems obvious that the sferic activity had changed significantly between sets of measurements.

A number of samples of rate versus triggering level data, averaged over 4-hour periods, are shown in figure 7. The scattering of the points is a result of the mixture of diurnal and day-to-day variations in sferic activity. A smooth curve drawn through the mean of the points is seen to have an average slope of about -2.

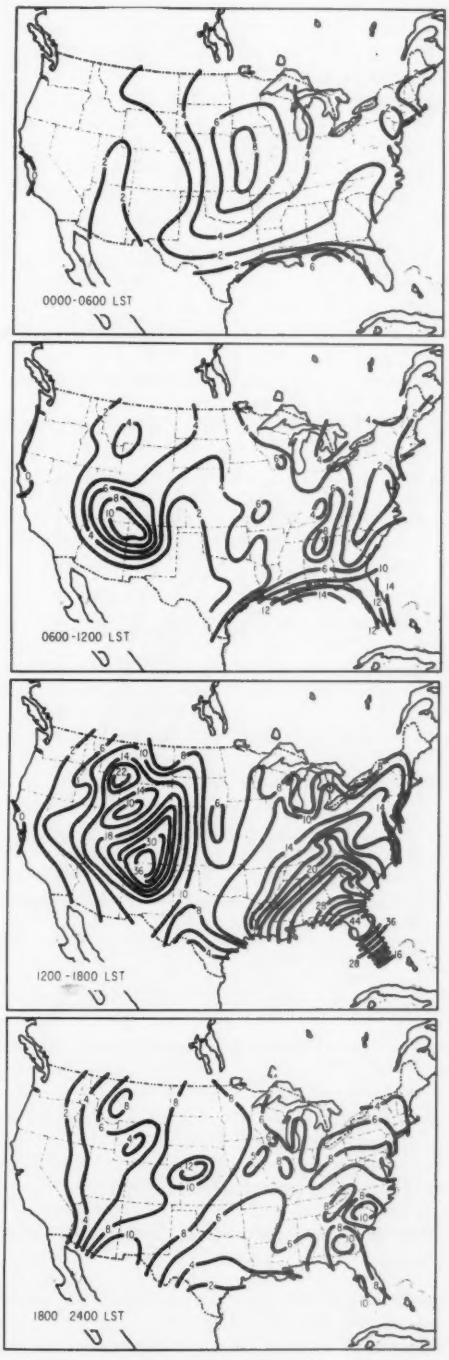

FIGURE 4. *Diurnal thunderstorm counts.*

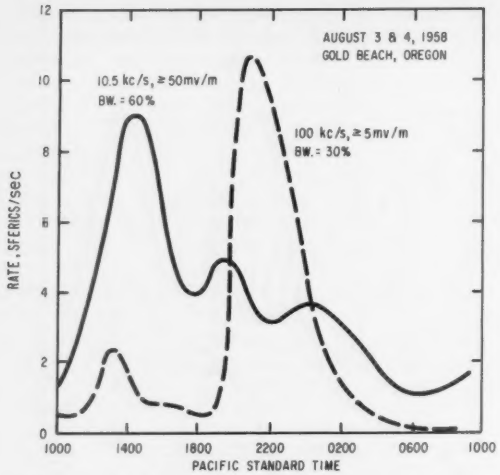

FIGURE 5. *Comparison of 10.5 and 100 kc/s rates.*

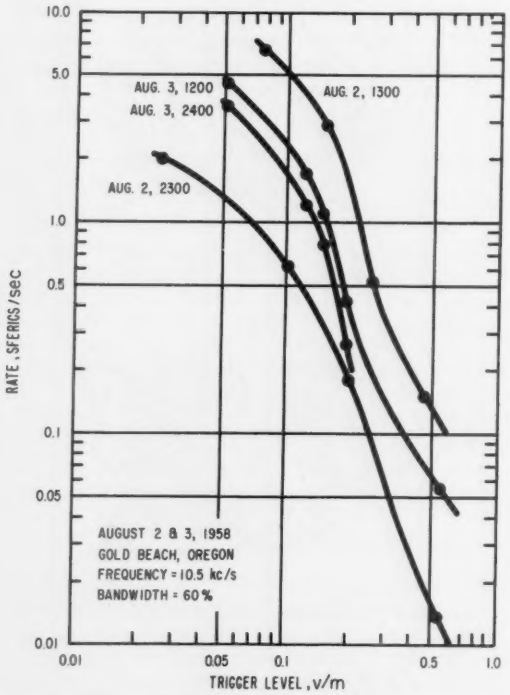

FIGURE 6. *Examples of sferic rate distributions as a function of triggering level.*

3. Directional Data

3.1. Correlation of Azimuthal Plots and Weather Data

The foregoing data provide no clue as to the direction from which the sferics came. The phenomenon being measured can be better explained by use of azimuthal scans of the sferic activity. Comparison

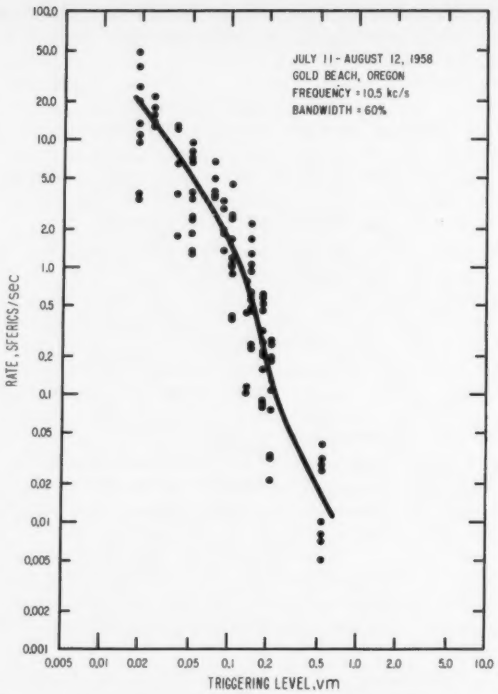

FIGURE 7. *Mean sferic rate distributions from period July 11 to August 12, 1958.*

of these scans with the occurrence of thunder or visible lightning reported by the U.S. Weather Bureau provides some further understanding of the subject. See also [10] and [11].

Figures 8 through 10 include a wide variety of thunderstorm conditions. Each symbol indicates that a weather station reported thunder or visible lightning at approximately the hour shown on the maps. Linear polar plots of sample sferic rates measured at Gold Beach, are superimposed to show the comparison with the reported lightning.

In figure 8, only three stations reported lightning. The azimuthal scan seems generally to agree with the reports, but does not show three distinct lobes in the expected directions. There are several factors which could explain the lack of agreement between such sferic measurements and available weather data. For example:

1. The available weather data are not complete. In the meteorological data used a number of weather stations had not reported.
2. Lightning is less obvious in daylight than at night. More distant lightning will probably be reported at night than during the daytime.
3. In the available reports no distinction was made between a single stroke of lightning and an intense electrical storm.
4. In some areas weather stations are so widely separated that thunderstorms and especially the visible lightning or audible thunder often escape observation.

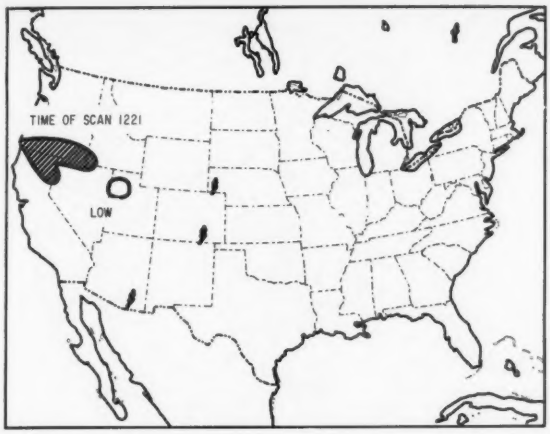

FIGURE 8. *Comparison of azimuthal scan with reported lightning, July 16, 1958.*

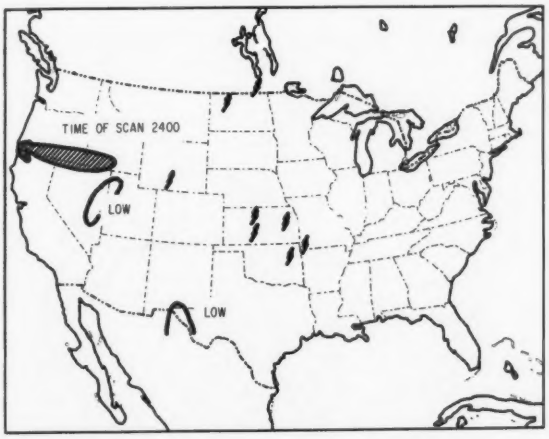

FIGURE 9. *Comparison of azimuthal scan with reported lightning, July 16, 1958.*

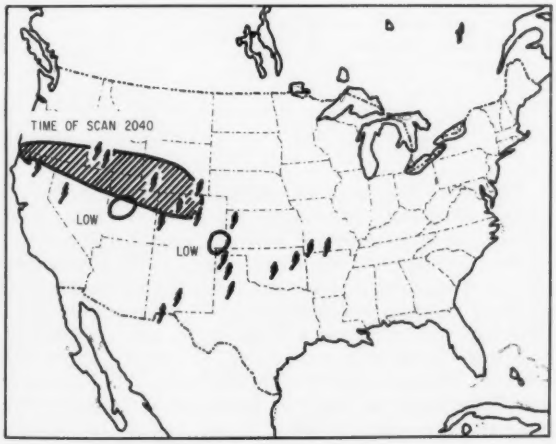

FIGURE 10. *Comparison of azimuthal scan with reported lightning, July 16, 1958.*

The correlation between the reported lightning and the azimuthal scan at 0100 (fig. 9) earlier the same day is somewhat better than at 1300 (fig. 8). The small lobe (fig. 9) to the north-east corresponds to the thunderstorm activity along the North Dakota-Manitoba border, while the large lobe to the east seems to be composed largely of sferics from the storm in south-central Wyoming. The lightning reported in Kansas, southwestern Missouri and northeastern Oklahoma is at roughly twice the range of the Wyoming storm. Correspondingly, a smaller percentage of sferics from the more distant storm would exceed the triggering level. The main lobe shows sferics from this direction, but the Wyoming storm appears predominant.

A small and somewhat irregular lobe to the south-east is rather conclusive evidence that lightning was occurring in that direction also. While no lightning was reported, two low-pressure areas in that direction are shown. It is entirely possible that unreported lightning was taking place in either or both of these areas. A further possibility is that a number of these sferics were of more distant origin, representing only the very large discharges from a storm in Central or South America.

By late evening that same day the thunderstorm activity was widespread throughout the Central and Western States (see fig. 10). This sferic rate plot is more consistent with the reported lightning.

A linear polar plot of sferic rates conveys immediately and simply a clear notion of the direction in which the bulk of the sferic activity exists. But frequently, significant amounts of sferic activity in some directions may represent a very small fraction of the maximum and cannot be successfully shown on a linear plot. A polar logarithmic plot overcomes this difficulty: however, it is impossible to define zero on such a plot and when no sferics are observed in a given direction there is a break in the curve. In many cases only one sferic may be counted in a particular direction during the course of a systematic set of measurements. The single sferic count can be reduced to a value of rate and plotted along with the rest of the data, but while correct dimensionally, statistically the sample is not adequate. In view of these limitations the logarithmic plots are more suitable for presenting averaged data (figs. 12 and 13) than data obtained during a single scan (fig. 11).

Figure 11 is a logarithmic polar plot of an azimuthal rate scan made July 30, 1958, between 1030 and 1130 P.s.t. A 6° sector was rotated clockwise in 6° increments. The sferics were counted for a period of exactly 1 min on each heading. In this case the triggering level was 50 mv/m and, therefore, more sferics from greater distances were recorded than shown in figures 8, 9, and 10 where the triggering level was 85 mv/m. The main lobe at 70° follows the general pattern of the other plots but in contrast, several storms in the western half of the azimuth circle were evident at that time.

A large number of azimuthal scans were averaged to provide a more representative measure of the sferic activity during July and August. The data

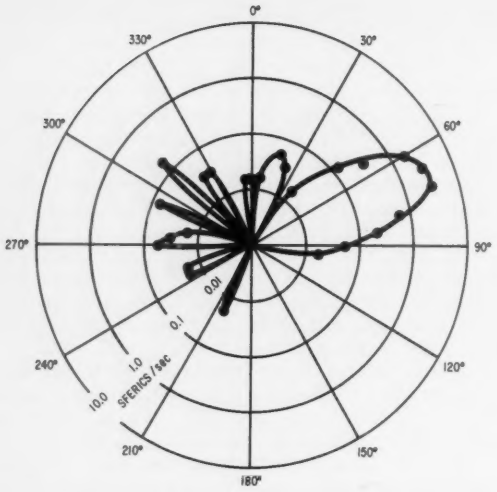

FIGURE 11. *Azimuthal scan of sferic rate, July 30, 1958: 1036 to 1135 P. s. t.*

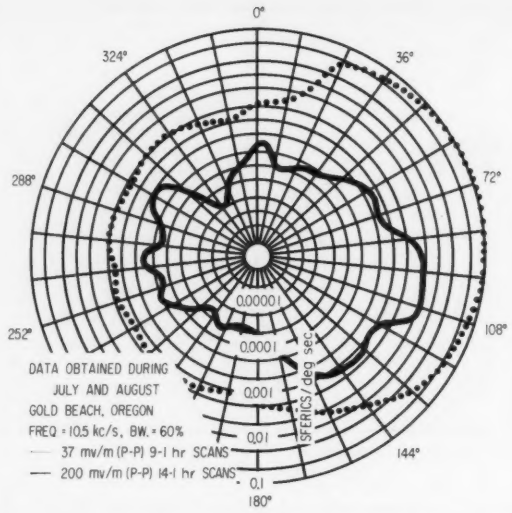

FIGURE 12. *Average sferic rate as a function of azimuth.*

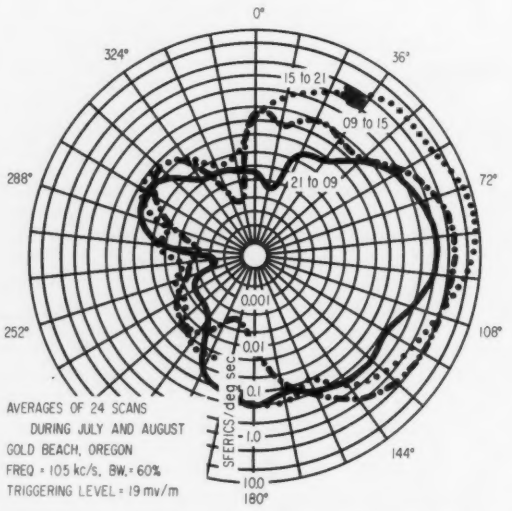

FIGURE 13. *Average rate over 24-hr period in three time blocks.*

were averaged in two ways: First by selecting scans which were well distributed over the diurnal cycle, and second by arranging the data in time blocks. These average values are plotted in figures 12 and 13, respectively.

It is evident that the two curves in figure 12 are generally similar but the 200-mv/m curve is much more variable. This variation is partly caused by the difference in triggering levels. The quantity of data (that is, the total number of sferics counted) in the 200-mv/m curve is considerably less than that in the 37-mv/m curve. The total amount of data, especially that at the 200-mv/m level, was evidently not great enough to average out completely the day-to-day variations on a statistical basis.

An additional factor is that the data for the two curves were not recorded simultaneously. Thunderstorms do not occur in the same places every day so the distance from the storms to the receiver was variable. In regions where storms occur frequently, an average value for such distances may be established within a few days but in regions where storms rarely occur, limited observations will not establish a reliable average.

Figures 12 and 13 may be compared with the U.S. Weather Bureau charts [12] of thunderstorm days shown in figure 14 and the summer thunderstorm diurnal storm counts shown in figure 4. A thunderstorm day is defined as a day on which thunder is heard. In counting thunderstorm days no distinction is made between a single clap of thunder and one or more intense electrical storms; however, in figure 4, the distinction is that each individual thunderstorm is reported separately. The average rate curves, figures 12 and 13, correlate well with known regions of intense activity indicated in both figures 4 and 14.

Figure 12 indicates an increase in sferic rate at the higher sensitivity (37 mv/m) from about 12° to 156°. These azimuths subtend both the mountains and the central plains. At the lower sensitivity (200 mv/m) the maximum has shifted southward and the greatest activity is found in the interval between 80° to 156°. The location of these storms were not established, but these azimuths include the Central Plains, the Gulf of Mexico, and South America. The ratio of the sferic rates for the two sensitivities at any given azimuth indicates the relative number of large sferics compared to the small ones. These ratios are approximately 12 to 1 toward the west (240° to 312°)

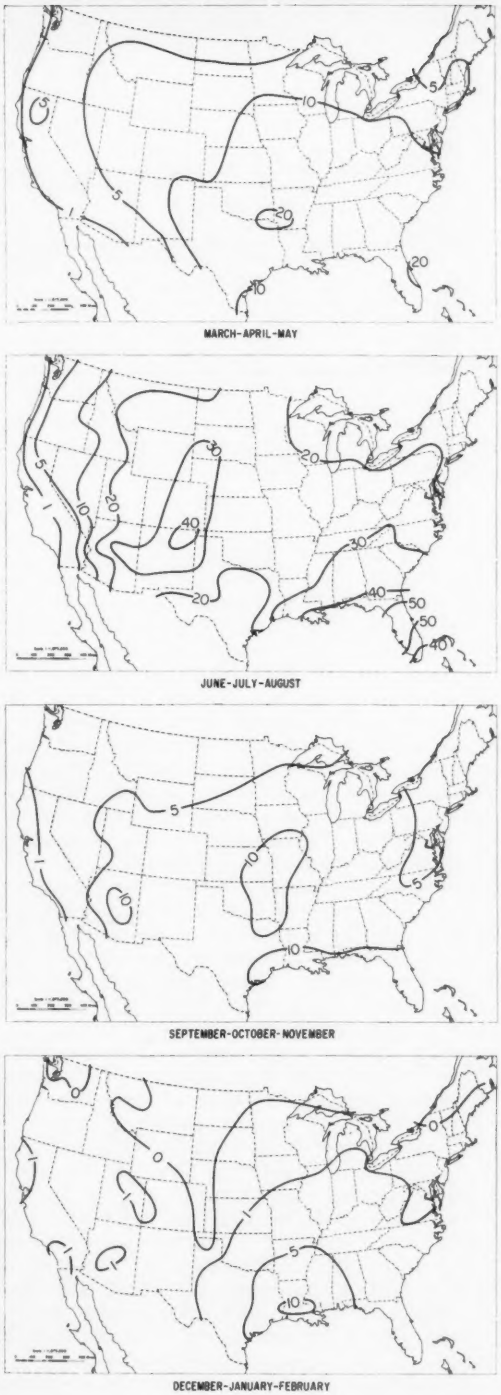

FIGURE 14. *Thunderstorm days in three-month periods.*

and toward the southeast (108° to 156°) but they increase to as high as 125 to 1 to the northeast and east (24° to 90°). These widely differing ratios may be related to source characteristics and propagation differences over land and sea paths.

In figure 13 the observed sferic rates were averaged and grouped in three time blocks. These curves may be compared with the average thunderstorm counts in figure 4. Unfortunately, different time blocks were chosen in the two figures, but they seem to be at least generally consistent. Data during the early morning hours, 0300 to 0900, was extremely sparse. In order to show the azimuthal relationship of sferic activity through a complete diurnal period this data was combined with the data from 2100 to 0300. Such grouping reduces the average rates below what they should have been from 2100 to 0300.

Small but rather pronounced peaks in all three time blocks are seen in the vicinity of 300° to 312°, and the diurnal variations in these peaks are small. Since these peaks are not evident in the curves at lower sensitivity (figure 12), it is presumed that these sferics are of distant origin (Japan, Philippines, or Borneo-Sumatra area) and that only the largest ones exceeded 19 mv/m at Gold Beach.

3.2. Comparison of Data From Two Storm Areas

When the sferics in a narrow sector are observed for an extended period of time (in contrast to the brief periods on each heading in the azimuthal scans), better statistical samples can be obtained. In this connection, the distribution of amplitudes is of particular interest because it would be desirable to associate such distributions with individual storms. However, there was no adequate independent verification that the sferics from a particular storm were isolated and, for that reason, positive conclusions from these data are not warranted. Nevertheless, the data are of interest and are presented with a possible explanation.

A 40-minute sample of data observed in three adjacent sectors gave the distributions shown in figures 15 through 18. The time indicated is G.m.t. which corresponds to P.s.t. of 1820 to 1900 on August 26. Available weather maps for this period indicated there were thunderstorms in the vicinity of the Nevada, Utah border and scattered thunderstorms in west Texas. The sectors were centered on 106°, 111°, and 116° true azimuth as shown in figure 19. The outer sectors were 6° wide and the center sector was 4°. The triggering level was 50 mv/m p-p.

The amplitude distributions of the broadband waveforms (1 to 150 kc/s) and components of the spectrum at frequencies of 10.5, 40, and 100 kc/s (30% bandwidth) are plotted in figures 15 to 18, respectively. The obvious characteristics of these distributions are: (1) The similarity between the 10.5- and 100-kc/s data, and (2) the lack of similarity between these data and the 40-kc/s data. It is suspected that the nature of these distributions is closely linked with the different types of lightning

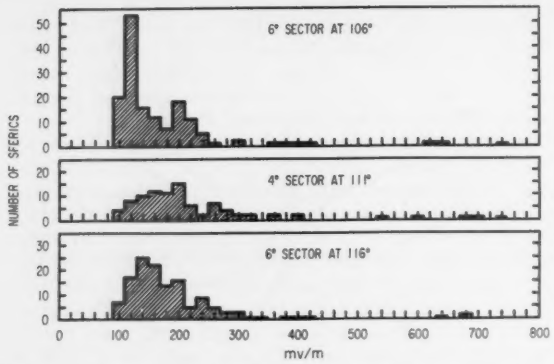

FIGURE 15. *Amplitude distribution of broadband waveforms, Gold Beach, Oregon: August 27, 1958, 0220 to 0300.*

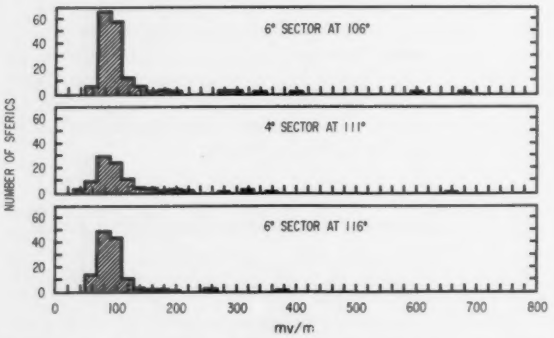

FIGURE 16. *Amplitude distribution of 10.5 kc/s component, Gold Beach, Oregon: August 27, 1958, 0220 to 0300.*

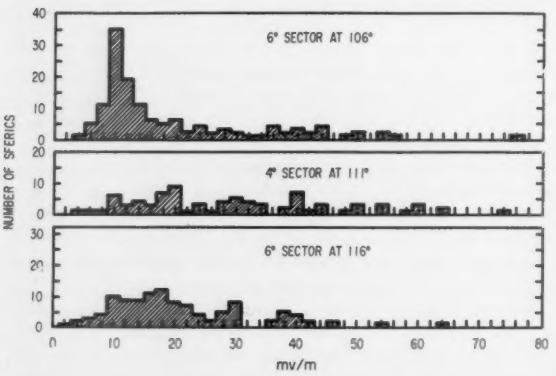

FIGURE 17. *Amplitude distribution of 40 kc/s component, Gold Beach, Oregon: August 27, 1958, 0220 to 0300.*

discharges [13] and propagation characteristics. The large sferics produced by the cloud-to-ground discharges probably account for the scattered large amplitudes in both the broadband and 10.5-kc/s distributions. The cloud-to-cloud and intracloud discharges probably account for the pronounced groupings at the lower amplitudes. The dissimilarity among the 40-kc/s distributions is not understood.

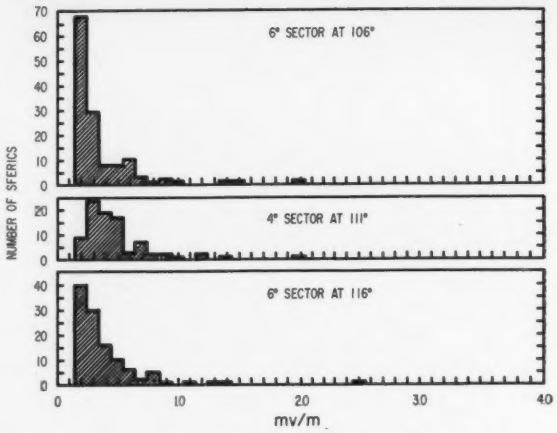

FIGURE 18. *Amplitude distribution of 100 kc/s component, Gold Beach, Oregon: August 27, 1958, 0220 to 0300.*

In November 1958, similar measurements were made at Boulder, Colo. During the course of the measurements the U.S. Weather Bureau reported a low-pressure area in the Gulf where thunderstorm conditions existed. The weather conditions between Boulder and the Gulf were such that the possibility of lightning occurring was extremely remote. The peak of the sferic activity as determined by an azimuthal scan correlated perfectly with the center of the reported low-pressure area (see fig. 19). The cumulative distribution of the 10.5-kc/s component of the sferic amplitudes from this direction are shown in figure 20 along with the cumulative distribution of the data from figure 16.

In obtaining the data the receiver triggering level was varied in steps over a wide range beginning at 10 mv/m. The sferic rate was determined at each step. It is of special interest to note that the slope of the curve rapidly approaches zero below 20 mv/m, indicating that virtually all the sferics in that sector exceeded the threshold sensitivity.

The data for the other curve (Nevada storm) were obtained by operating the receiver at a fixed threshold sensitivity of 40 mv/m, while the amplitudes were scaled from film recordings. In that case virtually all the sferics exceeded a field strength of 60 mv/m, again indicating that all the sferics from that sector were received.

These results would be expected if a single storm area existed in the sector and if the receiver sensitivity were increased sufficiently to detect all the sferics from that storm area. Evidently the storm areas established from the independent weather reports accounted for the observed activity within the sector.

Entirely similar results were published by Horner [14] where he found that all the sferics from a storm at a distance of 500 km exceeded 1.6 mv/m (300-c/s bandwidth). The greatest sensitivity used was 0.4 mv/m. The smaller sferics from two other storms

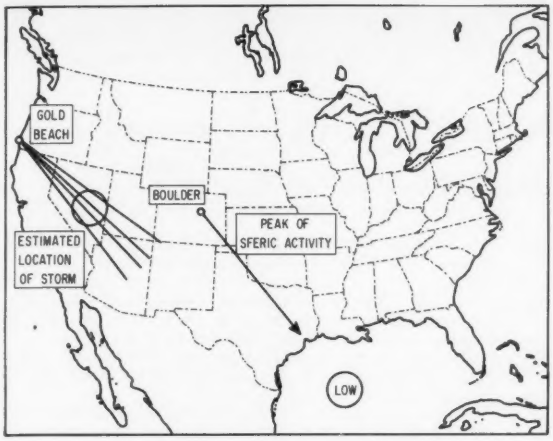

FIGURE 19. *Nevada and Gulf storms.*

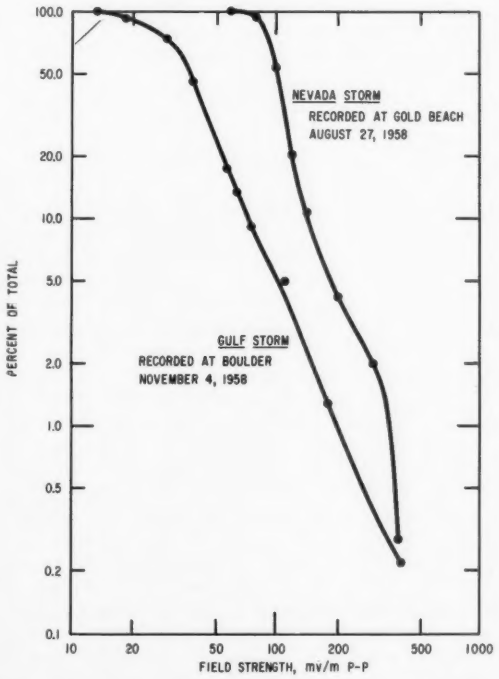

FIGURE 20. *Cumulative distributions of Nevada and Gulf storms.*

at 5,000 and 8,000 km did not exceed the 0.4-mv/m threshold, but it is presumed that similar lower limits existed.

The narrow bandwidths commonly used restrict the lower level at which individual sferics can be resolved because of the ringing effect of the higher Q circuits. The measurements reported herein were made with wide-band filters (30 to 60%) to provide substantially better resolution at higher sensitivities.

At the lower sensitivities the curves in figure 20 appear relatively straight, but with different slopes. Since one storm area was evidently over sea water and the other over mountainous area, it is suspected that the differences are related to the topography. The generally steeper slope of the distribution from the land area indicates that there were relatively fewer large sferics in this storm area. This, along with the other data that indicated larger sferics over sea water, might be explained by the higher conductivity on the sea water which might permit a greater surge of discharge current to flow.

4. Future Measurements

Measurements made from a single location do not provide fix information which is necessary for a more complete analysis of the data. In any future measurement program a minimum of two sets of equipment should be located in a configuration that would yield good fixes in the areas of interest. A third set of equipment appropriately located would further enhance the scope and usefulness of the data.

With two or more sferic stations linked together with telephone lines, instantaneous fix data could be obtained. Such data would give a current indication of thunderstorm activity and should be valuable to air navigation, weather reporting and forecasting, and other purposes.

Future long-term measurements could provide statistical data on the location and frequency of occurrence of thunderstorms and statistical classification of sferic characteristics as they relate to meteorological phenomena throughout the different seasons. Such statistical data would aid prediction services and should eventually yield a better understanding of thunderstorm activity in general.

Additional measurements should also stimulate the development of mathematical models of sferic activity. Such models should take into account explicitly the physical factors that determine the mechanism by which sferics originate. In the formulation of these models, the effect of topographical and meteorological factors should be carefully studied. The achievement of these models can result only from a closely coordinated effort in both the theoretical and experimental fields.

Sferics may be used as tools for evaluating the physical properties of propagation paths. For example, observation of the groundwave component of one or more sferics occurring on the extension of a line joining two stations provides the necessary data from which the ground conductivity of the path can be deduced [15].

The measurements and analyses reported herein were sponsored in part by the U.S. Air Force Cambridge Research Center, Air Research and Development Command. The authors also acknowledge the engineering contributions of E. L. Berger and T. L. Davis, and the assistance of C. A. Samson in relating the data to weather observations.

5. References

[1] H. R. Byers, ed., Thunderstorm electricity, ch. XI (University of Chicago Press, Chicago, Ill., 1953).

[2] Lee R. Tepley, A comparison of sferics as observed in the very low frequency and extremely low frequency bands, J. Geophys. Research **64,** 2315 (1959).

[3] A. D. Watt and E. L. Maxwell, Characteristics of atmospheric noise from 1 to 100 kc, Proc. IRE **45,** 787 (1957).

[4] J. Ralph Johler and Lillie C. Walters, On the theory of reflection of low- and very-low-radiofrequency waves from the ionosphere, J. Research NBS **64D,** 269 (1960); J. Ralph Johler, W. J. Kellar and L. C. Walters, Phase of the low radiofrequency ground wave, NBS Circ. 573 (June 26, 1956).

[5] J. R. Wait, Transmission loss curves for VLF propagation, Trans. IRE **CS–6,** 58 (1958); see also supplement to above which includes a presentation of mode calculations.

[6] J. R. Wait and H. H. Howe, Amplitude and phase curves for ground-wave propagation in the band 200 cycles per second to 500 kilocycles, NBS Circ. 574, U.S. Government Printing Office (1956); (fairly extensive calculations based on the Van der Pol-Bremmer theory).

[7] J. R. Wait and A. Murphy, The geometrical optics of VLF sky wave propagation, Proc. IRE **45,** 754 (1957).

[8] H. R. Byers, ed., Thunderstorm electricity, ch. XII (University of Chicago Press, Chicago, Ill., 1953).

[9] G. Hefley, R. H. Doherty and E. L. Berger, An intermittent-action camera with absolute time calibration, 1959 IRE-WESCON Conv. Record, pt. 6 (Aug. 18–21, 1959).

[10] T. Kamada and J. Nakajima, On the direction of arrival of atmospherics at Toyokawa, Proc. Research Inst. Atmospherics, Nagoya Univ. (Jan. 1954).

[11] A. Kimpara, Atmospherics in the Far East, Proc. Research Inst. Atmospherics, Nagoya Univ. (Nov. 1955).

[12] Mean number of thunderstorm days in the United States, U.S. Weather Bureau, Tech. Paper 19 (Dec. 1952).

[13] J. Chapman, The waveforms of atmospherics and the propagation of very low frequency radio waves, J. Atmospheric and Terrest. Phys. **11,** 223 (1957).

[14] F. Horner, The relationship between atmospheric radio noise and lightning, J. Atmospheric and Terrest. Phys. **13,** 140 (1958).

[15] J. R. Johler and L. C. Walters, Propagation of a ground wave pulse around a finitely conducting spherical earth from a damped sinusoidal source current, IRE Trans. **AP–7,** 1 (1959).

(Paper 65D2–114)

JOURNAL OF RESEARCH of the National Bureau of Standards—D. Radio Propagation
Vol. 65D, No. 2, March–April 1961

Effect of Antenna Radiation Angles Upon HF Radio Signals Propagated Over Long Distances[1]

W. F. Utlaut

(July 21, 1960)

Observations of a HF continuous wave radio signal which after propagating over east-west paths 6800 and 8400 kilometers in length were received on antennas having different vertical-plane radiation angles indicate that very low radiation-angle antennas may be advantageous for use in long-distance communication systems.

Much of the time, hourly median signal levels received on antennas with radiation angles less than 2 degrees exceeded those received at angles of 15 degrees by 10 decibels while signals received at angles between 2 and 5 degrees were 5 decibels greater than those received at 15 degrees.

No significant change in the fade rate of the signal received at various radiation angles was found.

A limited amount of data obtained during ionospheric storms suggests that the radio signal received on a low radiation-angle antenna is deteriorated by storm effects for a shorter time, and to a lesser degree, than is the signal received by a high radiation-angle antenna.

1. Introduction

In the design of antennas for use in ionospheric scatter and tropospheric communication systems, considerable attention has been given to the optimization of the radiation angle (vertical angle of radio wave radiation). In long-distance high-frequency communication circuit design, however, little attention has been paid in many cases to this parameter. In part this may be because HF radio signals seem to be receivable on almost any antenna, although not necessarily with the reliability desired in modern communication systems, and in part because the longer wavelengths of radio waves in the HF band require high antennas if low radiation angles are called for and result in greater antenna construction costs, and in part because the optimum radiation angle is more difficult to predict and more variable then for the other two examples.

Potter and Friis [1][2] in a short experiment in 1932 compared the signal strengths received on two antennas with different radiation angles for propagation paths between New Jersey and South America as well as between New Jersey and England and found that significantly stronger signals were received on the lower radiation-angle antenna for both horizontal and vertical polarizations.

Hallborg and Goldman [2] in a 1947 paper presented results of angle-of-arrival measurements made during September to December 1941 on a path between Riverhead, N.Y. and Bolinas, Calif. Measurements were made only between the hours 0900 and 2000 e.s.t., during most of which time the entire path was in the sunlight. The circuit path length was about 4000 km, a distance which is normally considered as the maximum range for 1-hop propagation. The angles of arrival reported were all greater than 5° and tended to be grouped around values appropriate for 2 and 3-hop propagation modes. It is not clear whether the equipment was capable of measuring the low angles required for a 1-hop mode. Signal intensity measurements made in 1945 over this same path were made utilizing rhombic antennas with radiation angles at 8.5 and 12.5°. A major conclusion of the results shown by this test was that a fixed-beam type of high-frequency antenna will not give maximum performance at all seasons or times of day.

Angle-of-arrival measurements were made in England by Wilkins and Kift [3] during daylight hours over the transmission path at various times between October 1952 and January 1954. Utilizing pulse signals from Negombo, Ceylon, 8700 km from the receiver at Slough, England, it was found that the strongest ray arrived predominately at angles of 7° ±2° except during the summer when signal levels were too low to record. Similar measurements on a 7200-km path between Kirkee, India, and Slough showed that the predominate angles of arrival of the strongest ray were, during winter 7½° ±2° and during summer 5° ±2°. Frequently, angles of 3 to 4° were observed on both paths; however, as the authors point out, very low angles of elevation were discriminated against by both the receiving and transmitting antennas.

Occasional oral reports tend to suggest that certain long distance HF circuits which have terminals with low radiation-angle antennas provide extraordinarily good signal reception over periods of time greatly exceeding that normally expected.

[1] Contribution from Central Radio Propagation Laboratory, National Bureau of Standards, Boulder, Colo.

[2] Figures in brackets indicate the literature references at the end of this paper.

To provide a better understanding of the relationship between signal characteristics and antenna radiation angle a long-distance cw radio experiment was undertaken, the results of which are presented here.

2. Experimental Arrangement

Through the cooperation of the United States Information Agency a cw radio signal at a frequency of 20.06 Mc/s was transmitted from a Voice of America station in Munich, Germany on a 24-hour-a-day, 5-days-a-week schedule. The Munich signal was received at sites in the vicinity of Boulder, Colorado and at the National Bureau of Standards Sterling, Virginia Field Station, near Washington, D.C., on antennas having different effective heights and radiation angles. Great-circle distances from Munich to the receiving sites are: to Boulder 8400 km (5200 miles) and to Sterling 6800 km (4200 miles).

2.1. Transmitting Antennas

Voice of America communication commitments made it necessary to alternate transmission of the 20-Mc/s signal between two rhombic antennas which were not quite identical although both were aimed on a bearing of 295°. One rhombic antenna designated as 6E was used during the period 0000–0700 m.s.t. and the second antenna designated as 2W was used for the remainder of a 24-hour period with the exception of the period 0700–0800 m.s.t. during which time transmitter maintenance was performed and no signal was transmitted.

The bearing of Sterling from Munich is 297° and the antenna beam maximum at 295° was thus oriented nearly along the propagation path. The bearing of Boulder from Munich, however, is 316°, 21° off the main lobe direction. Fortunately, however, each of the rhombics produced strong side lobes approximately in the direction of Boulder.

Utilizing Foster's stereographic representation method for obtaining rhombic antenna patterns [4], it was calculated, at the frequency of operation, that the elevation of lobe maximum for the bearing of 295° was 10.5° for antenna 2W and 12° for antenna 6E with antenna 2W having approximately 1.1 db greater gain. In a similar manner it was found that a side lobe of antenna 2W was produced at a bearing of 317° and elevation of 16° while antenna 6E had a side lobe on a bearing of 315° elevated 12° above the horizon. The side lobe of antenna 6E provided a signal approximately 2.9 db greater than that of antenna 2W.

2.2. Receiving Antennas

Receiving antennas used at Boulder were half-wave horizontal dipoles with a reflector and were matched into a 50-ohm transmission line. The reflector was used to minimize the effect of signals coming in from the back side of the antenna due to reflections from nearby mountains. In all, five receiving antennas were used at Boulder and the height advantage of nearby mesas was used where possible to provide effective antenna heights ranging from 50 to 985 ft. The elevation angles of the first lobe from these antennas at the signal frequency were calculated to range from 0.7 to 15.6°. Table 1 shows the effective height and calculated radiation angle for the Boulder antennas which are designated in order of ascending height as 1B through 5B.

At the Sterling receiving site three identical half-wave dipole antennas, again matched into a 50-ohm transmission line, were installed at different heights on a 320 ft tower. Effective heights and calculated radiation angles for these antennas which are designated as 1S, 2S, and 3S are also tabulated in table 1. Antennas with radiation angles as low as those provided by antennas 4B and 5B at Boulder were not employed at Sterling because of the great tower height required.

Double conversion heterodyned receivers with mechanical filters in the second IF stage which limited the receiver bandwidth to 800 c/s were used and the AVC signal level was recorded.

Fading rate recorders were used in conjunction with the receivers during a portion of the recording period at both the Sterling and Boulder receiver locations. A discussion of the recorders is provided in ref. [5].

3. Experimental Results

3.1. Signal Strength, Munich-Boulder

Monthly median values of the signal strength in dbw (decibels above 1 watt) received on each of the five antennas at Boulder are shown in figures 1 through 4 for the months March through June of 1959. Also shown are the times during which the signal frequency exceeded the predicted value of MUF as obtained from CRPL Series D information. The median values shown here represent signal power; i.e., the noise power level, which was determined during a 5-min period each hour when the transmitter was off, has been subtracted from the median value of signal-plus-noise power measured in the same hour.

It may be observed in figures 1 to 4 that the received signal strength, at a common distance from the transmitter, is dependent in some manner upon the radiation angle of the receiving antenna but it is also evident that no single radiation angle always provides a signal of greatest amplitude. In March and April it may be seen that the antenna with the

TABLE 1.

Boulder Antenna	Height	Radiation Angle
	ft	*deg*
1B	50	15.6
2B	135	5.2
3B	310	2.3
4B	485	1.4
5B	985	0.7
Sterling Antenna		
1S	50	15.6
2S	150	4.7
3S	312	2.3

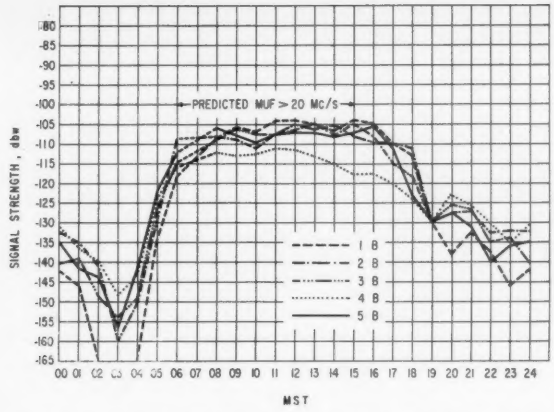

FIGURE 1. *Hourly median signal strength, Munich-Boulder, March 1959.*

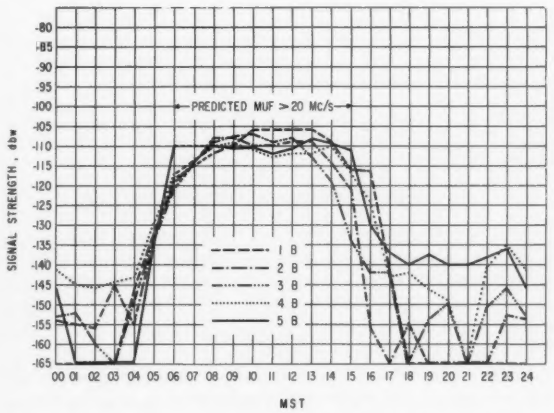

FIGURE 2. *Hourly median signal strength, Munich-Boulder, April 1959.*

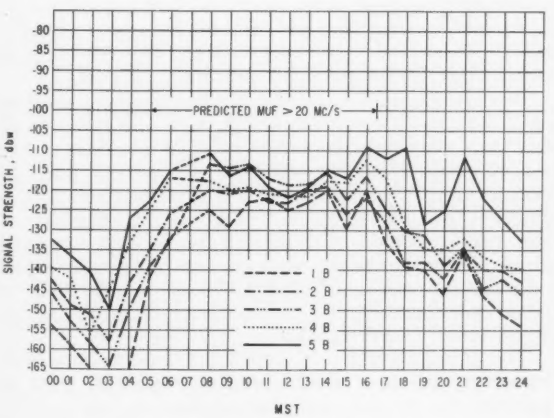

FIGURE 3. *Hourly median signal strength, Munich-Boulder, May 1959.*

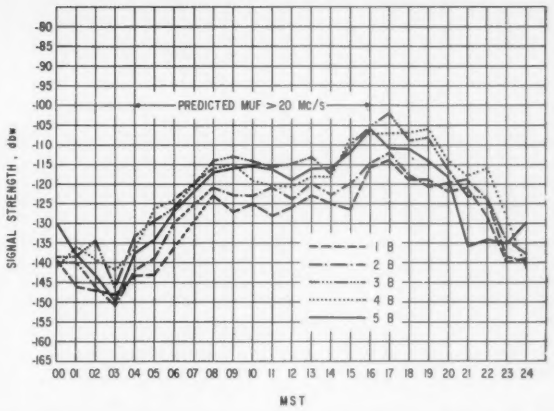

FIGURE 4. *Hourly median signal strength, Munich-Boulder, June 1959.*

highest radiation angle, 1B, received a signal of greater strength than the other antennas during a substantial portion of the period when the predicted value of MUF exceeded the signal frequency but that it generally produced the lowest signal level at other times of the day. In May and June this same antenna usually provided the weakest signal throughout the entire day. Another feature which may be noted is that the separation between signal levels received by the various antennas is greater in May and June than it is in the earlier two months with higher signal intensities prevailing on the lower radiation-angle antennas. These results suggest: (a) That a seasonal change in the angle of arrival of the signal on this path, progressing from higher angles toward lower angles, occurs as the ionosphere makes the transition from winter to summer conditions and (b) that angles of arrival, even under winter ionospheric conditions, in the period somewhat beyond the predicted MUF (monthly median) are substantially lower than they are during the period when the signal frequency is less than that of the predicted MUF.

To enable a better comparison of the relative merit of each antenna to be made, figures 5 and 6 are presented. These show a portion of the signal-strength time-distribution curve for each antenna during the 4-month period March through June. Figure 5 shows the results of all data, irrespective of time of day, while the curves in figure 6 were obtained by using data only from those periods of time when the predicted MUF value was less than the signal frequency. In each of the figures it is evident that the antenna with the highest of the five radiation angles, 1B, received the weakest signal for any particular percent of time. The data for antennas 2B and 3B tend to group together and show a signal level approximately 5 db higher than that of antenna 1B for a comparable percentage of time. The signal levels received on the two antennas with the lowest radiation angles, 4B and 5B, similarly tend to group together and are 10 db, or more, higher than those from antenna 1B.

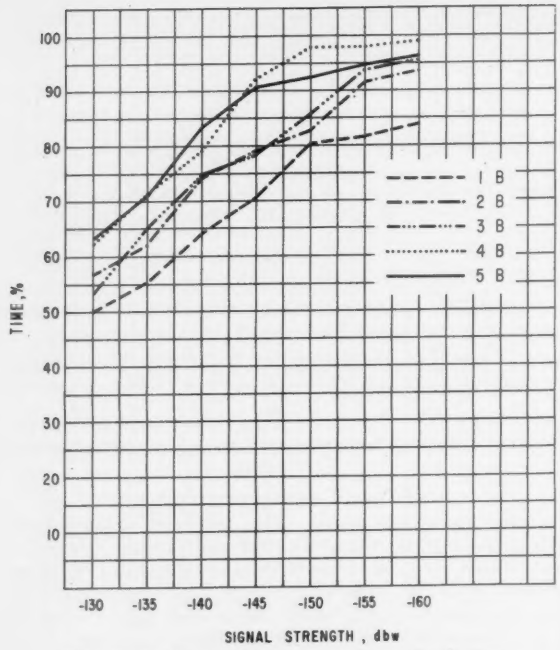

FIGURE 5. *Percent of time signal exceeds abscissa.*
Average of 4 months for all times, Munich-Boulder.

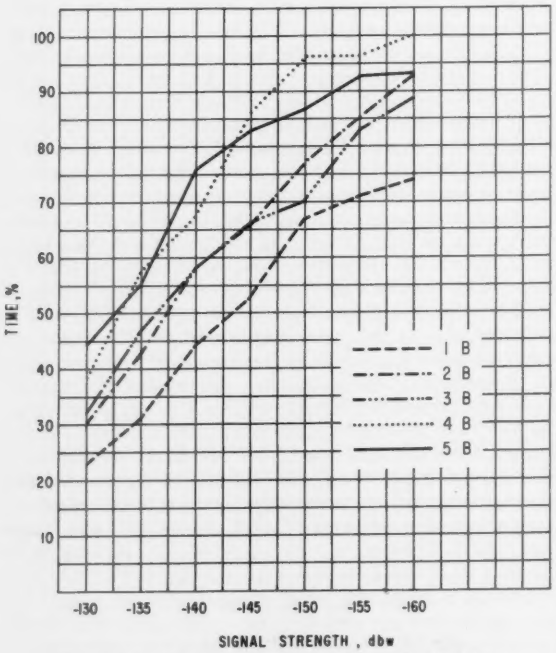

FIGURE 6. *Percent of time signal exceeds abscissa.*
Average of 4 months for those times when predicted MUF <20 Mc/s, Munich-Boulder.

The results found here suggest that over a substantial proportion of time a large amount of energy arrives at low angles, perhaps on the order of a degree or so. This fact is interesting particularly when it is noted that an optimum angle of radiation for this path, based upon a 3-hop geometrical mode and a 300-km ionospheric height, is 6°. It also may be remarked that the increase in received signal strength on the antennas with low-radiation angles occurred even though the major portion of energy from the transmitting antenna was radiated at fairly high angles of 12 to 16°.

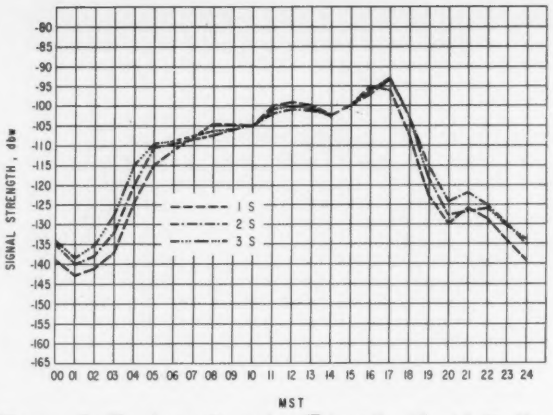

FIGURE 7. *Hourly median signal strength, Munich-Sterling, May, June, July 1959.*

3.2. Signal Strength, Munich-Sterling

On the shorter path between Munich and Sterling, Virginia, signal levels in dbw were recorded during a two and one-half month period from the middle of May through July 1959. The hourly median signal strength recorded on the antennas 1S, 2S, and 3S for this period are shown in figure 7.

CRPL Series D predictions for the May–July recording period indicated that normal *F*-layer propagation for the path was expected between the hours 1300 to 1800 m.s.t., approximately, and was limited to this short interval because of *F*-layer conditions at the western control point, 2000 km from the receiving terminals where low MUF values existed. In figure 7 it may be seen that the strongest signals, on all antennas, were received during this period when *F*-layer propagation could have existed.

Predictions also indicated that radio propagation over this path was expected nearly 100 percent of the time between the hours of 0400 to 1800 m.s.t. via sporadic *E* at the western end of the path in conjunction with *F*2 or sporadic-*E* reflections at the Munich end of the path. The sloping plateau of the median curves in figure 7 extends over a length of time corresponding approximately to that when propagation was predicted and during this time it may be observed that median signal levels on all antennas were comparable.

During the period of time when predictions indicated propagation would not be expected, 1800 to 0400 m.s.t., it was observed, except during periods of ionospheric disturbances, that signals, although considerably lower in amplitude than those received

during the predicted propagation period but still well above noise level, were received nearly all the time on all three antennas. In figure 7 it may be seen that higher median signal levels were received by the two lower radiation-angle antennas during this period than were received by the high radiation-angle antenna, 1S, even though a significantly greater amount of power is transmitted at the high angle.

A comparison of the relative merit of the three Sterling antennas is provided in figure 8 where a portion of the signal-strength time-distribution curves are shown. Here, as in the case of the longer propagation path between Munich and Boulder, lower radiation-angle antennas received signals of greater strength a substantial portion of the time. More than 50 percent of the time, hourly median signal levels received at radiation angles of 2.3° were about 5 db greater than those received at an angle of 15°. An interesting result to note in comparing figures 5 and 8 is the tendency toward a 5-db difference in median signal level recorded with antennas 1S and 3S as well as 1B and 3B where each pair have corresponding radiation angles at the terminus of the 6800-km and 8400-km paths.

3.3. Signal Fading Rates

To ascertain whether marked differences in the fading characteristic of the received signal due to antenna height variations existed, two fading rate recorders were utilized in conjunction with certain antennas from the middle of May through July 1959. One meter was used at Boulder to record the fading of the signals received on antennas 3B and 4B, alternating from one to the other at 24-hr intervals. A second meter was used at the Sterling site alternating between the signal received on the three antennas in sequence at 24-hr intervals.

Distribution curves of the fading rate of the received signal obtained from these measurements are shown in figure 9 where it may be observed that

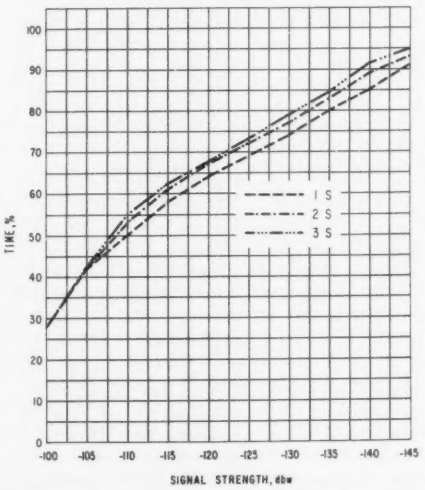

FIGURE 8. *Percent of time signal exceeds abscissa, May, June, July 1959, Munich-Sterling.*

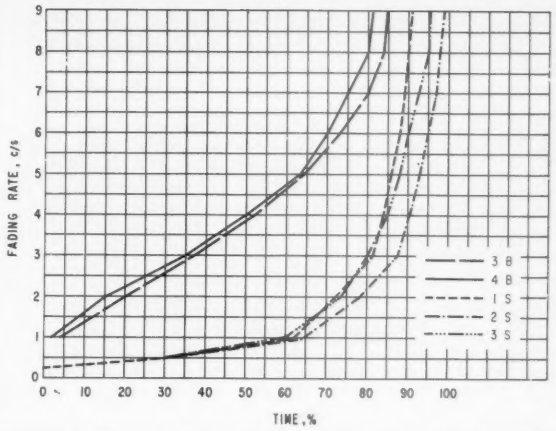

FIGURE 9. *Percent of time fading rate less than ordinate, May, June, July 1959.*

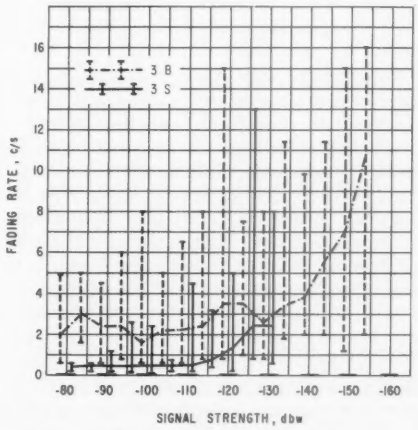

FIGURE 10. *Fade rate distribution.*

during much of the time little difference in the fading rate of signals received on antennas with different radiation angles occurs. For some 20 percent of the time, however, a difference of 1 c/s or greater in fading rates, apparently associated with antenna radiation angles, is evident.

In figure 9 it is apparent that the signals received at Boulder faded at higher rates than did those received at Sterling. This is again indicated in figure 10 where curves comparing the median value and range of fade rate as a function of signal intensity for antennas 3S and 3B, which have the same radiation angles at Sterling and Boulder respectively, are shown. The signal received at Boulder, in addition to having a higher fade rate, generally shows a greater variability of fade rate than does the Sterling signal at corresponding signal intensities.

3.4. Magnetic Storms

During the period of time in which the Munich signal was recorded several magnetic storms occurred which provided an opportunity to observe the signal

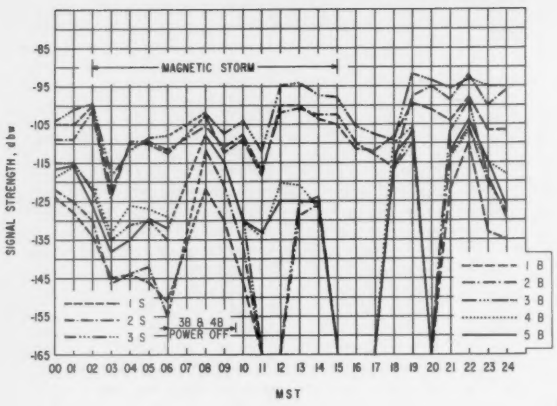

FIGURE 11. *Signal strength variation, June 11, 1959.*

characteristics in relationship to antenna radiation angles when the ionosphere was in a disturbed condition.

An outstanding example of low radiation-angle advantage is shown in figure 11 where hourly median signal intensities received on the Sterling and Boulder antennas are given for a 24-hr period on June 11, 1959 during which time a moderate intensity magnetic storm began abruptly at 0210 m.s.t. and ended shortly after 1500 m.s.t. Disturbed ionospheric conditions associated with the magnetic storm caused, at one time or another, total loss of the signal on all antennas at Boulder but a salient feature to be observed here is the differing lengths of time this occurred on the various antennas. While all antennas show a marked reduction in signal strength during the first few hours after the storm onset, with the highest radiation-angle antennas, 1B and 2B, showing the greatest signal reduction of all antennas at 0600 m.s.t., signal strengths were, by 0800 m.s.t., up to levels near the monthly median values. Following this, a decline in signal intensities occurred which resulted in the loss of signals on antennas 1B, 2B, and 3B by 1100 m.s.t. Antennas 4B and 5B did not suffer a loss of signal at this time although intensities were 15 db or more below the monthly median values. In the ensuing 9-hr period no Munich signal was evident on antenna 1B. In the same period antennas 2B and 3B did not receive any signal for a total time of 6 hr while antennas 4B and 5B did not receive a detectable signal for a total period of 4 hr. During this storm signal strengths at Sterling were, at times, as much as 25 to 30 db below the corresponding monthly median values but as may be observed in figure 11 the lowest radiation-angle antenna, 3S, received signals that were at least 5 db greater than those received on the other two Sterling antennas. Thus, during this storm, and as was generally observed during other storms, signals received on antennas with the lowest radiation angles were deteriorated the least, on both the 6800-km and 8400-km paths.

4. Discussion of Results

4.1. Diurnal and Seasonal Trends

In long-distance high-frequency radio transmission, daytime propagation by the $F2$ layer is characterized by a relatively large number of $F2$ hops. This period would have the highest angle modes and would explain why the higher angle antennas gave the strongest signals at Boulder in March and April. For sufficiently high operating frequencies there will be a time somewhat before noon over the path and again after noon, when the smallest number of geometrical $F2$ modes will prevail. Before that time in the morning and after that time in the evening waves will arrive by means of combinations of low-angle $F2$ modes with scatter or sporadic E, or multiple sporadic-E hops plus perhaps some scattering or layer tilt mode. Frequently the arriving modes will be nongreat-circle modes. All of these modes are inherently low-angle modes and would explain the fact that the signals arriving outside the hours when the operating frequency exceeds the $F2$ path MUF are low-angle signals.

In May and June the low-angle modes received at Boulder were strongest even during the hours when the MUF exceeded the operating frequency. This phenomenon is probably explicable by the fact that the increased incidence of sporadic E in May and June increased the number of possible low-angle mode combinations.

The Sterling data were obtained during a period of high incidence of sporadic E. In this case during the hours when the operating frequency was below the predicted $F2$ MUF all three Sterling antennas (corresponding to the lowest three at Boulder) gave approximately equal responses, as distinguished from the fact that for the same season the lower angle antennas were giving stronger responses at Boulder. As the path length increases, the number of possible low-angle modes increases hence, the greater response at the low angles at Boulder during a season when there could be low-angle daytime modes.

Since responses at angles are tied to specific modes there are some irregularities in the curves. Thus, even when the trends are toward low angles the very lowest-angle antenna does not always have the largest response, as the curves show.

It is interesting to note that the median signal-strength curves (figs. 1 to 4 and 7) do not show a discontinuity which could be identified as a true MUF failure but rather they show a relatively smooth transition from high-signal levels during the day to lower levels in the evening hours and rising again in the early morning hours. On the Munich-Sterling path it was observed that a good signal was received over a 24-hr period, on all three antennas, nearly all of the time during the recording period. A similar result at the higher antenna terminals of the Munich-Boulder path was observed on many occasions. Commonly used MUF prediction methods would not have led one to expect these results. In view of the need for greater efficiency in usage

of the radio spectrum it would seem most desirable that effort be made toward extending prediction capabilities in order that well designed communication systems might make use of the signals which are received beyond the time of conventional MUF failure.

4.2. Strength of Low-Angle Modes

It is surprising at first glance that although the transmitting antenna had a main-lobe radiation angle which was high for both propagation paths the low-angle responses were greater so much of the day. In one instance for the Munich-Sterling path, the expected field strength at 1700 m.s.t. for a 4-hop $F2$ mode was compared to that of a 2-hop $F2$ mode. The time chosen here corresponds to that when the maximum median signal levels were obtained at Sterling (fig. 7) and when ionospheric absorption over the path was low but the $F2$ mode of propagation still possible. The 4-hop $F2$ mode is regarded as a typical high-angle mode (14° radiation angle for a 300-km layer height) and the 2-hop $F2$ a typical low-angle mode (2.5°). Using the method of Rawer [6], which includes the effects of focusing due to a curved earth and ionosphere, it was determined that the low-angle mode should be about 6 db stronger than the high-angle one if an isotropic transmitting antenna were assumed. However, in the practical case with the transmitting rhombic described in section 2 above, the directivity at a 2.5° radiation angle is lower than that at 14° by more than 10 db [7]. The low-angle mode signal would thus have been expected to be at least 3 db lower than that of the high-angle mode and yet the actual results (fig. 7) indicated that the median value of the signal received on the low-angle antenna was 3 db greater than that received on the high-angle antenna. This leads to the qualified conclusion then, that the low-angle transmission mode is more efficient than the high-angle one. The qualified in this case refers to the fact that there were not identical antennas at the two terminals.

The fact that the total received power at the low angles was so frequently comparable to or actually greater than at the high angles indicates that there may have been a larger number of these low-angle modes. The signal strengths recorded on the various antennas actually provide a comparison of the square of the sum of amplitudes of groups of modes at one range of angles with that for another range. Pulse patterns for long-distance propagation showing the presence of numerous low-angle modes appear in a paper by Silberstein [8].

4.3. Fading

a. Variation With Antenna Radiation Angle

The relationship between radiation angle and the fade rate of the received signal is not made clear from the data for, when the fade-rate distribution curves of the Sterling antennas are not coincident (fig. 9) the rate of fading of the signal received by antenna 2S, with a radiation angle intermediate between those of antennas 1S and 3S, tends to be 1 to 3 c/s lower than that found on the other two antennas. Signals with the highest fading rate were received on the antenna with the highest radiation angle. Data for the two Boulder antennas, 3B and 4B, indicate that slightly higher fading rates are found for the signals received by the antenna with the lower of the two-radiation angles. In making this latter comparison, however, it should be noted that the radiation angles of these antennas are both relatively low so that a direct comparison between fade rates at high and low angles is not available here. In general it would appear that no significant deterioration of signal quality, because of fading-rate differences due to antenna radiation angles alone, would be expected.

b. Differences in Fading Between Boulder and Sterling Paths

The greater degree of variability and higher fade rate found in the signals recorded at Boulder as compared with those recorded at similar radiation angles at Sterling may be attributable to the difference of the radio paths in the ionosphere. It is well known that radio signals received on paths which intercept the auroral zone are frequently characterized by rapid signal fading and doppler frequency shifts. The Munich-Boulder great-circle path traverses the region of maximum auroral activity twice whereas the Munich-Sterling path does not come much closer than 1000 km to the auroral zone. The signals arriving over the former path would then be expected to show, on the average, higher fade rates than those arriving over the latter path.

4.4. Behavior During a Magnetic Disturbance

An example of low radiation-angle advantage observed during an ionospheric disturbance was presented in section 3.4. Whether the results obtained here and during a few additional storms which occurred during the recording period are generally valid will require further investigation. However, the limited amount of data of this type does indicate that the length of time during which signals are depressed in strength, or lost entirely, increases as the radiation angle of the antenna increases. The time of signal intensity reduction on the various antennas may differ by as little as a few minutes up to a time of several hours.

During ionospheric disturbances great changes in the layer heights occur, the $F2$ layer often rising to heights well above the normal ones. Considerable stratification of the region also occurs. In the auroral zones, ionization capable of reflecting higher frequency radio waves than normal is produced in the E region also during disturbances.

The above ionospheric changes probably all tend to provide, for the longer paths, more low-angle propagation modes. This may explain why antennas with low radiation angles suffer less signal deterioration from increased ionospheric absorption occurring as a result of the effects accompanying a magnetic storm than do those with high-angle response.

Although it is known that transmission over paths that lie, even in part, in the auroral zones are subject to a greater degree of irregularity than are transmissions over other paths, little is known, qualitatively, about auroral-zone absorption in general. The observations made during the course of this experiment when ionospheric storms occurred, while not capable of providing qualitative results, do indicate that a greater increase in the amount of absorption on the path traversing the auroral zone was produced as a result of a storm than there was on the path not passing through the auroral zone. The greater sensitivity to disturbance of the former path is evident in comparing the results at Boulder and Sterling in figure 11.

5. Recommendations

The data presented earlier indicates, for long-distance HF circuits, that low radiation-angle antennas appear to be advantageous. Certain factors require additional investigation, however, before categorical confirmation of the indicated trend may be asserted. As an example, it is to be noted that antennas with wide horizontal beam widths were utilized in this experiment and the results may then only be applicable when antennas with this characteristic are used if a large component of the received signal arrives on bearings differing greatly from that of the great circle path. Communication systems typically use high-gain antennas and thus have reduced horizontal beam widths. This suggests that observations of the azimuthal, as well as further vertical, direction of arrival be made with direction-finding equipment capable of measuring signals which arrive at low angles. Pulsed signal studies also would be most desirable to aid in understanding by which modes radio waves arrive at various vertical angles and how these vary diurnally and seasonally.

A factor of some importance which needs to be investigated is whether better system operation would result if low radiation-angle antennas were used for both transmitting and receiving. In view of the results found above this might be an expected result, yet it is not assured.

6. Summary

Observations of a HF cw radio signal which after propagating over east-west paths 6800 km and 8400 km in length were received on antennas having different vertical-plane radiation angles indicate that very low radiation-angle antennas may be advantageous for use in long-distance communication systems. Over a period of several months, wide horizontal beam width antennas with vertical radiation angles of less than 2° provided, on the average, signals nearly 10 db stronger than those received on an antenna with a radiation angle of 15° and antennas with radiation angles in the range 2 to 5° provided signals about 5 db greater than the latter antenna. For a given system threshold a substantial increase in the amount of time a circuit may be operated is provided by the use of very low radiation-angle antennas. These results were obtained even though little power was radiated at low angles from the transmitting antenna and even for paths where ray theory indicates that higher angles are required for optimum propagation.

Data indicated that little difference in the fading rate of the signal received at various radiation angles was to be expected. Higher fading rates of the signal received over the longer path were recorded and it was concluded that this was most probably caused because the radio wave path traversed the auroral zone over the longer path whereas it did not on the shorter path.

A limited amount of data obtained during the occurrence of magnetic storms suggests that radio signals are degraded a shorter period of time when received on low radiation-angle antennas than if high radiation angles are used.

Without the close cooperation of Mr. George Jacobs of the United States Information Agency and the personnel of the Voice of America station at Munich, Germany, this experiment could not have been performed. Their able services are gratefully acknowledged. Considerable support for this program was also provided by the U.S. Army Signal Engineering Agency. The author is indebted also to A. R. Mitz, M. W. Woodward, R. C. Peck, and L. H. Tveten for their assistance in installing and maintaining the receiving equipment, to A. E. Smith and K. L. Phillips for aid in data scaling, and to R. Silberstein for his constructive discussions concerning the experiment and interpretation of the results.

7. References

[1] R. K. Potter and H. T. Friis, Some effects of topography and ground on short-wave reception, Proc. IRE **20,** 699 (1932).

[2] H. E. Hallborg and S. Goldman, Radiation angle variations from ionospheric measurements, RCA Review **8,** 342 (1947).

[3] A. F. Wilkins and F. Kift, Characteristics of HF signals, Electronic and Radio Engineer **34,** 335 (1957).

[4] Donald Foster, Radiation from rhombic antennas, Proc. IRE **25,** 1327 (1937).

[5] J. W. Koch, W. B. Harding, and R. J. Jansen, Fading rate recorder for propagation research, Electronics **32,** 78 (1959).

[6] Karl Rawer, The Ionosphere, p. 165 (Frederick Ungar Publishing Co., New York, N.Y., 1952).

[7] A. E. Harper, Rhombic antenna design, p. 49 (D. Van Nostrand Co., New York, N.Y., 1941).

[8] R. Silberstein, A long-distance, pulse-propagation experiment on 20.1 megacycles, J. Geophys. Research **63,** 445 (1958).

(Paper 65D2–115)

JOURNAL OF RESEARCH of the National Bureau of Standards—D. Radio Propagation
Vol. 65D, No. 2, March–April 1961

Graphical Determination of Radio Ray Bending in an Exponential Atmosphere*

C. F. Pappas, L. E. Vogler, and P. L. Rice

(August 11, 1960)

This paper presents a simple engineering method for calculating the amount of bending undergone by a radio ray passing through an exponential model atmosphere. For any initial takeoff angle and for values of the surface refractivity ranging from 200 to 450, the bending angle τ may be determined as a function of height above the earth's surface, using a few graphs and a few calculations. Indications of the accuracy of the method are given at the end of the paper.

1. Introduction

The course of a radiofrequency electromagnetic wave traveling through the atmosphere is altered by variations of the atmospheric index of refraction, n. These variations, due to changes in vapor pressure, air pressure and temperature, are extremely complex in detail; however, mathematical models of refraction can be constructed which represent an average picture of the variations. This paper considers an "exponential" model (the CRPL Exponential Reference Atmosphere [1][1]), in which the refractivity $(n-1)\times 10^6$ decreases exponentially with height, causing the radio wave to be bent away from its initial direction. The amount of bending is measured by the refraction angle, τ, and is important in such problems as the accurate determination by radar of the range and height of flying objects, the location of extra-terrestrial radio noise sources in radio astronomy, and the analysis of radio communication systems.

Mathematically, τ may be expressed in the following integral form [2,3]

$$\tau = -\cos\theta_0 \int_{n_0}^{n_1} (dn/n)[(nr/n_0 r_0)^2 - \cos^2\theta_0]^{-1/2} \quad (1)$$

where n is the atmospheric index of refraction, n_0 is the value of n at the surface of the earth and r, r_0, and θ_0 are defined in figure 1. The CRPL Exponential Reference Atmosphere is characterized by an index of refraction of the form

$$n = 1 + (n_0 - 1)e^{-c_e h}$$

where c_e is the decay constant and h is the altitude above the surface of the earth. For this model atmosphere eq (1) is not integrable in closed form; it can be expanded in series, but the resulting expression is quite complicated for hand calculations. A numerical integration method has been used to compute values of τ by Bean and Thayer; these are listed in reference 1. This method is only practical through the use of a large scale computer.

It might be noted that when θ_0 is large τ may be calculated by a formula which is quite simple and very accurate [4]:

$$\tau = \left(\frac{n_0 - 1}{n_0}\right) ctn\theta_0 (1 - e^{-c_e h}) \text{ (radians)}. \quad (2)$$

However, for small θ_0 no simple expression is available for calculations; thus, an engineering method was developed to provide a quick and practical means to obtain τ in this case. This method has the added advantage over the tables in ref [1] in that the N_s of τ is not limited to those listed.

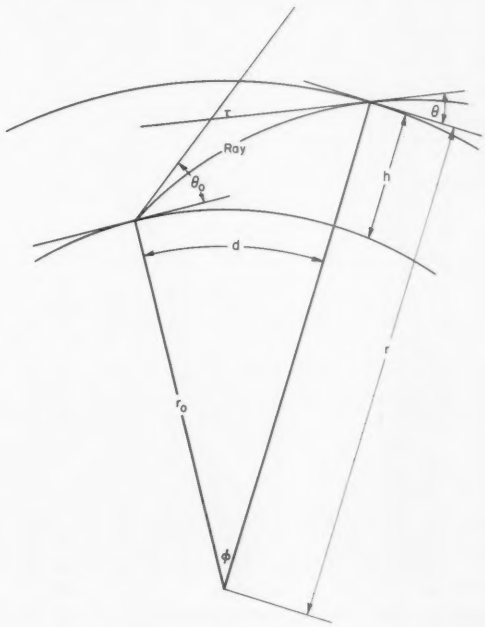

FIGURE 1. *Geometry of radio-ray refraction.*

*Contribution from Central Radio Propagation Laboratory, National Bureau of Standards, Boulder, Colorado.

[1] Figures in brackets indicate the literature references at the end of this paper.

2. Calculation of τ_a

The approximation of τ is denoted by τ_a; the formula is given by

$$\tau_a = f(n_0) \cos \theta_0 q e^{Bf(n_0)+pC} \quad (3)$$

where the terms are explained as follows:

τ_a = the bending approximation in milliradians.
$f(n_0)$ = read from figure 2 for a given N_s. If more accuracy is desired, this value can be computed by

$$f(n_0) = \left[\left(\frac{\pi}{2}\right)\left(\frac{n_0 - 1}{n_0}\right)(k-1)\right]^{1/2} \times 10^3.$$

n_0 = the index of refraction at the earth's surface.
k = the effective earth's radius factor.
N_s = the surface refractivity.
θ_0 = the initial elevation angle expressed in milliradians.
h_m = the height above the surface of the earth in meters.
q = read from figure 3 for a given h_m and θ_0.
B = read from figure 4 or 5 for a given h_m and θ_0.
p = a correction factor for N_s which is read from figure 6 for a given N_s.
C = a height correction factor which is obtained from figure 7 for a given h_m.

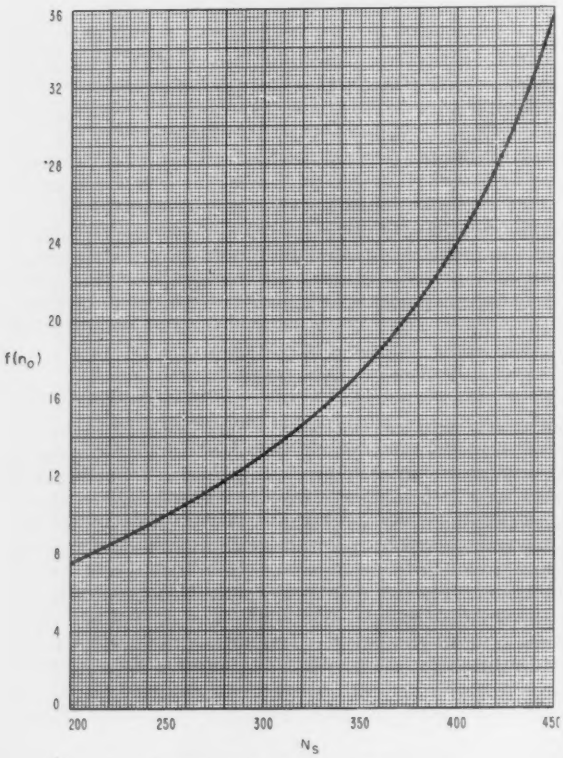

FIGURE 2. $f(n_0)$ *versus* N_s.

Two examples of the computation of τ_a are included to illustrate the use of the τ_a formula. One example is for an N_s of 252.9 and the second is an example using an N_s of 404.9 in which the pC correction factor has an effect.

Example 1. (Calculation of τ_a with $N_s \leq 344.5$)

Given: $N_s = 252.9$
$\theta_0 = 40$ milliradians
$h_m = 500$ meters

Find: $\tau_a = f(n_0) \cos \theta_0 q e^{Bf(n_0)+pC}$

$f(n_0) = 10.06$ (fig. 2)
$\cos \theta_0 = .99920$
$q = .0385$ (fig. 3)
$B = .00077$ (fig. 4)
$Bf(n_0) = .0077$
$p = 0$ (fig. 6)
$pC = 0$
$e^{Bf(n_0)+pC} = 1.0077$
$\tau_a = .39$ milliradians
$\tau = .38$ milliradians[2]

Example 2. (Calculation of τ_a with $N_s > 344.5$)

Given: $N_s = 404.9$
$\theta_0 = 200$ milliradians
$h_m = 30$ meters

Find: $\tau_a = f(n_0) \cos \theta_0 q e^{Bf(n_0)+pC}$
$f(n_0) = 24.70$ (fig. 2)
$\cos \theta_0 = .98007$
$q = .000472$ (fig. 3)
$B = .00117$ (fig. 4)

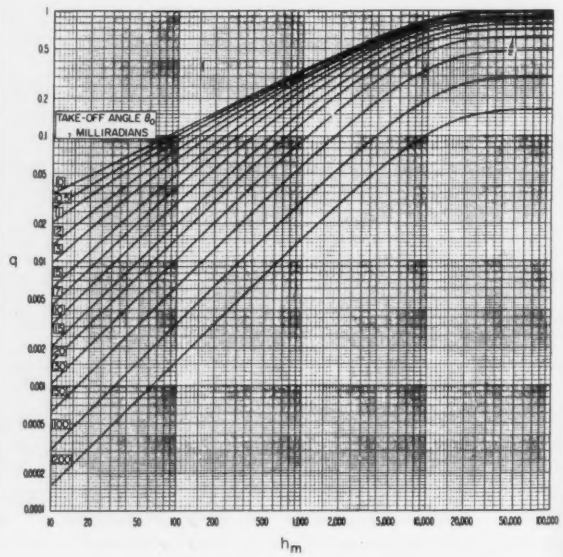

FIGURE 3. q *versus* h_m.

[2] Obtained by numerical integration.

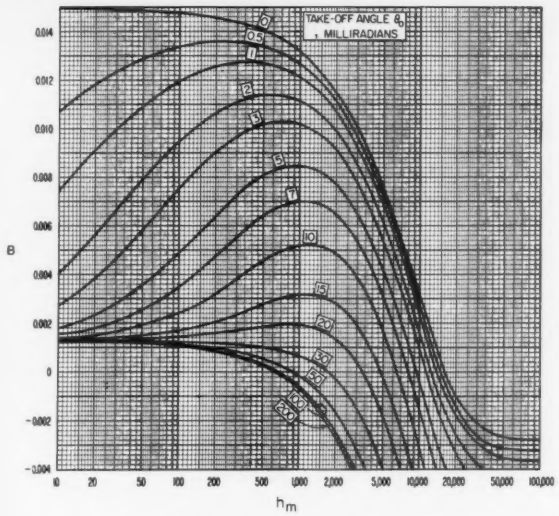

FIGURE 4. B *versus* h_m.

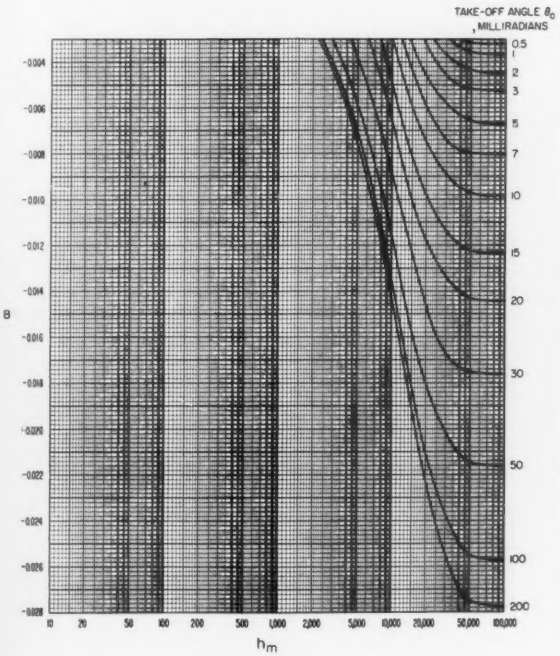

FIGURE 5. B *versus* h_m.

$$Bf(n_0) = .0289$$
$$p = .30 \quad \text{(fig. 6)}$$
$$C = -.125 \quad \text{(fig. 7)}$$
$$pC = -.0375$$
$$Bf(n_0) + pC = -.0086$$
$$e^{Bf(n_0)+pC} = .9914$$
$$\tau_a = .0113 \text{ milliradians}$$
$$\tau = .0113 \text{ milliradians}^2$$

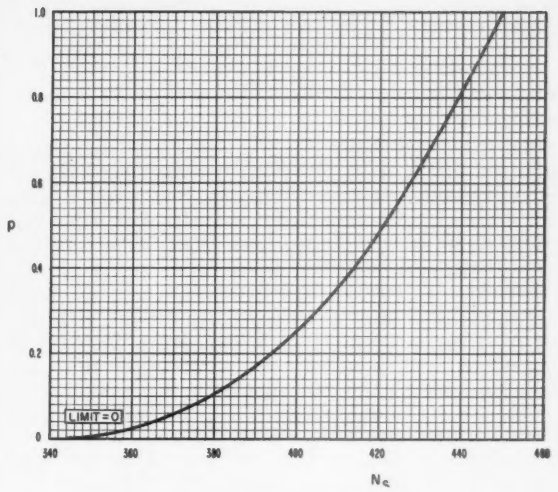

FIGURE 6. N_s *correction factor.*

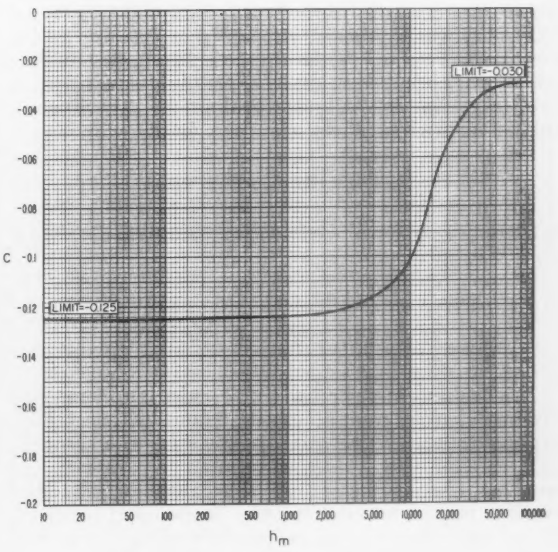

FIGURE 7. *Height correction factor.*

3. Derivation of τ_a formula

By plotting τ versus h for many different values of θ_0 and n_0, it was decided that the simplest form that could be assumed for τ to obtain the accuracy desired was

$$\tau = f(n_0) \cos \theta_0 e^{A+Bf(n_0)} \qquad (4)$$

The range of N_s considered lies between 200 and 450 since values outside this range rarely occur in actual practice.

Using two values of N_s, 200 and 344.5, and τ's obtained by the numerical integration procedure of ref [1], a least squares fit of

$$\ln\left(\frac{\tau}{f(n_0)\cos\theta_0}\right)$$

was made to obtain values of A and B for a given h_m and θ_0.

Values of e^A, denoted by q, were computed and graphed for h_m and given θ_0 (see fig. 3). The B values were also plotted versus h_m for given θ_0 (see figs. 4 and 5). It may be noted that q and B are not graphed for height values less than 10 m; at the upper range of height, a limit for q and B is approached and reached for a given θ_0.

Using the A and B values it was found that for an N_s greater than 344.5 a correction factor was needed to modify $qe^{Bf(n_0)}$ (or $e^{A+bf(n_0)}$) so that the ln $(\tau/f(n_0)\cos\theta_0)$ and, consequently, the τ error were within an acceptable range. The height correction C was obtained from the difference between ln $(\tau/f(n_0)\cos\theta_0)$ and $qe^{Bf(n_0)}$ for an N_s of 450 and plotted for graphical use (see fig. 7). Through further calculations and comparisons the relationship of N_s to the height correction C was determined for N_s greater than 344.5, and less than 450. This relationship was the basis for the N_s correction p which was plotted versus N_s (see fig. 6). Inclusion of this additional correction element results in an expression $qe^{Bf(n_0)+pC}$ for an N_s greater than 344.5. Since p equals zero when N_s is less than or equal to 344.5,

$$\tau_a = f(n_0)\cos\theta_0\, qe^{Bf(n_0)+pC}$$

becomes the general form for the simplified calculation of τ.

4. Accuracy of τ_a Method

In checking out the simplified calculation method various τ_a were compared with values of the CRPL exponential reference atmosphere τ for the same h_m and θ_0. Of the values computed τ_a showed the smallest absolute error at the lower heights and smaller N_s. The largest errors calculated were for N_s of 450, the maximum absolute error being 0.53 milliradians, with a maximum relative error of 6.8 percent.

Below is a table of computed values which gives indication of the range of absolute and percent error for several values of N_s. It will be noted that error values for an N_s of 200 and 344.5 were not included in this list since these values of N_s were used for the least squares fit and were considered to have less error than the N_s listed.

Only error values for τ_a greater than 1.0 milliradian were (arbitrarily) included in table 1. For τ_a less than 1.0 milliradian the absolute error is quite low, but the percent error can be high since τ_a is so small. This can give a somewhat distorted picture since a small τ_a may have an error of only 0.0001 milliradian and still be in error by greater than 3 percent.

TABLE 1.—*Range of error for $\tau_a > 1.0$ mr*

N_s	Range of absolute error	Range of percent error
252.9	0.0006 to 0.0739	0.01% to 2.11%
313.0	0 to .0918	0 to 1.91%
377.2	.0013 to .1507	.01% to 1.53%
404.9	0 to .2539	0 to 1.86%
450.0	.0024 to .5313	.22% to 6.79%

5. Explanation of Symbols

B=figures 4 and 5.

C=height correction factor; figure 7,

c_e=decay constant; see ref [1],

$f(n_0)$=figure 2,

$$=\left[\left(\frac{\pi}{2}\right)\left(\frac{n_0-1}{n_0}\right)(k-1)\right]^{1/2}\times 10^3,$$

h=altitude above the surface of the earth,

h_m=altitude above the surface of the earth in meters,

k=effective earth's radius factor

$$=\frac{n_0}{n_0-r_0c_e(n_0-1)},$$

n=atmospheric index of refraction

$=1+(n_0-1)e^{-c_eh}$ (CRPL Exponential Reference Atmosphere),

n_0=index of refraction at the earth's surface

$=n(h=0)$,

N_s=surface refractivity

$=(n_0-1)\times 10^6$,

p=N_s correction factor; figure 6,

ϕ=angle at center of the earth (see fig. 1)

$=\theta+\tau-\theta_0$.

q=figure 3,

r=radial distance from the center of the earth,

r_0=distance from the center to the surface of the earth,

τ=bending

$$=-\cos\theta_0\int_{n_0}^{n_1}(dn/n)\left[(nr/n_0r_0)^2-\cos^2\theta_0\right]^{-1/2}$$

τ_a=bending approximation in milliradians,

$=f(n_0)\cos\theta_0\, q\, e^{Bf(n_0)+pC}$

θ=local elevation angle

$$=\cos^{-1}\left(\frac{n_0r_0\cos\theta_0}{nr}\right),\ \text{(using Snell's law)}$$

θ_0=initial elevation or takeoff angle.

6. References

[1] B. R. Bean and G. D. Thayer, CRPL exponential reference atmosphere, NBS Monograph 4 (October 29, 1959).

[2] D. E. Kerr, Propagation of short radio waves, Radiation Laboratories Series, Vol 13, p. 49, (McGraw-Hill Book Co., New York, N.Y., 1951).

[3] B. R. Bean and G. D. Thayer, Models of the atmospheric radio refractive index, Proc. IRE **47**, No. 5, 740 (May 1959).

[4] W. M. Smart, Spherical astronomy, ch. III, Cambridge University Press, London (1931).

(Paper 65D2–116)

JOURNAL OF RESEARCH of the National Bureau of Standards—D. Radio Propagation
Vol. 65, No. 2, March-April 1961

A Formula For Radio Ray Refraction in An Exponential Atmosphere[1]

G. D. Thayer

(October 27, 1960)

A formula for the radio ray refraction angle, τ, is derived by integration of the approximate differential equation for the case where the refractivity, $(n-1)\times 10^6$, decreases exponentially with height above the surface of a smooth, spherical earth. The solution is in terms of the widely tabulated exponential and error functions, and is accurate to within 4 percent over the useful range of the variables employed.

1. Background

In problems where the direction of radio propagation is important, e.g., tracking radar, it is convenient to be able to compute the refraction of radio rays as they pass through the atmosphere. Assuming that the refractive index, n, is a function only of height above the surface of a smooth, spherical earth, the usual integral for the ray refraction angle, usually called the "bending", τ, is [1, 2] [2]

$$\tau=-\int_0^{h_\tau}\frac{\cos\theta_0[dN/dh]dh\times 10^{-6}}{\left\{\sin^2\theta_0+\frac{2h}{r_0}-2(N_s-N)\cos^2\theta_0\times 10^{-6}\right\}^{1/2}}, \tag{1}$$

where h_τ is the "target" height to which the bending is to be calculated, N is the radio refractivity, $(n-1)\times 10^6$, with N_s the surface value, and θ_0 is the initial elevation angle of the radio ray. The geometry involved in the problem is shown on figure 1.

The integral (1) is to be evaluated under the assumption that

$$N=N_s\exp\{-ch\}, \tag{2}$$

where c is a constant determining the gradient of N with respect to height; this is the exponential model atmosphere recently recommended for international use by the CCIR [3].

2. Development

The integral (1) with N given by eq (2) is put in readily integrable form by means of the approximation

$$N_s\times 10^{-6}[1-\exp\{-ch\}]\sim\gamma h \tag{3}$$

made where N_s-N appears in the denominator of (1). The parameter γ is defined by

$$\gamma=\frac{N_s\times 10^{-6}[1-\exp\{-cH\}]}{H},\ 0<H<h_\tau$$

where H is an effective integration height which was determined from published tabulations of refraction variables in model atmospheres of exponential form [4] for $\theta_0=0$, and is given by

$$H=4.75\,[\exp\{-0.01158cN_s\}][1-\exp\{-ch_\tau\}]. \tag{4}$$

With (3), the integral for τ in an exponential atmosphere is approximated by

$$\tau\cong cN_s\times 10^{-6}\cos\theta_0\int_0^{h_\tau}\frac{\exp\{-ch\}dh}{\left\{\sin^2\theta_0+2h\left[\frac{1}{r_0}-\gamma\cos^2\theta_0\right]\right\}^{1/2}} \tag{5}$$

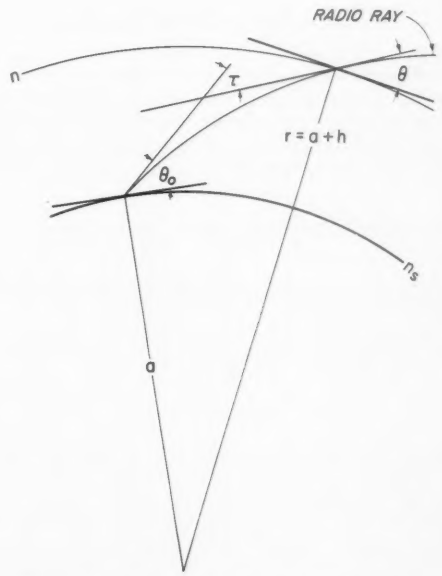

FIGURE 1. *Geometry of radio ray refraction.*

[1] Contribution from Central Radio Propagation Laboratory, National Bureau of Standards, Boulder, Colo.
[2] Figures in brackets indicate the literature references at the end of this paper.

The change of variable:

$$z(h)=\sqrt{z_0^2+ch},$$

$$z_0^2=\frac{ckr_0\sin^2\theta_0}{2},$$

where

$$k=\frac{1}{1-\gamma r_0\cos^2\theta_0},$$

results in:

$$\tau\cong N_s\times10^{-6}\cos\theta_0\sqrt{2ckr_0}\exp\{z_0^2\}\int_{z_0}^{z(h_\tau)}\exp\{-z^2\}\,dz.$$

This can be given in terms of the error function, [5]

$$\operatorname{erf}(x)=\frac{2}{\sqrt{\pi}}\int_0^x e^{-t^2}dt,$$

as:

$$\tau\cong N_s\times10^{-4}\cos\theta_0\sqrt{ck}\exp\{z_0^2\}\,[\operatorname{erf}\{z(h_\tau)\}-\operatorname{erf}\{z_0\}],\quad(6)$$

where $\sqrt{\pi r_0/2}$, r_0 in kilometers, has been absorbed as a factor of 100 in the constant 10^{-4}.

Equation (6) has the following form for the case of total bending, $h_\tau\geqq70$ km:

$$\tau(h_\tau\to\infty)\cong N_s\times10^{-4}\cos\theta_0\sqrt{ck}\exp\{z_0^2\}[1-\operatorname{erf}\{z_0\}],\quad(7)$$

which reduces to an interestingly short form for $\theta_0=0$,

$$\tau(h_\tau\to\infty,\theta_0=0)\cong N_s\times10^{-4}\sqrt{ck}.$$

3. Accuracy of the Solution

Equation (6) approximates the true value of τ with increasing accuracy as the initial elevation angle approaches $\pi/2$; this can be shown by substituting the asymptotic expansion of the error function [5] in eq (7), with the result that

$$\tau(h_\tau\to\infty)\cong N_s\times10^{-6}\cot\theta_0\left[1-\frac{1}{2z_0^2}+\frac{3}{4z_0^4}-\frac{15}{8z_0^6}+\cdots\right].$$

If z_0 is large enough so that $\frac{1}{2}z_0^2$ may be neglected (approximately for $\theta_0>0.3$ radians) then the familiar approximation to the total bending at large elevation angles results [1, 2],

$$\tau(h_\tau\to\infty)\cong N_s\times10^{-6}\cot\theta_0,\ \theta_0>0.3,$$

which is known to be convergent to the true value of τ as θ_0 approaches $\pi/2$. The extension to the case of $h_\tau<70$ km yields similar results.

The accuracy of eq (6), for $\theta_0<0.3$ radians, has been checked against published results obtained for the CRPL Exponential Reference Atmospheres [4]. The largest errors found, using (4) to obtain H, were about 4 percent, and these were for a profile with a very strong N-gradient; the largest errors for profiles of average N-gradient were about 1.5 percent.

For ease of calculation H may be set constant for all profiles and all h_τ; a value of $H\cong1$ km results in errors no larger than about 10 percent.

On the other hand if higher accuracy is desirable H may be made a function of initial elevation angle also; adding $f(\theta_0)$ to the value of H as given by (4), where

$$f(\theta_0)\sim\frac{185\,\theta_0}{1+24\,\theta_0},\ \theta_0\text{ in radians},$$

will limit the errors to about 1 percent for the CRPL exponential profiles.

In summary, eq (6) represents a relatively accurate and concise formulation for the ray bending in an exponential atmosphere. It has the advantage of being in terms of elementary, well-tabulated functions, and so can be easily programed for solution on digital or analogue computers, and in addition the solution is asymptotic to the correct values for large initial elevation angles.

4. References

[1] W. M. Smart, Spherical astronomy, Chapter III (Cambridge University Press, London, 1931).

[2] M. Schulkin, Average radio-ray refraction in the lower atmosphere, Proc. IRE **40**, 554 (1952).

[3] International Radio Consultative Committee, Documents of the IXth Plenary Assembly, Los Angeles, 1959, Vol. I: Recommendations, Sec. G: Propagation, Recommendation No. 309, Definition of a basic reference atmosphere.

[4] B. R. Bean and G. D. Thayer, CRPL exponential reference atmosphere, NBS Mono. 4, (1959).

[5] National Bureau of Standards, Appl. Math. Series 41, Tables of the error function and its derivative.

(Paper 65D2–117)

JOURNAL OF RESEARCH of the National Bureau of Standards—D. Radio Propagation
Vol. 65D, No. 2, March–April 1961

Impedance of a Monopole Antenna With a Circular Conducting-Disk Ground System on the Surface of a Lossy Half Space[1]

S. W. Maley and R. J. King

(September 27, 1960; revised December 1, 1960)

The base impedance of a $\lambda/4$ monopole antenna with a circular conducting disk ground system on the surface of a lossy half-space is calculated as a function of disk diameter using three different approximate methods. Verifying measurements were made on a model at X-band frequencies by simulating the lossy half-space with a water filled tank sufficiently large to approximate the results expected from an infinite lossy ground. The measured impedance values, Z, were broken up into the sum of two terms ΔZ and Z^∞ where Z^∞ is the impedance of the antenna with a perfectly conducting ground and ΔZ is a term which accounts for the finite size of the disk. The experimental measurements on a number of antennas indicate that the ratio $\Delta Z/Z^\infty$ as a function of disk diameter is nearly the same for all antennas measured. Comparison of the measured values of this ratio and the values calculated by the three different approximate methods indicate qualitative agreement.

1. Introduction

This paper presents a theoretical and experimental investigation of the impedance of a vertical monopole with a thin, circular, conducting disk ground system on the surface of a lossy half space as represented in figure 1. The monopole impedance was calculated using three different methods and was experimentally measured for antenna heights near one-quarter wavelength and for a range of values of disk diameter. The investigation was made at X-band frequencies to permit the experimental work to be done in the laboratory under carefully controlled conditions. The lossy half space was simulated by use of a water-filled tank about 120 wavelengths square. The calculated and measured values of impedance have been plotted on the same chart to permit comparison.

2. Impedance Calculations

2.1. Formulation of Impedance

The base impedance of the monopole antenna system represented in figure 1 is calculated using three different approximate methods. Due to the symmetry of the configuration a cylindrical coordinate system is used making the field expressions independent of the azimuthal coordinate ϕ.

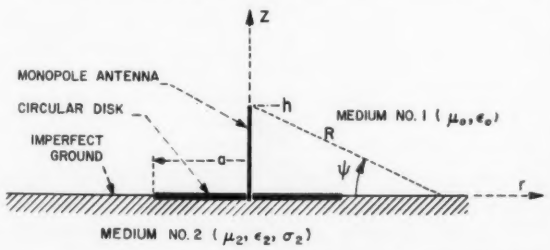

FIGURE 1. *Monopole antenna with a circular conducting disk ground system on the surface of a lossy half-space.*

It is convenient to express the magnetic field, $H_\phi(r,z)$ in the form

$$H_\phi(r,z)=H_\phi^\infty(r,z)+H_\phi^s(r,z). \tag{1}$$

The superscript "∞" denotes the field that would exist if the ground were perfectly conducting, while superscript "s" denotes the difference between the actual field and the field that would exist for a perfectly conducting ground. We also express the antenna impedance Z in a similar manner:

$$Z=Z^\infty+\Delta Z. \tag{2}$$

Here again the superscript "∞" denotes the impedance for a perfectly conducting ground, and ΔZ is the difference between the actual impedance and the impedance for a perfectly conducting ground.

As is shown by Wait and Pope, [5] [2] the change in impedance, ΔZ, may be expressed as

$$\Delta Z=-\frac{1}{I_0^2}\int_0^\infty H_\phi^\infty(r,0)E_r(r,0)2\pi r dr. \tag{3}$$

$H_\phi^\infty(r,0)$ is given by the expression

$$H_\phi^\infty(r,0)=-\frac{1}{2\pi}\frac{\partial}{\partial r}\int_0^h \frac{e^{-jk(z^2+r^2)^{1/2}}}{(z^2+r^2)^{1/2}}I(z)dz, \tag{4}$$

where

$$k^2=\omega^2\mu_0\epsilon_0.$$

In this expression, $I(z)$ is the current in the antenna as a function of z, and I_0 is the magnitude of the base current. The antenna is assumed to be thin and therefore the antenna current may be assumed real and sinusoidally distributed. Thus we have

[1] Contribution from Engineering Experiment Station, University of Colorado, Boulder, Colo. The work reported here was supported by the Electronics Research Directorate of the U. S. Air Force Cambridge Research Center.

[2] Figures in brackets indicate the literature references at the end of this paper.

$$I(z)=\frac{I_0}{\sin\alpha}\sin(\alpha-kz). \tag{5}$$

α is given by

$$\alpha=k(h+h'), \tag{6}$$

where h is the antenna height, and h' is a parameter which characterizes the top loading. Using (5) eq (4) may be written as follows:

$$H_\phi^\infty(r,0)=-\frac{I_0}{2\pi\sin\alpha}\frac{\partial}{\partial r}\int_0^h\frac{e^{-kj(z^2+r^2)^{1/2}}}{(z^2+r^2)^{1/2}}\sin(\alpha-kz)dz. \tag{7}$$

The integration in eq (7) is straightforward but somewhat involved: the result is

$$H_\phi^\infty(r,0)=\frac{jI_0}{2\pi\sin\alpha}\left[\frac{e^{-jk(r^2+h^2)^{1/2}}}{r}\cos(\alpha-kh)-\frac{e^{-jkr}}{r}\cos\alpha-\frac{jhe^{-jk(r^2+h^2)^{1/2}}}{(r^2+h^2)^{1/2}r}\sin(\alpha-kh)\right]. \tag{8}$$

In order to evaluate eq (3), it is necessary to have an expression for E_r $(r, 0)$, but an exact solution for E_r $(r, 0)$ is not available in a useable form. Therefore, to obtain an answer, an approximation to E_r $(r, 0)$ may be used to obtain an approximate value for ΔZ. For low frequencies, Wait and Surtees [6] have used the approximate boundary condition given by

$$\left.\begin{aligned}E_r(r,0)&\cong-\eta H_\phi(r,0) && r>a\\ &=0 && r<a\end{aligned}\right\}, \tag{9}$$

where

$$\eta=\left(\frac{\mu_2}{\epsilon_c}\right)^{1/2}$$

and

$$\epsilon_c=\epsilon_2-j\frac{\sigma_2}{\omega}.$$

"a" is the radius of the thin, circular conducting disk. Then they have used the additional approximation,

$$H_\phi(r,0)\cong H_\phi^\infty(r,0). \tag{10}$$

Approximation (10) is valid for low frequencies but only for small values of r. However, at low frequencies, the significant contribution to the integral in (3) is for low values of r; therefore, the approximations (9) and (10) may both be used to give the approximation

$$\left.\begin{aligned}E_r(r,0)&\cong-\eta H_\phi^\infty(r,0) && r>a\\ &=0 && r<a\end{aligned}\right\}. \tag{11}$$

Another approximation suggested by Wait and Surtees is that given by

$$\left.\begin{aligned}E_r(r,0)&\cong-\eta F(w)H_\phi^\infty(r,0) && r>a\\ &=0 && r<a\end{aligned}\right\}, \tag{12}$$

where $F(w)$ is the ground-wave attenuation factor as given by Norton [2]. For low frequencies and low values of r, (12) reduces to (11) because the factor $F(w)$ is very nearly unity with a zero phase angle. Approximation (12) is probably a better approximation than (11) for high frequencies.

For frequencies as high as that used in the accompanying experimental investigation (10 kMc/s), it was felt that a good approximation for $E_r(r, 0)$ would be that given by

$$\left.\begin{aligned}E_r(r,0)&\cong E_r'(r,0) && r>a\\ &=0 && r<a\end{aligned}\right\}, \tag{13}$$

where $E_r'(r, 0)$ is the radial component of the electric field at the surface of the ground for the case in which no disk is present. $E_r'(r, 0)$ is given by Norton's formula (14).

2.2. Calculation of Impedance

Norton's formula [2] gives the tangential electric field at the surface of the ground for a current element of differential length dl, carrying a current I, and located a distance b, above the ground. Since this field is a function of b, the expression for the field will be written E_r' $(r, 0, b)$ to indicate this dependence. Norton's formula may be written:

$$E_r'(r,0,b)=-j\,30\,kIdl\left[\cos\psi(1-R_v)\frac{e^{-jkR}}{R}\right]\left\{\sin\psi+u(1-u^2\cos^2\psi)^{1/2}F(w)\left[1-\frac{u^2(1-u^2\cos^2\psi)}{2}+\frac{\sin^2\psi}{2}+\frac{1}{j2kR}\right]+\sin\psi\frac{1}{jkR}+u(1-u^2\cos^2\psi)^{1/2}\frac{1}{jkR}\right\}, \tag{14}$$

where

$$R=(r^2+b^2)^{1/2},$$

$$u=\frac{k}{k_2},$$

and

$$k_2^2=\omega^2\mu_2\epsilon_c.$$

R_v is the vertical reflection coefficient and $F(w)$ is the ground wave attenuation factor as given by Norton in the form of tables and charts [2]. ϵ_c is the complex permittivity of medium No. 2.

The field, $E_r(r, 0)$, is now given by

$$E_r(r,0)\cong E_r'(r,0)=\int_0^h E_r'(r,0,b)I(b)db. \tag{15}$$

The complexity of the expressions for E_r' $(r, 0, b)$ makes it necessary to evaluate the integral in (15) numerically. This integral must be evaluated for each value of r that is required. Since E_r $(r, 0)$ must be obtained by a numerical integration, eq (3) for ΔZ must also be evaluated by a numerical integration. The integral in (3) was approximated by a sum over a finite range of values of r; then a constant was added to correct for the use of the finite range for r rather than an infinite range. It was found that this constant could be evaluated to a high degree of accuracy. Using this method it was found that the integrations in eqs (3) and (15) can be carried out numerically to an adequate degree of accuracy without a prohibitive amount of work. These calculations have been made for a quarter-wave monopole at 10 kMc/s for the case in which medium No. 2 is water. The complex dielectric constant used for water was $\epsilon_c = 49 - j34$. The impedance ΔZ was also calculated for the same antenna and the same frequency, using the approximations (11) and (12).

The results of the calculations for all three approximations are shown along with the measured values, in figure 4. The resistive and reactive components of ΔZ are plotted as functions of disk radius in wavelengths.

3. Construction of the Experimental Equipment

A large 12 ft x 12 ft x 4 in. plywood water tank (117 wavelengths square at 9.60 kMc/s) was held aloft so that the impedance measuring equipment could be placed directly beneath the monopole positioned at the tank center. It is anticipated that the finite size of the tank causes insignificant error because identical measurements were made with a tank roughly half the size of the one used here.

The monopole was fed by a 50Ω rigid air-coaxial line 0.620 in. in length which made a transition into 8 in. of 48Ω rigid air-coaxial line. The latter was in turn connected into a coaxial slotted section with a standard type "N" connector. A micrometer equipped probe carriage then provided a means of measuring the standing wave pattern position with a tolerance of ±0.001 cm.

The short section of 50Ω air-coaxial line used a replaceable center conductor which plugged into the 48Ω line center conductor. Various lengths of the monopole (an extension of the center conductor) could then be interchanged without disturbing the coaxial feed system. A single supporting teflon bead 0.020 in. long was fastened approximately midway in the 50Ω air-coaxial line. The inside diameter (⅛ in.) of the monopole feed line was made as small as machining considerations would allow, thereby better approximating a "thin" antenna and a "point" feed, and providing a very high attenuation (75.3 db/cm) for the TE_{11} mode of propagation.

Stability considerations required that the 48Ω line be as rigid as possible, thus allowing the monopole to be raised and lowered without disturbing the system calibration. For these same reasons, the number of mechanical joints was kept to a minimum.

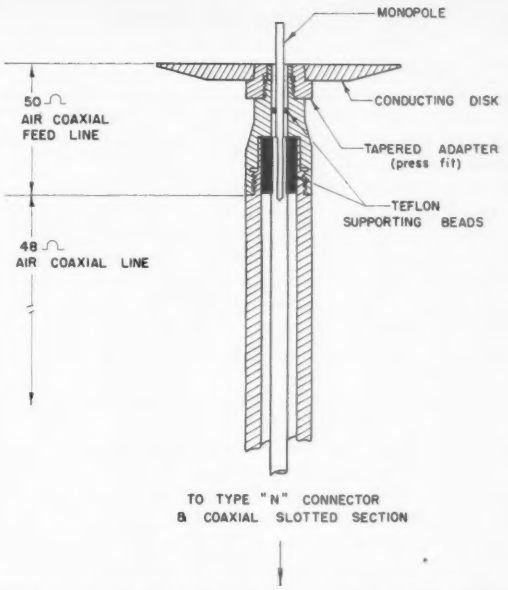

FIGURE 2. *Assembled view of 0.750 λ radius disk with 0.250 λ monopole and the associated coaxial feed line.*

Although it was desirable to have a low residual standing wave ratio, the mechanical stability was far more important in achieving accurate calibration.

Measurements were taken for disks whose radii ranged from ⅛ to ⅜ wavelength and for monopoles with lengths from 0.230 to 0.270 wavelength and with a diameter of 0.045 wavelength. Data for the larger disks were taken using a single disk which was machined down about 0.050 in. in diameter after each successive measurement. This procedure provided accurate reseating of the disk after each radius change and presented a noticeable improvement over results obtained when a set of several disks of different radii was used. This machining procedure was continued to a disk radius of ¼ wavelength; then three special disks were used to complete the range. The three smaller disks screw directly onto the 50Ω air-coax while the larger disk was set in place with the aid of an adapter. The adapter-disk connection utilized a press fit onto a slight taper. Figure 2 shows the cross section of the assembled feed line with the conducting disk mounted in position.

Ordinary tap water at 20° C was used as the surrounding imperfectly conducting ground region. The water meniscus at the edge of the conducting disk was eliminated by securing a 0.001 in. thickness of mylar sheet to the top surface with vacuum-system grease. This established an abrupt transition between the disk and water. This grease is extremely viscous and has a high dielectric constant. The position of the disk could be accurately determined from the observer's position below the water tank with the aid of a special mirror-telescope arrangement.

4. Experimental Results

The input reflection coefficient to the rigid coaxial line was measured as a function of the disk radius, and the results were plotted on a Smith Chart. The plot for a given monopole, as a function of disk radius, takes the shape of a spiral as shown in figure 3. Using an impedance transformation technique, which is described elsewhere, [4] the monopole base impedance was found; the resistive and reactive components were plotted as functions of disk radius. From these plots the impedance, Z_c^∞, for an infinitely large disk could be estimated by extrapolation. This impedance then was subtracted from the monopole base impedance to give ΔZ as a function of disk radius.

Impedance measurements were made for a number of antennas. It was found that Z_c^∞ varied appreciably with antenna length and further that it was somewhat higher in magnitude than would be expected on the basis of published analyses of a monopole over a perfectly conducting ground [1, 3]. This discrepancy was thought to be due to the effects of the annular gap between the monopole and the circular conducting disk and of the high-frequency resistance of the monopole. It was found, however, that the ratio, $\Delta Z/Z_c^\infty$, plotted as a function of disk diameter was nearly the same for all antennas measured.

The experimentally established dependence of ΔZ upon Z_c^∞ suggested that the function $\Delta Z/Z_c^\infty$ involving measured quantities ΔZ and Z_c^∞ should be compared with the function $\Delta Z/Z_c^\infty$ involving the calculated function ΔZ and the calculated impedance, Z_c^∞, of a monopole over a perfectly conducting ground. The value for Z_c^∞ was taken to be [1, 3]

$$Z_c^\infty = 34 + j16.$$

The function $\Delta Z/Z_c^\infty$, was measured and plotted for a number of antennas with lengths varying from 0.23 to 0.27 wavelengths. These plots were all nearly the same. Three representative plots for antenna lengths of 0.230, 0.250, and 0.270 wavelength were selected and are shown in figure 4. In order to present the results in terms of ohms rather than as dimensionless quantities, both the experimental functions $\Delta Z/Z_c^\infty$ and the calculated functions $\Delta Z/Z_c^\infty$ were multiplied by Z_c^∞. The real parts of the resulting functions are labeled ΔR and the imaginary parts ΔX.

The values of Z_c^∞ for the three antennas for which measured data is presented are shown in table 1.

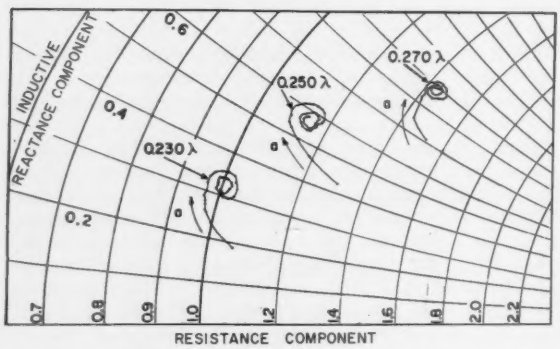

FIGURE 3. *Measured monopole input reflection coefficient spirals for 3 monopole heights.*
(Taken from a small section of a Smith chart).

TABLE 1.

Monopole height in wavelengths	Z_c^∞ in ohms
0.230	45+j6.3
.250	55.1+j15.3
.270	77.7+j24

The calculations were made at 10 kMc/s, but the experimental measurements were taken at 9.60 kMc/s. Since the radius of the disk is in wavelengths the curves may be compared directly.

5. Conclusions

Examination of the curves of figure 4 indicates that all three of the approximate methods of impedance calculation yield results which agree in a qualitative sense with the measured data in both amplitude and phase.

The theoretically calculated data was for a 0.25 λ monopole; the measured data was for three different monopole heights, 0.23 λ, 0.25 λ, and 0.27 λ. The curves show that the measured data for the 0.23 λ monopole agree with the calculated data better than that for the 0.25 λ or 0.27 λ monopoles.

Comparing the individual calculated curves with measured curves shows that the approximation given by (11) is good for the resistive component of the impedance but is substantially too great in magnitude for the reactive component. The approximation given by (12) gives results which are too low in magnitude for both the resistive and reactive components; however, the phase in this case agrees well with the measured data. Of the three approximations considered, the one given by (14) seems to give results in closest agreement with the measured data in both amplitude and phase. These results show two things; first, that the approximation (14) is reasonably good; and second, that Norton's formula for the electric field tangential to the ground is reasonably accurate even for distance of the order of one wavelength from the antenna.

6. References

[1] R. W. P. King, The theory of linear antennas, p. 165 (Harvard University Press, Harvard, Conn., 1956).

[2] K. A. Norton, The propagation of radio waves over the surface of the earth and in the upper atmosphere, Proc. IRE **24,** p. 1367 (Oct. 1936).

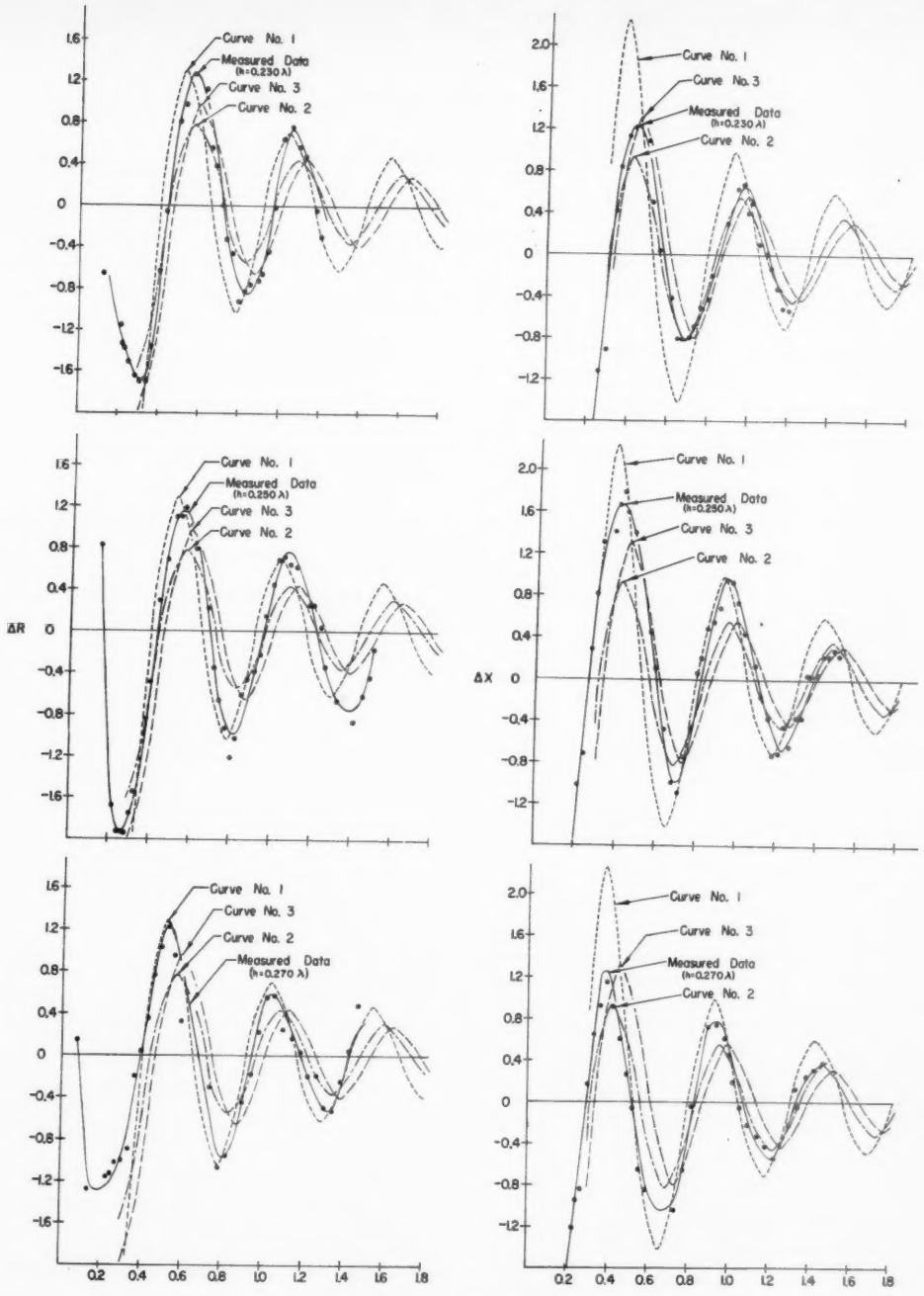

FIGURE 4. *Calculated and measured values of incremental resistance and reactance of monopoles on a disk ground system as a function of disk radius.*

The calculated curves are for a quarter-wave monopole at 10 kMc and are based on the following approximations:

No. 3. $E_r(r,0)$ as given by Norton's formula.
No. 2. $E_r(r,0) = -\eta F(\omega) H_\phi^\infty(r,0)$
No. 1. $E_r(r,0) = -\eta H_\phi^\infty(r,0)$

The measured data is for a frequency of 9.60 kMc/s and a monopole height h.

[3] S. Ramo and J. R. Whinnery, Fields and waves in modern radio, p. 546 (John Wiley & Sons, Inc., New York, N.Y., 1953).
[4] Scientific Report ERD–TN–60–763, Impedance and pattern studies of disk-based monopoles over lossy ground surfaces, Electronics Research Directorate, Air Force Research Division, Air Research and Development Command, July 1960, Contract No. AF 19 (604)–4556.
[5] J. R. Wait and W. A. Pope, The characteristics of a vertical antenna with a radial conductor ground system, Applied Scientific Research, B **4,** 177 (1954).
[6] J. R. Wait and W. J. Surtees, Impedance of a top loaded antenna of arbitrary length over a circular grounded screen, J. Appl. Phys. **25,** 553 (1954).

(Paper 65D2–118)

JOURNAL OF RESEARCH of the National Bureau of Standards—D. Radio Propagation
Vol. 65D. No. 2, March–April 1961

Radio-Wave Propagation in the Earth's Crust[1, 2]

Harold A. Wheeler

(February 26, 1960)

There is a reasonable basis for postulating the existence of a useful waveguide deep in the earth's crust, of the order of 2 to 20 km below the surface. Its dielectric is basement rock of very low conductivity. Its upper boundary is formed by the conductive layers near the surface. Its lower boundary is formed by a high-temperature conductive layer far below the surface, termed the "thermal ionosphere" by analogy to the well-known "radiation ionosphere" far above the surface.

The electrical conductivity of the basement rock has not been explored. An example based on reasonable estimates indicates that transmission at 1.5 kc/s might be possible for a distance of the order of 1500 km.

This waveguide is located under land and sea over the entire surface of the earth. It may be useful for radio transmission from the shore to a submarine on the floor of the ocean. The sending antenna might be a long conductor in a drill hole deep in the basement rock; the receiving antenna might be a vertical loop in the water.

In the earth's crust, there appears to be a deep waveguide that has not yet been explored. This waveguide extends under all the surface area, so it suggests the possibility of wave propagation under the ocean floor. This might enable communication from land to a submarine located on or near the ocean floor. If below a certain depth, it happens that the excess radio noise from electric storms would become weaker than thermal noise, and no other source of appreciable radio noise is recognized.

This waveguide comprises basement rock as a dielectric between upper and lower conductive boundaries. The upper boundary is formed of the well-known geological strata located between the surface and the basement rock, with conductivity provided by electrolytic solutions and semiconductive minerals. The lower boundary is provided by high-temperature conductivity in the basement rock.

In concept, the lower boundary is similar to the usual ionosphere, being formed by gradually increasing conductivity. In the usual ionosphere [Wait, 1957], caused by extraterrestrial radiation, the conductivity increases with height. In the present case, however, the conductivity increases with depth and is caused by the increasing temperature in the dielectric material. Therefore it may be designated as the "inverted ionosphere" or "thermal ionosphere."

Figure 1 shows how this waveguide may be used for communication from a shore sending station (S) to an underwater receiving station (R). The latter may be a submarine on the bottom of the ocean. The sender launches a vertically polarized transverse-electro-magnetic (TEM) wave by means of a vertical wire projecting into the basement rock. The wave is propagated in the deep waveguide between the surface conductor and the thermal ionosphere. Some power from the wave leaks out of the waveguide into the ocean just above, and is sampled by an antenna at the receiver.

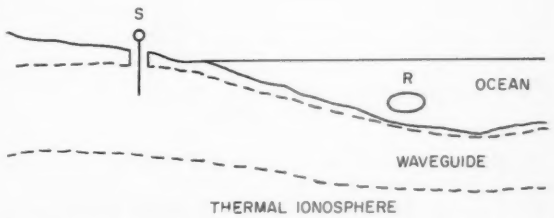

FIGURE 1. *Communication through the deep waveguide under the ocean.*

Figure 2 shows an arrangement for the sender antenna. It is a long conductor (pipe) sunk into a drill hole filled with oil insulation. The example shown has conducting material down to a depth of about 1 km. Through this layer of earth, there is an outer pipe which forms the outer conductor of a coaxial transmission line. This pipe is in contact with a conducting surface such as water or radial wires in the ground. Below this layer of earth, the inner conductor extends further about 2 km into the basement-rock dielectric. This extension radiates into the waveguide in the usual manner.

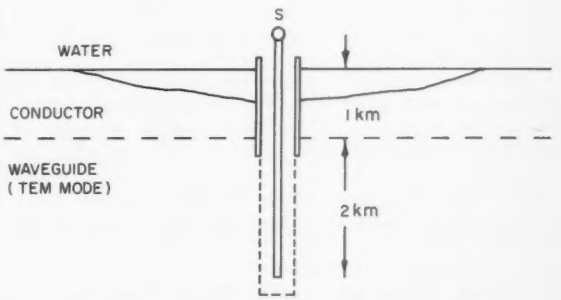

FIGURE 2. *Sender antenna in the deep waveguide.*

[1] Contribution from Wheeler Laboratories, Great Neck, N.Y., and Developmental Engineering Corp., Leesburg, Va.
[2] Paper presented at Conference on the Propagation of ELF Radio Waves, Boulder, Colo., January 27, 1960.

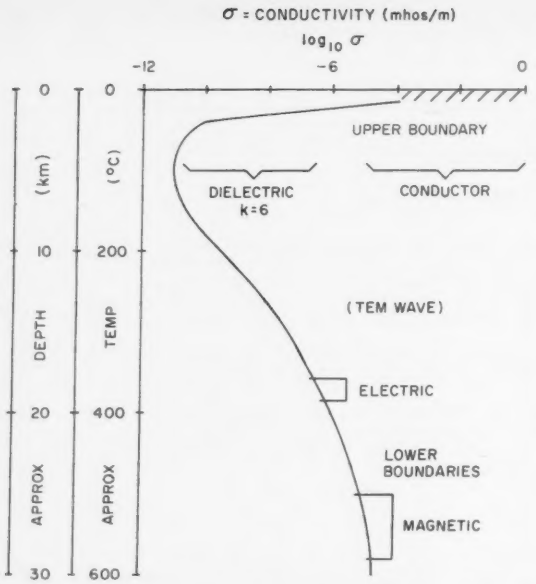

FIGURE 3. *Variation of conductivity with depth to form the deep waveguide.*

Figure 3 shows how the temperature and the resulting conductivity may vary with depth, especially in the basement rock at depths exceeding a few kilometers. This diagram will be used to explain the expected behavior of the deep waveguide. At depths of about 2 to 20 km, the basement rock is indicated to have such low conductivity that it is a dielectric suitable for wave propagation. Above and below this dielectric, the conductivity is high enough to serve the function of boundaries for the waveguide.

The upper boundary is fairly well defined, in a depth of the order of 1 km (perhaps down to several kilometers). Its conductivity, in the most common materials, ranges from a maximum of 4 mhos/m in sea water down to about 10^{-4} in rather dry nonconductive minerals.

The dielectric layer, shown between depths of about 2 and 20 km, may have very low conductivity, of the order of 10^{-6} to 10^{-11} mho/m. The lowest conductivity is observed in fused quartz, but probably is not found in nature. The present plan is useful if the conductivity is around 10^{-8} or lower. The dielectric constant is about 6.

The lower boundary has some unusual properties. (These are also characteristic of the ionosphere at frequencies below VLF.) The gradual increase of conductivity [Van Hippel, 1954] provides an effective boundary for each kind of field, that for the electric field being closer than that for the magnetic field. In each case, there is a sort of skin depth in the boundary [Wheeler, 1952]. Both of these boundaries make comparable contributions to the total dissipation factor of the waveguide, which determines the exponential attenuation rate.

The location of each boundary depends on the frequency, the conductivity, and the rate of change of conductivity with depth. In the example to be outlined, these boundaries occur at temperatures in the range of 300 to 600 °C.

As an example of the behavior that might be expected in this waveguide, the following numerical values are suggested.

Frequency	1.5 kc/s
Dielectric constant	6
Wavelength (in dielectric)	80 km
Effective boundaries of E field (depths)	1–18 km
Effective boundaries of M field (depths)	1–27 km
Skin depth for E field (lower boundary)	1.5 km
Skin depth for M field (lower boundary)	4 km
Length of radiator (in waveguide)	2 km
Reactance of radiator	1600 ohms
Effective length of radiator	1 km
Radiation resistance (in waveguide)	0.4 ohms
Other resistance	20 ohms
Radiation efficiency	0.02
Average power factor of E and M fields, about	0.1
Napier distance (for wave attenuation)	130 km
Decibel distance (for wave attenuation)	15 km
100–db distance	1500 km

If these values are to be experienced, communication ranges of the order of 1500 km will be possible under the surface of the earth.

The assumptions for this example are based on preliminary estimates of the best conditions that are at all likely to be realized. The high-temperature conductivity needed for the lower boundary is typical of quartz and other similar minerals. The extremely low conductivity at lower temperatures is unlikely, but need not be quite so low to provide a dielectric that could give the indicated performance.

As for the properties of the basement rock, it is very doubtful how low its conductivity may be. Its seismic properties are explored but not its electrical conductivity. Its principal chemical components are known, but apparently not its small content of "impurities" that may determine the conductivity. It seems that core samples have been made to only a small depth (less than 1 km) in the basement rock, presumably because there has been little prospect of valuable mineral products at a reasonable cost. It is notable that some tests show a trend toward lower conductivity (below 10^{-6}) in the transition from the surface layers into the basement rock. A continuation of this trend may enable such performance as is indicated in the example.

Returning to the waveguide properties, the TEM mode (with vertical polarization) is the one that has the greatest probability of enabling long-range communication. It is the only propagating mode at frequencies below about 2 kc/s (including the above example).

This preliminary study has indicated that the deep waveguide is probably a definite physical phenomenon. The properties of its dielectric and boundaries are not known quantitatively, so it is uncertain to what distances this waveguide may be useful for communication or related purposes. Some rather optimistic assumptions as to these properties

lead one to speculate on distances of the order of 1500 km. While the deep waveguide extends under the entire surface of land and sea, it is most needed for radio transmission to a submarine on the ocean floor, because this location is shielded from the usual radio waves above the surface.

This concept occurred to the writer recently during discussions with Lester H. Carr and his associates in Developmental Engineering Corporation, notably L. E. Rawls, G. F. Leidorf, and their geological consultant, P. Parker. The opportunity of working with this group is acknowledged with appreciation.

References

Von Hippel, A. R., Dielectric materials and applications. Fused quartz at high temperatures, p. 403 (John Wiley & Sons, New York, N.Y., 1954).

Wait, J. R., The mode theory of VLF ionosphere propagation for finite ground conductivity, Proc. IRE 45, 760–767 (June 1957).

Wheeler, H. A., Universal skin-effect chart for conducting materials, Electronics 25, No. 11, 152–4 (Nov. 1952). (Including land and sea.)

(Paper 65D2–119)

JOURNAL OF RESEARCH of the National Bureau of Standards—D. Radio Propagation
Vol. 65D, No. 2, March–April 1961

Publications of the National Bureau of Standards*

Selected Abstracts

Use of the incoherent scatter technique to obtain ionospheric temperatures, T. E. VanZandt and K. L. Bowles, *J. Geophys. Research* **65,** *No. 9, 2627–2628 (Sept. 1960).*
If the ion-electron gas is in diffusive equilibrium on the topside of the F layer, then the electron density decreases exponentially with height, and its logarithmic decrement is proportional to the neutral gas temperature. From an electron density profile obtained by the scatter radar technique, it is shown that this interpretation is consistent. Moreover, the deduction of ionospheric temperatures in this way from scatter radar electron density profiles has several advantages over other methods.

Correlation of an auroral arc and a subvisible monochromatic 6300 A Arc with outer-zone radiation on November 28, 1959, B. J. O'Brien, J. A. VanAllen, F. E. Roach, and C. W. Gartlein, *J. Geophys. Research* **65,** *No. 9, 2759–2766 (Sept. 1960).*
During a severe geomagnetic storm on November 28, 1959, two Geiger tubes on satellite Explorer VII (1959 iota) found anomalies in the outer radiation zone at an altitude of about 1000 km which appear to be correlated in space and time with optical emissions from the atmosphere beneath. Very intense narrow zones of radiation were detected over a visible aurora during one pass. The radiation in three such zones was harder toward low latitudes. On three subsequent passes the radiation zone was deduced to be over a subvisible 6300 A arc, whose brightness diminished as the radiation zones became less intense. The correlation is discussed.

Seasonal variations in the twilight enhancement of [OI] 5577, L. R. Megill, P. M. Jamnick, and J. E. Cruz, *J. Atmospheric and Terrest. Phys.* **18,** *No. 4, 309–314 (Aug. 1960).*
Measurements of the twilight enhancement of [OI] 5577 were obtained during the period September 1957 to December 1958 at Rapid City, S.D. All these measurements were normalized to the intensity at sunset or sunrise at a height of 100 km. The results obtained indicate that there was a seasonal dependence of the twilight enhancement of [OI] 5577 emission. The enhancement occurred most frequently in the autumn and winter months, the maximum occurring about 1 November. The enhancement almost never occurred during the spring and summer months.

Some magnetoionic phenomena of the Arctic *E*-region, J. W. Wright, *J. Atmospheric and Terrest. Phys.* **18,** *No. 4, 276–289 (Aug. 1960).*
Several unusual phenomena of E-region ionogram echoes obtained at Thule, Greenland (mag. dip 85.5°) are described. They are explained as the effects of electron collisions on the propagation of radio waves at high-magnetic latitudes. The third magnetoionic component (Z-echo) is explained in this way and several of its distinguishing features are explained and illustrated. New phenomena demonstrate the existence of an E-pause (valley above h_{max} E), and permit the measurement of electron densities and collision frequencies therein.

Widely separated clocks with microsecond synchronization and independent distribution systems, T. L. Davis and R. H. Doherty, *IRE Wescon Conv. Record* **4,** *pt. 5, 3–17 (1960).*
In a majority of timing applications, a problem exists in setting two or more clocks to agree with one another. Present techniques using WWV or other high frequency broadcasts allow clocks to be synchronized within one millisecond. This paper offers an improvement in synchronization of three orders of magnitude.
Microsecond synchronization is obtained by use of the Loran-C navigation system as the link between a master clock at Boulder, Colorado, and any slaved clock anywhere in the Loran-C service area.
The timing system also includes a unique method for distribution of several time code formats on a single UHF channel.

Comment on models of the ionosphere above h_{max} F_2, J. W. Wright, *J. Geophys. Research* **65,** *No. 9, 2595–2596 (Sept. 1960).*
Evidence for a gradient of scale height in the F region is shown, and discussed in relation to a simple Chapman model of the F region above $h_{max}F_2$. It is suggested that a similar model, but allowing for a scale-height gradient, may give somewhat better agreement with recent observations.

Improvements in radio propagation prediction service, W. B. Chadwick, *Elec. Eng.* **79,** *721–724 (Sept. 1960).*
Data from world-wide ionospheric and solar stations permit close observation of the changing state of the ionosphere so that the maximum usable frequency for radio communications between any two points in the world can be accurately predicted 3 months in advance.

Other NBS Publications

Journal of Research, Vol 65A, No. 1, January–February 1961. 70 cents.

Faint lines in the arc spectrum of iron (Fe I). C. C. Kiess, V. C. Rubin, and C. E. Moore.
Infrared absorption of spectra of some 1-acetamido pyranoid derivatives and reducing, acetylated pyranoses. R. Stuart Tipson and H. S. Isbell.
Monolayers of linear saturated succinate polyesters and air-liquid interfaces. W. M. Lee, J. Leon Shereshefsky, and R. R. Stromberg.
Heat of formation of beryllium chloride. W. H. Johnson and A. A. Gilliland.
Heat of decomposition of potassium perchlorate. W. H. Johnson and A. A. Gilliland.
Heats of formation of lithium perchlorate, ammonium perchlorate, and sodium perchlorate. A. A. Gilliland and W. H. Johnson.
Heat of formation of N-dimethylaminodiborane. W. H. Johnson, I. Jaffe, and E. J. Prosen.
Separation of hafnium from zirconium by anion exchange. J. L. Hague and L. A. Machlan.
Reaction of sulfur, hydrogen sulfide, and accelerators with propylene and butadiene. F. J. Linnig, E. J. Parks, and L. A. Wall.

Journal of Research, Vol. 65C, No. 1, January–March 1961. 75 cents.

Electronic scanning microscope for a spectrographic plate comparator. M. L. Kuder.
Viscoelastometer for measurement of flow and elastic recovery. R. J. Overberg and H. Leaderman.
An ultra low frequency bridge for dielectric measurements. D. J. Scheiber.
The ephi system for VLF direction-finding. G. Hefley, R. F. Linfield, and T. L. Davis.
Fast counting of alpha particles in air ionization chambers. Z. Bay, F. D. McLernon, and P. A. Newman.

X-ray diffraction measurement of intragranular misorientation in alpha brass subjected to reverse plastic strain. C. J. Newton and H. C. Vacher.

Enthalpy and specific heat of nine corrosion-resistant alloys at high temperatures. T. B. Douglas and A. C. Victor.

Determination of minor constituents in low-alloy steels by X-ray fluorescence. R. E. Michaelis, R. Alvarez, and B. A. Kilday.

Standard X-ray diffraction powder patterns, H. E. Swanson, M. I. Cook, E. H. Evans, and J. H. deGroot. NBS Circ. 539, Vol. 10 (1960) 40 cents.

Heat treatment and properties of iron and steel, T. G. Digges and S. J. Rosenberg. NBS Mono. 18 (1960) 35 cents. (Supersedes C495).

Specific heat and enthalpies of technical solids at low temperatures. A compilation from the literature, R. J. Corruccini and J. J. Gniewek. NBS Mono. 21 (1960) 20 cents.

The metric system of measurement, NBS Misc. Publ. 232 (1960) 50 cents.

Household weights and measures. NBS Misc. Publ. 234 (1960) (Supersedes M39) 5 cents.

Screw-thread standards for federal services, 1957. Amends in part H28 (1944) (and in parts its 1959 Supplement). NBS Handb. H28 (1957) Part III (1960) 60 cents.

Quarterly radio noise data—June, July, August 1959, W. Q. Crichlow, R. D. Disney, and M. A. Jenkins. NBS TN18–3 (PB151377–3) (1960) $1.00.

Quarterly radio noise data—September, October, November 1959, W. Q. Crichlow, R. D. Disney, and M. A. Jenkins. NBS TN18–4 (PB151377–4) (1960) $1.50.

Investigation of bearing creep of two forged aluminum alloys, L. Mordfin, N. Halsey, P. J. Granum. NBS TN55 (PB161556) (1960) $1.00.

Rapid determination of the order of chemical reactions from time-radio tables, J. H. Flynn. NBS TN62 (PB161563) (1960) 75 cents.

Radio refractometry, J. W. Herbstreit. NBS TN66 (PB-161567) (1960) 50 cents.

Transistorized building blocks for data instrumentation, J. A. Cunningham and R. L. Hill. NBS TN68 (PB161569) (1960) $2.00.

Low- and very low-radiofrequency model ionosphere reflection coefficients, J. R. Johler, L. C. Walters, J. D. Harpen, Jr. NBS TN69 (PB161570) (1960) $2.00.

Calibration of five gamma-emitting nuclides for emission rate, J. M. R. Hutchinson. NBS TN71 (PB161572) (1960) 75 cents.

Table of magnitude of reflection coefficient versus return loss $\left(L_R = 20 \log_{10} \frac{1}{151}\right)$, R. W. Beatty and W. J. Anson. NBS TN72 (PB161573) (1960) $1.25.

VHF and UHF power generators for RF instrumentation, A. H. Morgan and P. A. Hudson. NBS TN77 (PB161578) (1960) 75 cents.

Halobenzenes as sensitizers for the radiation-induced polymerization of styrene, D. W. Brown and L. A. Wall, J. Polymer Sci, 44, 325 (June 1960).

Some aspects of fluorine flame spectroscopy, D. E. Mann. Proc. Propellant Thermodynamics and Handling Conf. Special Rept. **12** (Ohio State University, Columbus, Ohio, June 1960).

Optical constants of aluminum, H. Mendlowitz. Proc. Phys. Soc. (London, England) **LXXV,** 664 (1960).

Current thermodynamic research on light- element compounds at the national bureau of standards, T. B. Douglas. Proc. Propellant Thermodynamics and Handling Conf. Special Rept. **12** (Ohio State University, Columbus, Ohio, June 1960).

Free radicals in gamma, irradiated polystyrenes, R. E. Florin, L. A. Wall, and D. W. Brown, Trans, Faraday Soc. **56,** No. 453, 1304–1310 (Sept. 1960).

Sealed-off Hg^{198} atomic-beam light source, R. L. Barger and K. G. Kessler. J. Opt. Soc. Am. **50,** No. 7, 651 (July 1960).

Temperature dependence of Young's modulus of vitreous germania and silica, S. Spinner and G. W. Cleek. J. Appl. Phys. **31,** No. 8, 1407 (1960).

Atomic clocks for space experiments, P. L. Bender, Astronautics p. 69 (July 1960).

Photolysis of ammonia in a solid matrix at low temperatures, O. Schnepp and K. Dressler. J. Chem. Phys. **32,** No. 6, 1682 (June 1960).

Photochemical rates in the equatorial F_2 region from the 1958 eclipse, T. E. Van Zandt, R. B. Norton, and G. H. Stonehocker, J. Geophys. Research **65,** No. 7, 2003 (July 1960).

Influence of source distances on the impedance characteristics of ELF radio waves, J. R. Wait, Proc. IRE **48,** No. 7, 1338 (July 1960).

Electroless plated contacts to silicon carbide, R. L. Raybold. Rev. Sci. Instr. **31,** No. 7, 781 (July 1960).

Statistical models for component aging experiments, J. R. Rosenblatt. Intern. Conv. Record. Inst. Radio Engrs. **8,** Pt. 6, 115 (1960).

Isotope effect in the hydrogen atom-formaldehyde reaction, J. R. McNesby, M. D. Scheer, and R. Klein, J. Chem. Phys. **32,** No. 6, 1814 (June 1960).

Electric current and fluid spin created by the passage of a magnetosonic wave, R. P. Kanawal and C. Truesdell, Arch. Rational Mach. and Analysis, 5, No. 5, **432,** (1960).

The nature of the inorganic phase in calcified tissues, A. S. Posner. Calcification in Biological Systems, p. 373 (American Assoc. Advancement of Sci., Washington, D.C., 1960).

Effect of water-reducing admixtures and set-retarding admixtures on properties of concrete, Introduction and Summary, B. E. Foster. Am. Soc. Testing Materials Spec. Tech. Publ. **266,** Introduction 1 & 2 and Summary 240 (June 1960).

Absorption spectra of solid methane, ammonia, and ice in the vacuum ultraviolet, K. Dressler and O. Schnepp, J. Chem. Phys. **33,** No. 1, 270 (July 1960).

The extent of H II regions, S. R. Pottasch, Astrophys. J. **132,** No. 1, 269 (July 1960).

Nickel oxide thin film resistors for low pressure shock wave detection, K. E. McCullon. Rev. Sci. Instr. **31,** No. 7, 780 (July 1960).

Casimir coefficients and minimum entropy production, R. E. Nettleton, J. Chem. Phys. **33,** No. 1, 237 (July 1960).

Variations of surface tension calculated with improved approximation for activity coefficient, L. C. Shepley and A. B. Bestul. J. Am. Ceram. Soc. **43,** No. 7, 386 (July 1960).

Council adopts F. D. I. specification for alloy for dental amalgam, Council on Dental Research, J. Am. Dental Assoc. **60,** No. 6, 773 (June 1960).

The foundations of mechanics and thermodynamics, E. A. Kearsley and M. S. Green, Phys. Today **13,** No. 7, 22 (July 1960).

Optical methods for negative ion studies, S. J. Smith and L. M. Branscomb, Rev. Sci. Instr. **31,** No. 7, 733 (July 1960).

On the theory of the slow-tail portion of atmospheric waveforms, J. R. Wait, J. Geophys. Research **65,** No. 7, 1939 (July 1960).

Statistical aspects of the cement testing program, W. J. Youden. Am. Soc. Testing Materials Proc **59,** 1120 (1959).

Optical transmissivity and characteristic energy losses, H. Mendlowitz, J. Opt. Soc. Am. **50,** No. 7, 739 (July 1960).

Pyrolysis of polyolefins, L. A. Wall and S. Straus, J. Polymer Sci. **44,** 313 (June 1960).

A barium fluoride film hygrometer element, F. E. Jones, and A. Wexler, J. Geophys. Research **65,** No. 7, 2087 (July 1960).

Low-energy photoproduction of neutral mesons from complex nuclei, R. A. Schrack, S. Penner, and J. E. Leiss, II Nuovo Cimento **16,** Serie X, 759 (March 1960).

Adsorption spectra of solid xenon, krypton, and argon in the vacuum ultraviolet, O. Schnepp and K. Dressler, J. Chem. Phys. **33,** No. 1, 49 (July 1960).

Radiation patterns of finite-size corner-reflector antennas, A. C. Wilson, H. V. Cottony, IRE Trans, Ant. Prop. **AP–8,** No. 2, 144 (Mar. 1960).

Structure of sulfurous esters, H. Finegold, Proc. Chem. Soc. (London) **283** (Aug. 1960).

VLF attenuation for east-west and west-east daytime propagation using atmospherics, W. L. Taylor, J. Geophys. Research **65,** No. 7, 1933 (July 1960).

Mechanized conversion of colorimetric data to munsell renotations, W. Rheinboldt and J. P. Menard. J. Opt. Soc. Am. **50,** No. 8, 802 (Aug. 1960).

The use of geostationary satellites for the study of ionospheric electron content and ionospheric radio-wave propagation, O. K. Garriott and C. G. Little, J. Geophys. Research **65,** No. 7, 2025 (July 1960).

Our measurement system and national needs, A. V. Astin, Sperryscope **15,** No. 6, 16 (1960).

Standards of heat capacity and thermal conductivity, D. C. Ginnings, Book, Thermoelectricity, p. 320 (Including Proc. Conf. Thermoelectricity, Sponsored by the Naval Research Lab., Sept. 1958) (1960).

Neutron-insensitive proportional counter for gamma-ray dosimetry, R. S. Caswell, Rev. Sci. Instr. **31,** No. 8, 869 (Aug. 1960).

A study of 2-Mc/s ionospheric absorption measurements at high altitudes, K. Davies, J. Geophys. Research **65,** 2285 (Aug. 1960).

Carrier-frequency dependence of the basic transmission loss in tropospheric forward scatter propagation, K. A. Norton, J. Geophys. Research **65,** 2029 (July 1960).

The ionization constants of 2-chloro-4-nitrophenol and 2-nitro-4-chlorophenol, V. E. Bower and R. A. Robinson, J. Phys. Chem. **64,** 1078 (1960).

Closed circuit liquid hydrogen refrigeration system, D. B. Chelton, J. W. Dean, and B. W. Birmingham, Rev. Sci. Instr. **31,** 712 (July 1960).

A quantitative formulation of Sylvester's law of inertia, A. M. Ostrowski, Natl. Acad. Sci. Proc. **45,** No. 5, 740 (May 1959).

Infrared transmission of clouds, D. M. Gates and C. C. Shaw, J. Opt. Soc. Am. **50,** 876 (Sept. 1960).

Comparative fixation of calcium and strontium by synthetic hydroxyapatite, R. C. Likins, H. G. McCann, A. S. Posner, and D. B. Scott, J. Biolog. Chem. **235,** No. 7, 2152 (July 1960).

A comparison of atomic beam frequency standards, R. E. Beehler, R. C. Mockler, and C. S. Snider, Nature Letter **187** 681, (Aug. 20, 1960).

VI. Microscopic and macroscopic energy loss distributions. 1. Theoretical reviews: A summary, U. Fano, Natl. Acad. Sci., Natl. Research Council Publ. **752,** Report 29, p. 24 (Aug. 1960).

The mechanical properties of ceramics and their measurement at elevated temperatures, S. J. Schneider, Book, Thermoelectricity, Chapter **21,** 342 (1960).

A rating method for refrigerated trailer bodies hauling perishable foods, C. W. Phillips, W. F. Goddard, Jr., and P. R. Achenbach, ASHRAE J. **2,** No. 5, 45 (May 1960).

Reply to, On the structure of trimethylamine-trimethylboron, D. R. Lide, Jr., J. Chem. Phys. **32,** No. 5, 1570 (May 1960).

Dimensional changes occurring in dentures during processing, J. B. Woelfel, G. C. Paffenbarger, and W. T. Sweeney, J. Am. Dental Assoc. **61,** No. 4, 413 (Oct. 1960).

Teeth, artificial, G. C. Paffenbarger and G. B. Denton, Encyclopedia Britannica **21,** 878 (Jan. 1960).

A method of improving isolation in multi-channel waveguide systems, G. F. Engen, IRE Trans. Microwave Theory and Tech. Letter **MTT-8,** 460 (July 1960).

Influence of earth curvature and the terrestrial magnetic field on VLF propagation, J. R. Wait and K. Spies, J. Geophys. Research **65,** 2325 (Aug. 1960).

Charge transfer and electron production in $H^- + H$ collisions, D. G. Hummer, R. F. Stebbings, W. L. Fite, and L. M. Branscomb, Phys. Rev. **2,** 668 (July 1960).

The characteristic energy losses of electrons in carbon, L. B. Leder and J. A. Suddeth, J. Appl. Phys. **8,** 1422 (Aug. 1960).

Note historique sur les premieres annees de la microscopie electronique, L. Marton, Extrait Bull. Acad. Roy. Belg. (Classe des Sciences) **5,** 119 (Mar. 1959).

An optical study of the boundary layer transition processes in a supersonic air system, W. Spangenberg and W. R. Rowland, Phys. of Fluids **3,** No. 5, 667 (Sept.–Oct. 1960).

Thermodynamic structure of the outer solar atmosphere. VI. Effect of departures from the Saha equation on inferred properties of low chromosphere, S. R. Pottasch and R. N. Thomas, Astrophys. J. **132,** 195 (July 1960).

Polymer decomposition: Thermodynamics, mechanisms, and energetics, L. A. Wall, Soc. Plastic Engrs. **Pt. I,** 810 (Aug. 1960); Pt. II, 1031 (Sept. 1960).

The role of surface tension in determining certain clay-water properties, W. C. Ormsby, Bull. Am. Ceramic Soc. **39,** No. 8, 408 (Aug. 1960).

**Publications for which a price is indicated (except for Technical Notes) are available only from the Superintendent of Documents, U.S. Government Printing Office, Washington 25, D.C. (foreign postage, one-fourth additional). The Technical News Bulletin and Basic Radio Propagation Predictions are available on a 1-, 2-, or 3-year subscription basis, although no reduction in rates can be made. Reprints from outside journals and the NBS Journal of Research may often be obtained directly from the authors.*

The National Bureau of Standards

announces a three-week course in

Radio Propagation

July 31 to August 18, 1961

Central Radio Propagation Laboratory
Boulder, Colorado

This course is designed to provide a discussion of the fundamentals of radio propagation, the latest advances in the state of the art, and the application of this knowledge to the design and development of communication systems. Tropospheric Propagation and Ionspheric Propagation will be considered in two separate sections which may be taken individually or in succession. Details of this course may be obtained from the Educational Director at the address given below.

The course will consider communication via the entire range of useable radio frequencies and will extend into the modes of propagation which are being explored for the future. In both sections the continuing emphasis will be on those elements of propagation which affect system design and frequency allocation.

In addition to the subject matter mentioned above the two sections will include discussion of the following:

Tropospheric Propagation (July 31-August 4, 1961)

The effect of atmospheric turbulence, and of both normal and unusual atmospheric stratification, upon the refraction and attenuation of radio waves . . . Climatology of the atmospheric radio refractive index and its measurement by refractometers or weather data . . . Diffraction and reflection from irregular terrain and absorption by trees and buildings . . . The phase stability of microwave signals and its effect upon systems of tracking, guidance, and geodetic measurement . . . Mechanisms of tropospheric propagation . . . Variability of transmission loss and the theoretical basis for transmission loss prediction . . . Modulation studies and techniques . . . Methods for predicting the probability of satisfactory point-to-point communication, broadcast coverage, and communication via satellites.

Ionospheric Propagation (August 7-18, 1961)

Theory of radio wave propagation via the ionosphere, from the very lowest frequencies to microwaves . . . The distorting effects of ionospheric irregularities and dispersion on broad-band radio signals . . . A description of the ionosphere—its spatial and temporal variations and their predictability . . . Transmission loss and its variability as a function of frequency and other system parameters . . . Special problems of earth-space communication . . . Statistical character and average power of atmospheric, cosmic, and artificial radio noise . . . Characterization of the propagation medium as a time-variant communication channel . . . Consideration of perturbations of amplitude and phase, multipath propagation, and noise as factors affecting modulation techniques, and the capacity and reliability of systems . . . Prediction of performance of ionospheric radio systems for communication, detection and positioning, navigation and timing.

Prerequisites:

A bachelor's degree in Electrical Engineering, Physics, or other suitable academic or practical experience.

Tuition:

Tropospheric Propagation—$100
Ionospheric Propagation—$200
Entire course—$300

Registrations will be limited and early application should be made to ensure consideration. Further details of the course and registration forms will be available March 1, 1961, from: Edmund H. Brown, Educational Director, Boulder Laboratories, National Bureau of Standards, Boulder, Colorado.

Notice

The papers listed below will appear in early issues of *Radio Propagation:*

Propagation studies using direction finding techniques. Edgar C. Hayden.

Pulse diversity effects in long distance high frequency radio propagation. S. A. Bowhill.

The influence of ionospheric conditions on the accuracy of high frequency direction finding. P. J. D. Gething.

Phase difference observations at spaced aerials and their application to direction finding. W. C. Bain.

Research at the National Bureau of Standards applicable to long-distance communication and direction-finding problems. R. Silberstein.

Design for spinning goniometer automatic direction finding. W. J. Lindsay and D. S. Heim.

Resolution characteristics of correlation arrays. Isham W. Linder.

Instrumentation for propagation and direction finding measurements. Edgar C. Hayden.

The Brooke variance classification system. E. M. L. Beale.

The estimation of variances of position lines from fixes with unknown target positions. E. M. L. Beale.

The statistics of a radio wave diffracted by a random ionosphere. S. A. Bowhill.

Space analysis of radio signals. John B. Smyth.

The effect of receiver bandwidth on amplitude distribution of VLF atmospheric noise. Forrest F. Fulton, Jr.

Propagation of VLF and ELF radio waves excited by a horizontal magnetic dipole. Janis Galejs.

Smooth earth diffraction calculated for horizontal polarization. L. E. Vogler.

Comparison between mode theory and ray theory of VLF propagation. H. Volland.

Power density requirements for airglow excitation by gyro-waves. V. A. Bailey.

On the validity of some approximations to the Appleton-Hartree formula. Kenneth Davies and G. A. M. King.

UNITED STATES
GOVERNMENT PRINTING OFFICE
DIVISION OF PUBLIC DOCUMENTS
WASHINGTON 25, D.C.

OFFICIAL BUSINESS

PENALTY FOR PRIVATE USE TO AVOID
PAYMENT OF POSTAGE, $300
(GPO)

JOURNAL OF RESEARCH of the National Bureau of Standards Vol. 65D, No. 2 March–April 1961
D. Radio Propagation

Contents

	Page
Ionospheric motions observed with high-frequency back-scatter sounders. Lowell H. Tveten.	115
Relationship between red auroral arcs and ionospheric recombination. G. A. M. King and F. E. Roach.	129
Fresnel region fields of circular aperture antennas. Ming-Kuei Hu.	137
Free-balloon borne meteorological refractometer. John F. Theisen and Earl E. Gossard.	149
Weather and reception level on a troposphere link—annual and short-term correlations. L. G. Abraham, Jr., and J. A. Bradshaw.	155
Initial results of a new technique for investigating sferic activity. Gifford Hefley, Robert H. Doherty, and Robert F. Linfield.	157
Effect of antenna radiation angles upon HF radio signals propagated over long distances. W. F. Utlaut.	167
Graphical determination of radio ray bending in an exponential atmosphere. C. F. Pappas, L. E. Vogler, and P. L. Rice.	175
A formula for radio ray refraction in an exponential atmosphere. G. D. Thayer.	181
The impedance of a monopole antenna with a circular conducting-disk ground system on the surface of a lossy half space. S. W. Maley and R. J. King.	183
Radio-wave propagation in the earth's crust. Harold L. Wheeler.	189
Publications of the National Bureau of Standards.	193

For sale by the Superintendent of Documents, U.S. Government Printing Office, Washington 25, D.C. Price 70 cents (single copy)
Subscription price: $4.00 a year; 75 cents additional for foreign mailing

UNITED STATES GOVERNMENT PRINTING OFFICE, WASHINGTON : 1961

DID

copy)